

AD-A110 918

STANFORD UNIV CA STANFORD ELECTRONICS LABS

F/G 4/1

A STUDY OF ARTIFICIAL MODIFICATION OF THE VLF PROPAGATION CHARA--ETC(U)

JUL 80 P A BERNHARDT

N00014-77-C-0586

UNCLASSIFIED

SU-SEL-E324-1

NL

1 04 1  
000  
110910

END  
DATE  
FILMED  
03-82  
DTIC

LEVEL *11*

*Q*

*NR 523-047*  
*10/2/81*

# RADIOSCIENCE LABORATORY

STANFORD ELECTRONICS LABORATORIES  
DEPARTMENT OF ELECTRICAL ENGINEERING  
STANFORD UNIVERSITY · STANFORD, CA 94305



AD A110918

A STUDY OF ARTIFICIAL MODIFICATION OF THE VLF PROPAGATION  
CHARACTERISTICS OF THE PLASMASPHERE  
FINAL REPORT

by

Paul A. Bernhardt

Technical Report E324-1

July 1980

Sponsored by

The Office of Naval Research  
through Contract No. N00014-77-C-0586

DTIC  
FEB 12 1982  
H

DISTRIBUTION STATEMENT A  
Approved for public release,  
Distribution Unlimited

DTIC FILE COPY

82 02 01 (33

A STUDY OF ARTIFICIAL MODIFICATION OF THE VLF PROPAGATION  
CHARACTERISTICS OF THE PLASMASPHERE

FINAL REPORT

by

Paul A. Bernhardt

July 1, 1980

TECHNICAL REPORT E324-1

Prepared under  
The Office of Naval Research  
Contract N00014-77-C-0586

Radioscience Laboratory  
Stanford Electronics Laboratories  
Stanford University  
Stanford, California 94305

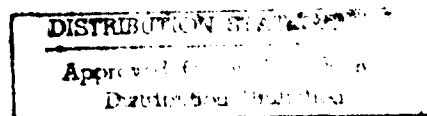


## TABLE OF CONTENTS

	<u>Page</u>
A. INTRODUCTION. . . . .	1
B. NEUTRAL GAS DIFFUSION MODEL . . . . .	2
C. GAS DYNAMICS OF VAPOR RELEASES. . . . .	3
D. RADIOWAVE PROPAGATION . . . . .	4
E. ANALYSIS OF VLF PHASE AND AMPLITUDE DATA. . . . .	5
PUBLICATION LIST. . . . .	6

Form For	
THIS GROUP	<input checked="" type="checkbox"/>
DEIC TAB	<input type="checkbox"/>
Unannounced	<input type="checkbox"/>
In Connection	
<i>Attch in file</i>	
By	
Distribution/	
Availability Codes	
Avail and/or	
Special	
<i>A</i>	

## A. INTRODUCTION

This is the Final Report for Office of Naval Research Contract Number N00014-77-C-0586. This report describes theoretical studies related to man-made disturbances of the upper atmosphere which can affect VLF wave propagation. The purpose of our research was to estimate the effect that artificially created plasma holes could have on whistler mode signals propagating through the ionosphere. In the course of our research, we have developed models which describe the flow of reactive vapor which can be injected into the plasma layers. Our research has considered the influence of the modified ionosphere on propagation of HF and VHF as well as VLF radiowaves. During the final period of research, we have found evidence of man-made perturbation of the earth-ionosphere waveguide.

## B. NEUTRAL GAS DIFFUSION MODEL

An overview at the status of our ionospheric depletion modeling indicated that our simulations of neutral gas expansion needed the most improvement. Consequently, we have developed a model of three-dimensional expansion of neutral gases in a nonuniform, chemically reactive medium. This model is described in the following paper which was published in the Journal of Geophysical Research and which was presented at the 1978 Summer Computer Simulation Conference.

# Three-Dimensional, Time-Dependent Modeling of Neutral Gas Diffusion in a Nonuniform, Chemically Reactive Atmosphere

PAUL A. BERNHARDT

*Radioscience Laboratory, Stanford University, Stanford, California 94305*

A time-varying model of neutral gas expansion in a nonuniform environment is developed. The model includes diffusion in a multicomponent atmosphere, chemical reactions between the diffusing gases and the atmosphere, thermal diffusion effects, and transport due to altitude-dependent winds. The three-dimensional diffusion equation governing the neutral gas flow is solved numerically using Fourier transform and finite difference techniques. Examples of  $H_2$ , OH, and  $CO_2$  diffusion illustrate the effects of chemical reactions and wind shears on the neutral expansion. The model may be applied to chemical releases which produce ionospheric depletions or luminescent trails.

## 1. INTRODUCTION

Passive experiments, such as tracing neutral wind patterns, or active experiments, such as chemical depletion of the  $F$  layer, involve the release of neutral gases into the upper atmosphere. Diffusive expansion governs the flow of these gases.

Previous theoretical treatments have considered various approximations to diffusive gas expansions. An analytic solution for diffusion of a point release in a lossless, exponential atmosphere was presented by Yu and Klein [1964]. This solution was generalized to continuous releases and extended for height-independent chemical losses by Bernhardt *et al.* [1975] and Bernhardt [1976]. Forbes and Mendillo [1976] and Mendillo and Forbes [1978] have produced an analytic solution for diffusion in an atmosphere with a chemical loss that varies exponentially with altitude.

A numerical model, as opposed to an analytic model, of neutral gas expansion in a cylindrical geometry has been described by Potier and Carr [1971]. This model described the solution to the diffusion equation in a two-dimensional (radial and axial) coordinate system using a finite difference technique. This model gives more realistic results than the analytic models because it does not require a simple analytic description of the atmospheric constituents. However, the two dimensionality of the model limits the range of its applicability.

None of the models mentioned thus far have included (1) the effects of an altitude-dependent neutral wind, (2) the diffusion of neutral species produced by chemical reactions between the released gas and the background atmosphere, (3) the expansion of several gases (which may react with each other as well as with the atmosphere), (4) the effects of thermal diffusion, and (5) the effects of a multispecies background atmosphere. This paper describes a numerical model of diffusion which contains all of the features mentioned above.

The numerical model, however, has its limitations. Latitudinal and longitudinal variations in the background atmosphere and neutral wind velocity are not included. Also, any departures from pure diffusion are neglected. For example, Schunk [1978] has shown that nonlinear acceleration and viscous stress may become significant for releases above 300-km altitude. A numerical model including these effects is currently being developed.

## 2. THREE-DIMENSIONAL DIFFUSION EQUATIONS

The equations describing the diffusion of several gases in a multicomponent atmosphere are developed. Fourier transform

is used to remove the spatial derivatives in the horizontal plane. An exponential transformation is used along the vertical axis. In the formulation the subscripts  $i$  and  $k$  refer to the  $i$ th injected gas species and the  $k$ th atmospheric species, respectively. The coordinates  $x$ ,  $y$ , and  $z$  represent the east, north, and vertical directions, respectively.

Consider  $M$  neutral species diffusing through a background atmosphere composed of  $K$  gas species. The diffusion velocity for neutral species  $i$  is written as

$$\mathbf{w}_i = \mathbf{w} - D_i \left[ \frac{1}{n_i} \nabla n_i + \frac{\hat{a}_z}{H_i} + \frac{(1 + \alpha_i)}{T} \nabla T \right] \quad (1)$$

$i = 1, 2, \dots, M$

[Vincenti and Kruger, 1965; Banks and Kockarts, 1973], where the  $i$ th neutral gas has velocity  $\mathbf{w}_i$ , scale height  $H_i = (kT)/(m_i g)$  ( $k$  is Boltzmann's constant), mass  $m_i$ , diffusion coefficient  $D_i$ , concentration  $n_i$ , and thermal diffusion factor  $\alpha_i$ . The neutral atmosphere is characterized by a temperature  $T$ , gravity acceleration  $g\hat{a}_z$ , and velocity  $\mathbf{w}$ . The unit vector in the  $z$  direction is  $\hat{a}_z$ . The diffusion coefficient is found from

$$\frac{1}{D_i} = \sum_{k=1}^K \frac{1}{D_{ik}} \quad (2)$$

where  $D_{ik}$  is the mutual diffusion coefficient between the  $i$ th and the  $k$ th neutral gases. The effect of the injected gases on the diffusion coefficient is neglected. Equation (1) is valid only when the diffusing gas is a minor constituent.

The continuity equation for the  $i$ th neutral species is

$$\frac{\partial n_i}{\partial t} + \nabla \cdot (n_i \mathbf{w}_i) = P_i - L_i + S_i \quad (3)$$

where  $t$  is time,  $P_i$  and  $L_i$  are chemical production and loss terms, respectively, and  $S_i$  is the source function of gas  $i$ . The background atmosphere is assumed to be horizontally stratified. Consequently, the neutral wind velocity ( $\mathbf{w}$ ), the diffusion coefficient ( $D_i$ ), and the neutral temperature ( $T$ ) vary only along the altitude coordinate ( $z$ ). Under these conditions the diffusion equation is given by

$$\frac{\partial n_i}{\partial t} = - \left[ w_x \frac{\partial n_i}{\partial x} + w_y \frac{\partial n_i}{\partial y} + \frac{\partial (w_z n_i)}{\partial z} \right] + D_i \left[ \frac{\partial^2 n_i}{\partial x^2} + \frac{\partial^2 n_i}{\partial y^2} + \frac{\partial^2 n_i}{\partial z^2} + \frac{1}{H_i} \frac{\partial n_i}{\partial z} + n_i \frac{\partial (1/H_i)}{\partial z} \right]$$

$$+ n_i(1 + \alpha_i) \frac{\partial^2 \ln T}{\partial z^2} + (1 + \alpha_i) \frac{\partial n_i}{\partial z} \frac{\partial \ln T}{\partial z} \Bigg] + \frac{\partial D_i}{\partial z} \left[ \frac{\partial n_i}{\partial z} + \frac{n_i}{H_i} + (1 + \alpha_i) n_i \frac{\partial \ln T}{\partial z} \right] + P_i - L_i + S_i \quad (4)$$

The  $x$  and  $y$  derivatives are removed by Fourier transformation. The two-dimensional Fourier transform of  $n_i$  is

$$\bar{N}_i = \int_{-\infty}^{\infty} \int_{-\infty}^{\infty} n_i(x, y, z, t) \exp[-j2\pi(f_x x + f_y y)] dx dy$$

In the  $z$  direction an exponential transformation is applied. The exponential transformation is given by

$$\xi = -H_i \exp \left[ \frac{z_0 - z}{H_i} \right]$$

where  $z_0$  is the release altitude and  $H_i$  is a constant. The combination of the two-dimensional Fourier transform and exponential transform will be referred to as the Fourier-exponential transform (FET). With this transformation, (4) becomes

$$\begin{aligned} \frac{\partial \bar{N}_i}{\partial t} = & \bar{N}_i \left\{ -(2\pi)^2 D_i (f_x^2 + f_y^2) - j2\pi(f_x w_x + f_y w_y) \right\} \\ & + \frac{D_i}{H_i^2} \left( \xi \frac{\partial \bar{N}_i}{\partial \xi} + \xi^2 \frac{\partial^2 \bar{N}_i}{\partial \xi^2} \right) - \frac{\xi}{H_i} \frac{\partial \bar{H}_i}{\partial \xi} \\ & \cdot \left\{ -w_z + D_i \left[ \frac{1}{H_i} - (1 + \alpha_i) \frac{\xi}{H_i} \frac{\partial \ln T}{\partial \xi} \right] - \frac{\xi}{H_i} \frac{\partial D_i}{\partial \xi} \right\} \\ & + \bar{N}_i \left\{ \frac{\xi}{H_i} \frac{\partial w_z}{\partial \xi} - \frac{D_i \xi}{H_i} \frac{\partial (1/H_i)}{\partial \xi} - \frac{\xi}{H_i} \frac{\partial D_i}{\partial \xi} \right. \\ & \cdot \left[ \frac{1}{H_i} - (1 + \alpha_i) \frac{\xi}{H_i} \frac{\partial \ln T}{\partial \xi} \right] \\ & \left. + \frac{D_i(1 + \alpha_i)}{H_i^2} \left[ \xi \frac{\partial \ln T}{\partial \xi} + \xi^2 \frac{\partial^2 \ln T}{\partial \xi^2} \right] \right\} + \Phi_i - \mathcal{L}_i + S_i \quad (5) \end{aligned}$$

where  $\Phi_i$ ,  $\mathcal{L}_i$ , and  $S_i$  are the FET's of  $P_i$ ,  $L_i$ , and  $S_i$ , respectively.

To gain insight into why the exponential transform is used, consider the following. The diffusion coefficient  $D_i$  increases with altitude. The variable  $\xi^2$  decreases with altitude. Consequently, the factor  $(D_i \xi^2)/H_i^2$ , which multiplies  $\partial^2 \bar{N}_i / \partial \xi^2$ , may be made relatively constant in altitude with an appropriate selection of  $H_i$ .

It is convenient to partition the production, loss, and source functions as follows:

$$P_i - L_i + S_i = \sum_{m=1}^M F_{im}(z) n_m(x, y, z, t) - g_i(x, y, z, t) \quad (6)$$

where  $F_{im}$  is an altitude-dependent function which represents the chemical coupling of species  $n_m$  to the production or loss of species  $n_i$ . Fourier-exponential transformation yields

$$\Phi_i - \mathcal{L}_i + S_i = \sum_{m=1}^M F_{im} \bar{N}_m - \bar{G}_i(f_x, f_y, \xi) \quad (7)$$

where  $\bar{G}_i$  is the FET of  $g_i$ .

The complex quantities  $\bar{N}_i$  and  $\bar{G}_i$  are written in terms of real and imaginary parts:

$$\bar{N}_i = N_{Ri} + jN_{Ii} \quad \bar{G}_i = G_{Ri} + jG_{Ii} \quad (8)$$

Substituting (7) and (8) into (5) and equating the real and imaginary parts yield

$$\begin{aligned} \frac{\partial N_{Ri}}{\partial t} = & \frac{\partial^2 N_{Ri}}{\partial \xi^2} \left( \frac{D_i \xi^2}{H_i^2} \right) + \frac{\partial N_{Ri}}{\partial \xi} \left\{ \frac{D_i \xi}{H_i^2} + \frac{\xi w_z}{H_i} \right. \\ & - \frac{D_i \xi}{H_i} \left[ \frac{1}{H_i} - (1 + \alpha_i) \frac{\xi}{H_i} \frac{\partial \ln T}{\partial \xi} \right] - \frac{\xi}{H_i} \frac{\partial D_i}{\partial \xi} \Bigg\} \\ & + N_{Ri} \left\{ -(2\pi)^2 D_i (f_x^2 + f_y^2) + \frac{\xi}{H_i} \frac{\partial w_z}{\partial \xi} - \frac{D_i \xi}{H_i} \frac{\partial (1/H_i)}{\partial \xi} \right. \\ & - \frac{\xi}{H_i} \frac{\partial D_i}{\partial \xi} \left[ \frac{1}{H_i} - (1 + \alpha_i) \frac{\xi}{H_i} \frac{\partial \ln T}{\partial \xi} \right] \\ & + \frac{D_i \xi(1 + \alpha_i)}{H_i^2} \frac{\partial \ln T}{\partial \xi} \\ & \left. + \frac{D_i \xi^2(1 + \alpha_i)}{H_i^2} \frac{\partial^2 \ln T}{\partial \xi^2} \right\} + N_{Ri} 2\pi(f_x w_x + f_y w_y) \\ & + \sum_{m=1}^M F_{im} N_{Rm} + G_{Ri} \quad (9) \end{aligned}$$

plus a similar equation with  $N_{Ri}$  replaced with  $N_{Ii}$ ,  $N_{Ii}$  replaced with  $-N_{Ri}$ , and  $G_{Ri}$  replaced with  $G_{Ii}$ .

The coupled, second-order differential equations governing the expansion of several gases in a nonuniform, chemically reactive environment are summarized in terms of the matrix differential equation

$$\frac{\partial \bar{N}}{\partial t} = \bar{E} \frac{\partial^2 \bar{N}}{\partial \xi^2} + \bar{A} \frac{\partial \bar{N}}{\partial \xi} + \bar{B} \bar{N} - \bar{G} \quad (10a)$$

where

$$\bar{N} = [N_{R1}, N_{I1}, \dots, N_{RM}, N_{IM}]^T \quad (10b)$$

$$\bar{A} = \begin{bmatrix} A_1 & & & 0 \\ & A_1 & & \\ & & \ddots & \\ & & & A_M \\ 0 & & & & A_M \end{bmatrix} \quad (10c)$$

$$\bar{B} = \begin{bmatrix} F_{11} + B_1 & C & F_{12} & 0 & \dots & F_{1M} & 0 \\ -C & F_{11} + B_1 & C & F_{12} & & 0 & F_{1M} \\ F_{21} & -C & F_{22} + B_2 & C & & F_{2M} & 0 \\ 0 & F_{21} & -C & F_{22} + B_2 & & 0 & F_{2M} \\ \vdots & & & & \ddots & & \vdots \\ F_{M1} & 0 & & F_{M2} & 0 & F_{MM} + B_M & C \\ 0 & F_{M1} & 0 & F_{M2} & \dots & -C & F_{MM} + B_M \end{bmatrix} \quad (10d)$$

$$\bar{E} = \begin{bmatrix} E_1 & & & \\ & E_1 & & \\ & & \ddots & \\ & & & E_M \\ & & & & E_M \end{bmatrix} \quad (10e)$$

$$\bar{G} = [G_{R1}, G_{I1}, \dots, G_{RM}, G_{IM}]$$



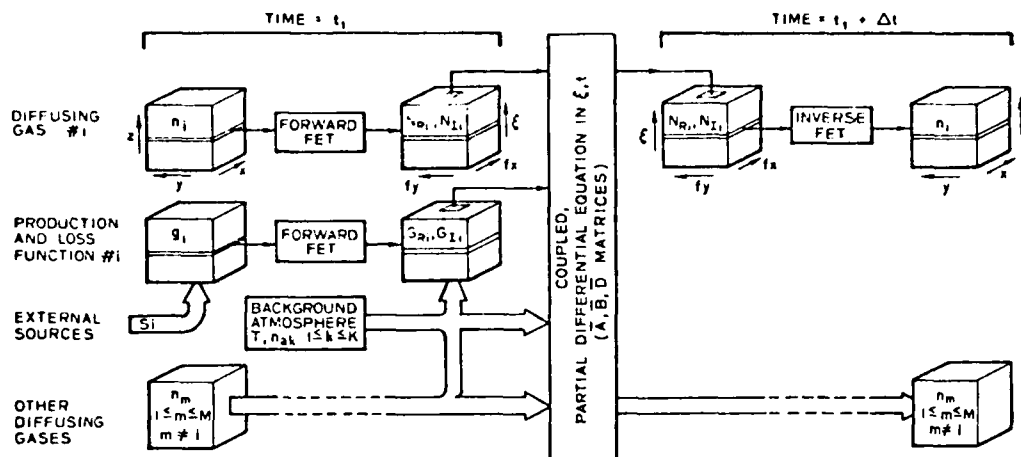


Fig. 1. Diagram of the numerical solution of the diffusion equation in three dimensions. FET stands for Fourier-exponential transform (see text).

The individual elements in the  $2M \times 2M$  matrices are

$$A_i = \frac{-\xi}{H_i} \left\{ -w_x + D_i \left[ \frac{1}{H_i} - \frac{1}{H_i} \right] \cdot \left( 1 + (1 + \alpha_i) \xi \frac{\partial \ln T}{\partial \xi} \right) - \frac{\xi}{H_i} \frac{\partial D_i}{\partial \xi} \right\} \quad (11a)$$

$$B_i = \frac{-\xi}{H_i} \left\{ -\frac{\partial w_x}{\partial \xi} + D_i \left[ \frac{\partial(1/H_i)}{\partial \xi} - (1 + \alpha_i) \cdot \left( \frac{\partial \ln T}{\partial \xi} + \frac{\xi}{H_i} \frac{\partial^2 \ln T}{\partial \xi^2} \right) \right] - D_i (2\pi)^2 (f_x^2 + f_y^2) - \frac{\xi}{H_i} \frac{\partial D_i}{\partial \xi} \left[ \frac{1}{H_i} - (1 + \alpha_i) \frac{\xi}{H_i} \frac{\partial \ln T}{\partial \xi} \right] \right\} \quad (11b)$$

$$C = 2\pi(f_x w_x + f_y w_y) \quad (11c)$$

$$E_i = D_i \xi^2 / H_i^2 \quad (11d)$$

and  $F_{i-}$  is defined by (7).

A few words about these equations are in order. The real and imaginary parts of  $\tilde{N}_i$  are coupled only by the parameter  $C$

in the  $B$  matrix. The parameter results from nonzero horizontal winds. If these winds are altitude independent, the transformation

$$\tilde{N}_i = \tilde{N}_i \exp \left[ \int_0^t j 2\pi (f_x w_x + f_y w_y) dt \right]$$

$$\tilde{G}_i = \tilde{G}_i \exp \left[ \int_0^t j 2\pi (f_x w_x + f_y w_y) dt \right]$$

results in a matrix with  $C = 0$ . This transformation is equivalent to following the gas diffusion in a reference frame which moves with the wind.

The equations presented in (10) have several properties which aid in their solution. The partial differential equations are second order in  $\xi$  and first order in  $t$ . The coefficient matrices  $\tilde{A}$  and  $\tilde{E}$  are diagonal and do not depend on  $\tilde{N}$ . Coupling between the elements in  $\tilde{N}$  occurs via multiplication with the  $\tilde{B}$  matrix and via the  $\tilde{G}$  matrix. Since  $\tilde{B}$  is independent of  $\tilde{N}$ , the only nonlinearity in (10) occurs through  $\tilde{G}$ .

In the solution of (10), however, the nonlinearity provided by  $\tilde{G}$  may be neglected. The relative importance of the nonlinearity varies according to the production and loss process represented by  $\tilde{G}$ . Complicated forms of  $\tilde{G}$  arise from chemical

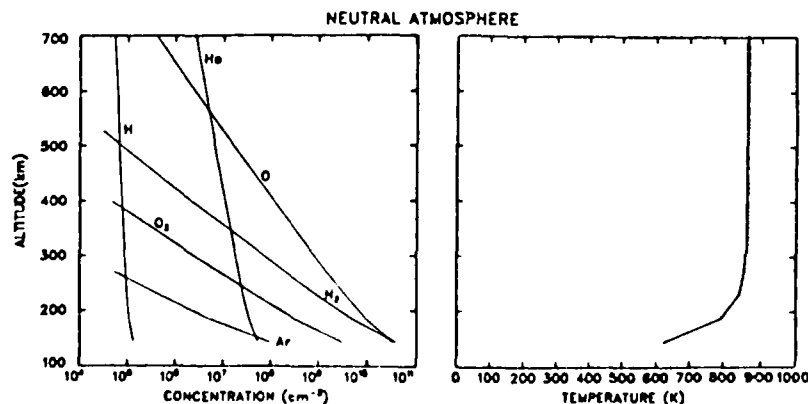


Fig. 2. Composition and temperature of the model atmosphere. The atmosphere is representative of mid-latitude, medium-solar-activity, nighttime conditions.

TABLE 1. Mutual Diffusion Coefficients From  $D_{ik} = A_{ik}T^{3/2}/n_k \text{ cm}^2/\text{s}$ 

	H	He	O	N <sub>2</sub>	O <sub>2</sub>	Ar
H <sub>2</sub> coefficients						
$A_{12}$	8.31[17]	6.45[17]	3.11[17]	2.8[17]	3.07[17]	2.89[17]
$S_{12}$	0.728	0.716	0.749	0.74	0.732	0.729
OH coefficients						
$A_{13}$	5.2[17]	3.12[17]	1.66[17]	0.902[17]	0.902[17]	0.514[17]
$S_{13}$	0.708	0.749	0.75	0.774	0.774	0.841
CO <sub>2</sub> coefficients						
$A_{14}$	1.07[17]	2.42[17]	0.548[17]	0.658[17]	0.577[17]	0.422[17]
$S_{14}$	0.597	0.720	0.841	0.752	0.749	0.795

OH diffusion coefficients are found from O diffusion coefficients by  $D_{OH,i}/D_{O,i} = 0.914[(1 + m_i/m_{OH})(1 + m_i/m_O)]^{1/2}$  [McKenzie et al., 1973], and  $[v] = 10^5$ . Read 8.31[17] as  $8.31 \times 10^{17}$ .

reactions between two different diffusing gases. This chemical coupling is generally weak for the gases of interest. Consequently,  $G$  is assumed to be a function of  $N$  at the beginning of each step in the solution. With this approximation, (10) is a set of linear, coupled partial differential equations. Before these equations can be solved, the initial conditions and the boundary conditions must be specified.

### 3. GAS RELEASE SOURCE FUNCTIONS AND INITIAL CONDITIONS

The injection of a neutral gas may be incorporated into the simulation either as (1) an initial condition for point sources or short extended sources or as (2) a source term  $S_i$  (see (3)) for long-duration extended sources. Point sources are considered first. During early times (time of release less than one collision time) a tenuous gas cloud will undergo free molecular expansion. The neutral gas concentration in space and time for this type of expansion is given by

$$n(x, y, z, t) = N_0 \left[ \exp \frac{-(x^2 + y^2 + z^2)}{(c_0 t)^2} \right] [(\pi c_0 t)^3]^{-1}$$

[Bienkowski, 1964], where  $N_0$  is the number of molecules released,  $c_0 = (2kT_0/m)^{1/2}$  is the speed of sound inside the gas at the time of release,  $T_0$  is the initial gas temperature,  $m$  is the molecular mass, and  $t$  is the time since release.

At later times (typically 10 collision times or greater), diffusive expansion applies. The solution for diffusive expansion of a point release in a uniform atmosphere is

$$n(x, y, z, t) = \frac{N_0 \exp [-(x^2 + y^2 + z^2)/(4D_0 t)]}{(4\pi D_0 t)^{3/2}}$$

where  $D_0$  is the diffusion constant [e.g., Jost, 1960].

Both the initial, free-molecular expansion and the later diffusive expansion have the form

$$n_p(x, y, z) = \frac{N_0 \exp [-(x^2 + y^2 + z^2)/(2\sigma^2)]}{(2\pi\sigma^2)^{3/2}} \quad (12)$$

where  $\sigma$  is the 'radius' of the expanding gas at the start of the simulation. Consequently, this expression is used for the initial distribution of a point release in the numerical simulation. All simulations of points releases are started three atmospheric collision times after release.

A line source is considered next. To model a source moving in a straight line, one can break the release into an infinite sequence of point releases. This is done by Bernhardt [1976] with the result

$$n_l(x, y, z, t) = F_0 \int_0^t \exp \left\{ - \left( x - V_x \left( \frac{t_\mu}{2} - \gamma \right) - X_c \right)^2 \right.$$

$$- \left( y - V_y \left( \frac{t_\mu}{2} - \gamma \right) - Y_c \right)^2 - \left. \left( z - V_z \left( \frac{t_\mu}{2} - \gamma \right) - Z_c \right)^2 \right\} / 4D_i(t_0 + t_\mu - \gamma) \Bigg] / [4\pi D_i(t_0 + t_\mu - \gamma)]^{3/2} d\gamma \quad (13)$$

where  $F_0$  is the flow rate of the source;  $t_\mu$  is the duration of the source;  $t_0$  is the time that the gas takes to thermalize with the background atmosphere;  $D_i$  is the injected gas diffusion coefficient;  $V_x$ ,  $V_y$ , and  $V_z$  are the velocity components of the moving source; and  $X_c$ ,  $Y_c$ , and  $Z_c$  are the centers of the line source. Each segment of the line release is delayed by time  $t_0$ , which is taken to be three atmospheric collision times.

The long-duration, extended source requires the continual injection of material during the time-varying simulation. To accomplish this, the source term  $S_i$  in the continuity equation (3) is used. The source term for a line source has the form

$$S_i(x, y, z, t) = \frac{F_0}{(2\pi\sigma^2)^{3/2}} \exp \left\{ - \left[ x - V_x \left( \frac{t_\mu}{2} - t \right) - X_c \right]^2 \right.$$

$$- \left[ y - V_y \left( \frac{t_\mu}{2} - t \right) - Y_c \right]^2 - \left. \left[ z - V_z \left( \frac{t_\mu}{2} - t \right) - Z_c \right]^2 \right\} / 2\sigma^2 \quad 0 \leq t \leq t_\mu \quad (14)$$

where the variables have already been defined in (12) and (13). It is computationally easier to include the gas source as an initial condition rather than as a source term in the continuity equation.

### 4. BOUNDARY CONDITIONS

The solution of any second-order partial differential equation requires boundary conditions. The boundary conditions at the horizontal border of the solution space are implicitly specified by using the two-dimensional finite Fourier trans-

TABLE 2. Relative Importance of Thermal Diffusion

Altitude, km	$1/H_0, \text{ m}^{-1}$	$(1 + \alpha_1) \partial \ln T / \partial z, \text{ m}^{-1}$
150	$3.5 \times 10^{-6}$	$7 \times 10^{-6}$
225	$2.7 \times 10^{-6}$	$7 \times 10^{-6}$
300	$2.6 \times 10^{-6}$	$8 \times 10^{-6}$
375	$2.5 \times 10^{-6}$	$8 \times 10^{-6}$
450	$2.4 \times 10^{-6}$	$8 \times 10^{-6}$

TABLE 3. Neutral Gas Release Simulations

Simulation	Species	Amount Released, molecules	Altitude, km	Type of Release	Wind Velocity, m/s	Figure Reference
1	H <sub>2</sub>	3.[27]	300	point source	0	3-6
2	CO <sub>2</sub> H <sub>2</sub>	3.[27] 3.[27]	250	line source $v_x = 8$ km/s $t_w = 5$ s	0	7
3	CO <sub>2</sub>	3.[27]	160	point source	Given in Figure 8	9
4	CO <sub>2</sub>	3.[27]	160	line source $v_x = 1$ km/s $v_z = 1$ km/s $t_w = 30$ s	Given in Figure 8	10

Note that [x] = 10<sup>3</sup>. Read 3.[27] as 3 × 10<sup>27</sup>.

form. This transform assumes that the solution is periodic in two dimensions with periods equal to the horizontal dimensions of the solution space. Care must be taken to insure that the solution does not expand into these borders.

The upper and lower boundary conditions to the second-order partial differential equation in  $z$  and  $t$  are specified by the equation

$$\bar{A}_0 \frac{\partial \bar{N}}{\partial \xi} + \bar{B}_0 \bar{N} - \bar{G}_0 = 0 \quad (15)$$

A simple condition would be to force the densities to zero by letting  $\bar{A}_0 = 0$ .

$$\bar{B}_0 = \begin{bmatrix} 1 & 1 & 0 \\ 0 & & 1 \end{bmatrix}$$

and  $\bar{G}_0 = 0$ . This condition requires an infinite sink of particles at the boundaries.

Another possible condition requires that the flux of particles,  $n_i w_{zi}$ , go to zero at the boundaries. From (1),

$$n_i w_{zi} = n_i w_z - D_i \frac{1}{H_i} + (1 + \alpha_i) \frac{\partial \ln T}{\partial z} - D_i \frac{\partial n}{\partial z} = 0$$

With this assumption (and the exponential transform) the matrix elements in (15) become

$$A_{0i} = \frac{\xi}{H_i} D_i$$

$$B_{0i} = w_z + D_i \left[ -\frac{1}{H_i} + \frac{\xi}{H_i} (1 + \alpha_i) \frac{\partial \ln T}{\partial z} \right]$$

$$G_{0i} = 0$$

This boundary condition does not allow any particles to leave the solution space.

The boundary conditions described above require infinite velocity and zero velocity, respectively, at the top and the bottom of the solution space. A condition between these two extremes is used in the present simulation.

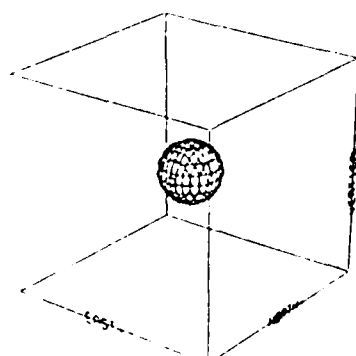
The diffusion velocity at the borders is specified by

$$w_z = (z - z_0)/2t \quad (16)$$

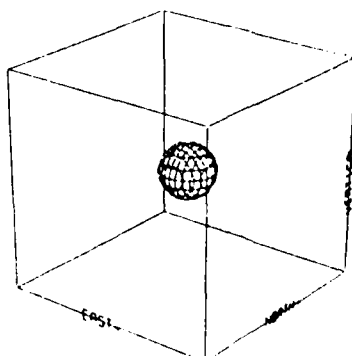
where  $z_0$  is the altitude of release at time  $t = 0$ . Equation (16) implies that the average velocity that a particle has after moving a distance  $z - z_0$  in time  $t$  is half the velocity that it would have if it encountered no collisions. This is indeed the gas velocity for diffusion in a uniform atmosphere [Bernhardt, 1976].

Substitution of (16) into (1) yields

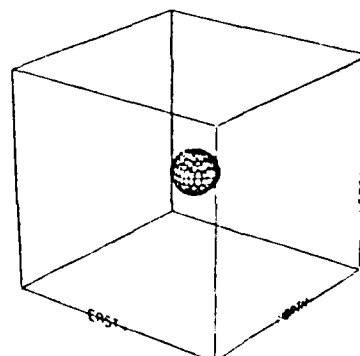
$$n_i \left\{ w_z - \frac{(z - z_0)}{2t} - D_i \left[ \frac{1}{H_i} + (1 + \alpha_i) \frac{\partial \ln T}{\partial z} \right] \right\} - D_i \frac{\partial n}{\partial z} = 0$$



300.0 km CUBE CENTERED AT 300.0 km ALTITUDE  
TIME AFTER RELEASE: 31.9 sec  
H<sub>2</sub> CONCENTRATION AT SURFACE: 3.0[8] cm<sup>-3</sup>



300.0 km CUBE CENTERED AT 300.0 km ALTITUDE  
TIME AFTER RELEASE: 31.9 sec  
OH CONCENTRATION AT SURFACE: 0.3[3] cm<sup>-3</sup>



300.0 km CUBE CENTERED AT 300.0 km ALTITUDE  
TIME AFTER RELEASE: 31.9 sec  
CO<sub>2</sub> CONCENTRATION AT SURFACE: 0.3[8] cm<sup>-3</sup>

Fig. 3. Simultaneous expansion of 3 × 10<sup>27</sup> molecules of CO<sub>2</sub> and 3 × 10<sup>27</sup> molecules of H<sub>2</sub> released at 300-km altitude. The reaction between O and H<sub>2</sub> produces the OH radical. At early times the expansion is nearly spherical.

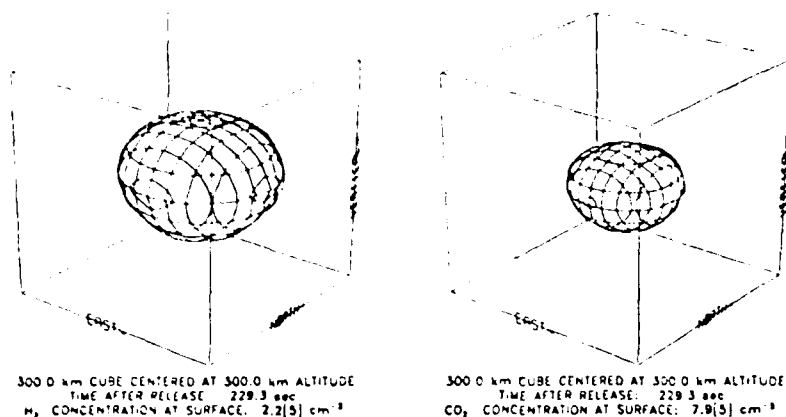


Fig. 4 Late time expansion of  $3 \times 10^{27}$  molecules of  $\text{CO}_2$  and  $\text{H}_2$  at 300-km altitude. The nonspherical expansion is due to the altitude variation in the background atmosphere.

The matrix coefficients for (15) become

$$A_{ii} = D_i \frac{\xi_i}{H_i}$$

$$B_{0i} = w_i + \frac{H_i}{2t} \left[ \ln \left( \frac{\xi_i}{H_i} \right) \right] \quad (17)$$

$$+ D_i \left[ \frac{\xi_i}{H_i} (1 + \alpha_i) \frac{\partial \ln T}{\partial \xi_i} - \frac{1}{H_i} \right]$$

$$G_{0i} = 0$$

With these boundary conditions the solution to (11) is computed numerically.

### 5. SOLUTION OF THE THREE-DIMENSIONAL DIFFUSION EQUATIONS

The procedure for the solution of (10) is displayed in Figure 1. Each diffusing gas concentration  $n_i$  and function  $g_i$  is stored in a memory block with dimensions corresponding to the  $x$ ,  $y$ , and  $z$  coordinate axes. The gas concentration block is filled with either initial values (at the start of a simulation) or values from the solution at a previous time ( $t_i$ ). The source function  $S_i$  is determined from external inputs. If the source function has an analytic Fourier transform, the numerical fast Fourier transform (FFT) will not be necessary. For instantaneous releases the source function is expressed as an initial condition, and  $S_i$  is neglected (see section 3).

Horizontal slabs in these blocks are Fourier-exponential-transformed and repacked into memory blocks corresponding to  $f_x$ ,  $f_y$ , and  $\xi$  coordinate space. The elements of the production-loss-source function ( $G_{0i}$ ,  $G_{0i}$ ) arise from chemical reactions between the individual diffusing space with an additional term due to external sources. The  $A$ ,  $B$ , and  $E$  matrices are determined from the background atmospheric parameters.

Vertical columns in  $z$  are retrieved from data memory blocks at fixed values of  $f_x$  and  $f_y$ . These are used, along with the partial differential equation given in (10), to find values of  $N_{0i}$  and  $N_{1i}$  at later times. The coupled, vector set of linear, second-order (parabolic) partial differential equations are solved by generalizing the method of Crank and Nicolson [1947].

The new solution vector is placed in an output memory block in the form of a 'column' at  $f_x$  and  $f_y$ . The process is continued until the updated columns have been determined for all spatial frequencies.

The inverse FET converts each slab in  $f_x$ ,  $f_y$ , and  $\xi$  space into one at the  $x$ ,  $y$ , and  $z$  spatial coordinates. The output memory block contains the neutral gas densities at time  $(t_i + \Delta t)$ . The solution process is repeated using time increments  $\Delta t$  which are proportional to  $1/t$ .

In the above description it has been conceptually convenient to consider four separate memory blocks: (1)  $x$ ,  $y$ ,  $z$  space at time  $t_i$ ; (2)  $f_x$ ,  $f_y$ ,  $\xi$  space at time  $t_i$ ; (3)  $f_x$ ,  $f_y$ ,  $\xi$  space at time  $t_i + \Delta t$ ; and (4)  $x$ ,  $y$ ,  $z$  space at time  $t_i + \Delta t$ . Actually, these four blocks should use the same memory locations to reduce data storage requirements.

Because of the uncertainties at the boundaries (see section 4) an adaptive grid is adopted. As the concentration of the neutral gases becomes significant near the edges of the solution grid, this space is increased by redefining the spacing of the

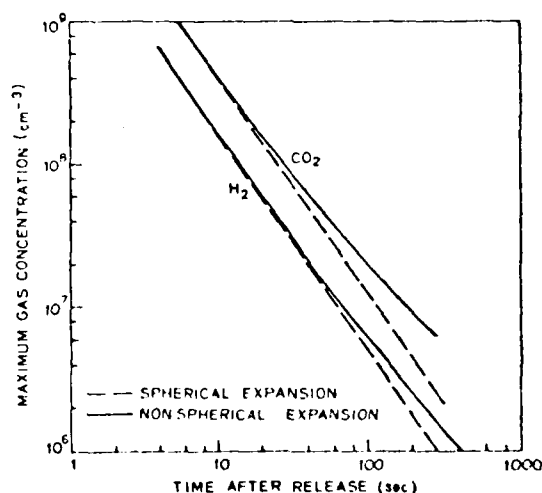


Fig. 5 Temporal variation in the maximum, central concentration of the expanding  $\text{CO}_2$  and  $\text{H}_2$  gas clouds. The point of maximum concentration drops in altitude with time. The concentration at this point is greater than the gas concentration for expansion in a uniform atmosphere.

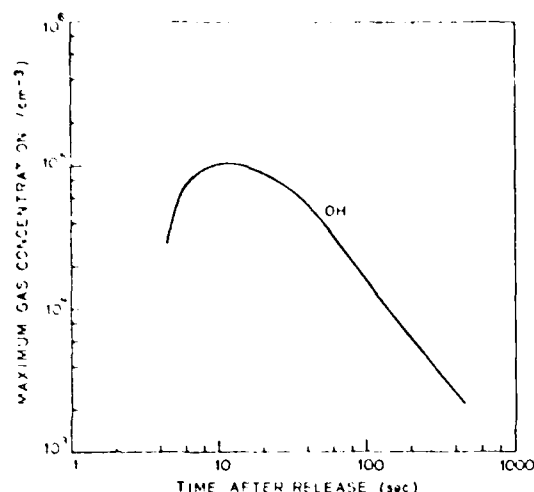


Fig. 1. Temporal variation in the maximum OH concentration. The initial rise in concentration is caused by reaction between atomic oxygen and the released  $H_2$ . The fall in the concentration is due mainly to diffusion.

grid. Thus the solution grid follows the outer edges of the diffusive expansion, containing the gases within its boundaries.

#### 6. SIMULATION OF $CO_2$ , $H_2$ , AND OH DIFFUSIVE EXPANSIONS

The procedure outlined in the previous sections is used to model carbon dioxide and/or molecular hydrogen expansions.  $CO_2$  and  $H_2$  were chosen because the large difference between their molecular masses produces a noticeable difference in their rates of expansion. Hydrogen is of special interest because it reacts with atomic oxygen in the atmosphere, producing the hydroxyl radical. All three substances ( $CO_2$ ,  $H_2$ , and OH) cause plasma depletions when injected into the  $F_2$  layer ionosphere [Bernhardt, 1976].

The neutral atmosphere used in the simulation is the empirical global model obtained from mass spectrometer-incoherent scatter (MSIS) data by Hedin *et al.* [1977a, b]. Figure 2 illustrates the composition and temperature profiles of the model neutral atmosphere.

The mutual diffusion coefficients for the diffusing gases ( $CO_2$ ,  $H_2$ , and OH) are found from the formula

$$D_{ik} = A_{ik} T^{S_{ik}} n_k$$

where  $T$  is the neutral temperature,  $n_k$  is the concentration of the  $k$ th atmospheric species, and  $A_{ik}$  and  $S_{ik}$  are given in Table 1. The diffusion coefficient for OH is found by scaling the diffusion coefficient for O, according to their relative masses (see footnote to Table 1). The numerical values for all diffusion coefficients are based on laboratory measurements tabulated by Mason and Marrero [1970] and Banks and Kockarts [1973]. Ion-neutral collisions have less than a 0.1% effect on the diffusion and are therefore neglected.

The values of the thermal diffusion factors are given as follows:  $\alpha_{OH} = -0.25$ ,  $\alpha_{OH} = 0.0$ , and  $\alpha_{OH} = 0.1$ . These factors were theoretically derived by Chapman and Cowling [1970].

In regions of large temperature gradients the effects of thermal diffusion become important. A comparison of the factors, which multiply  $n_i$  and  $i n_i / \partial z$  in (4), shows that thermal diffusion should be considered if

$$\frac{1}{H_i} \lesssim (1 + \alpha_i) \frac{\partial \ln T}{\partial z}$$

Table 2 illustrates the altitude dependence of the quantities for a simulation of an  $H_2$  release into the atmosphere given in Figure 2. Thermal diffusion becomes important only for releases below 200-km altitude.

The chemical reactions governing the releases are taken from Zinn and Sutherland [1975]. Chemical reactions between carbon dioxide and the upper atmosphere constituents are negligible. A molecular hydrogen release, however, produces OH,  $O_2$ , and  $H_2O$  by the following set of reactions:



$$k_a = 2.6 \times 10^{-11} \left( \frac{T}{300} \right)^{0.01} e^{-4652/T} \text{ cm}^3/\text{s}$$

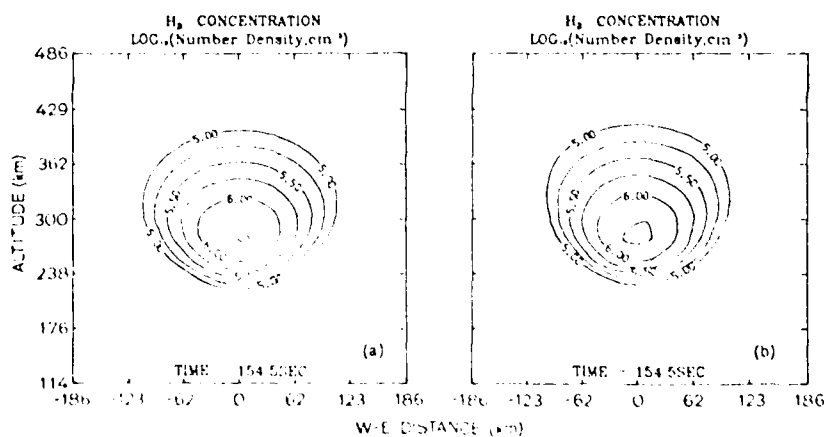
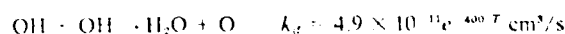
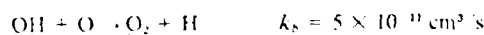


Fig. 2. Comparison of the (a) numerical and (b) approximate, analytic solutions to the diffusion equation 154.5 s after release.

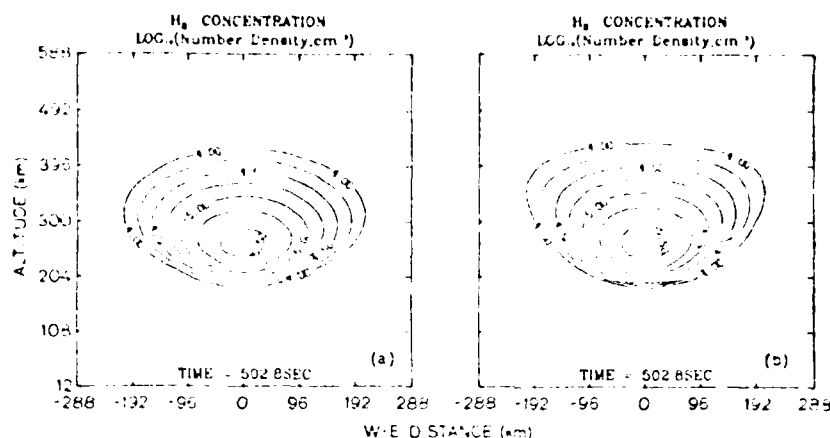


Fig. 8. Comparison of the (a) numerical and (b) approximate, analytic solutions to the diffusion equation 507.8 s after release.

For  $\text{CO}_2$  the production and loss terms in (3) are zero. The functions  $P_i$  and  $L_i$  for the hydrogen release are

$$\begin{aligned} P_1 &= 0 & L_1 &= k_a n_1 n_0 \\ P_2 &= k_a n_1 n_0 & L_2 &= (k_s n_0 + k_i n_1 + k_a n_2) n_2 \end{aligned}$$

where the subscripts 1 and 2 refer to the  $\text{H}_2$  and  $\text{OH}$ , respectively, and  $n_0$  is the atomic oxygen concentration.

The neutral gas expansions are illustrated as isopycnic contour plots or in terms of three-dimensional surface plots. The gas cloud is outlined by a surface on which the concentration is 10% of that of the central cloud.

The conditions for four simulations produced by the model are listed in Table 3. Simulation 1 modeled the point release of  $3 \times 10^{27}$  molecules of  $\text{CO}_2$  and  $\text{H}_2$  at 300-km altitude. The neutral wind velocity was set to zero. Figure 3 illustrates the diffusive expansion 31.9 s after release. The  $\text{CO}_2$  cloud is more concentrated but smaller in size than the faster diffusing  $\text{H}_2$  cloud. The maximum  $\text{OH}$  concentration is 0.2% of the maximum  $\text{H}_2$  concentration. At the early times of expansion the clouds are spherical. Figure 4 illustrates the  $\text{H}_2$  and  $\text{CO}_2$  gases almost 4 min after release. The increase in the neutral diffusion coefficient with altitude causes nonspherical expansions at this later time.

Figure 5 illustrates the effect of nonspherical expansion on the maximum concentration inside the expanding clouds. The maximum concentration for spherical expansions is proportional to  $t^{-3/2}$  as shown by the dashed lines in the figure. The actual expansions deviate from the dashed lines for times greater than 1 min.

The buildup and decay of the  $\text{OH}$  radical are illustrated in Figure 6. The  $\text{OH}$  concentration reaches a maximum value of  $1.05 \times 10^7 \text{ cm}^{-3}$  at 11 s after the  $\text{H}_2$  release. The  $\text{OH}$  concentration never becomes more than 0.3% of the  $\text{H}_2$  concentration for releases at 300-km altitude.

The results of simulation 1 are compared to an approximate analytic solution for diffusion in an exponential atmosphere. The purpose of this comparison is to provide an estimate for conditions when the approximate, analytic expression can be used.

The approximate expression for the gas concentration resulting from a point release is given by

$$n(x, y, z, t) = \frac{N_0}{(4\pi D_0 t)^{3/2}} \exp \left[ -z \left( \frac{3}{4H_0} + \frac{1}{2H_1} \right) \right] - \frac{H_0^2 \{1 - \exp[-z/(2H_1)]\}^2}{D_0 t}$$

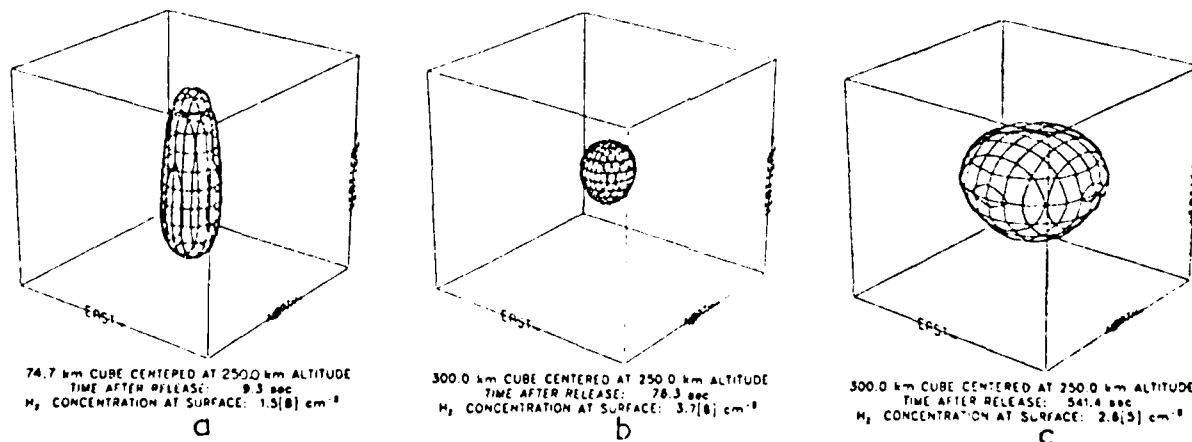


Fig. 9. Expansion of a vertical  $\text{H}_2$  line source centered at 250 km altitude.

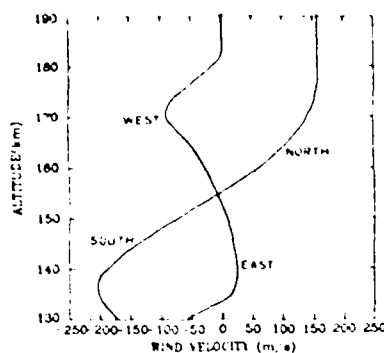


Fig. 10. Zonal and meridional winds used in the simulations illustrated in Figures 11 and 12.

$$\frac{(x^2 + y^2) \exp[-z/(2H_0)]}{4D_0 t} - \left( \frac{1}{H_2} - \frac{1}{H_1} \right)^2 \frac{D_0 t \exp[-z/(2H_0)]}{4}$$

where  $N_0$  is the number of molecules released,  $D_0$  and  $H_0$  are the diffusive coefficient and scale height, respectively, of the atmosphere at the point of release, and  $H_1 = kT/mg$  is the released gas scale height.

This formula was derived by Bernhardt [1976] and has been used by Bernhardt *et al.* [1975], Bernhardt and da Rosa [1977], Mendillo and Forbes [1978], and Anderson and Bernhardt [1978] to describe the diffusive flow of point releases.

The comparison is made for the  $H_2$  release at 300-km altitude because the effects of thermal diffusion and chemical reaction are minimal. The two solutions are identical for the first 40 s. At 154.5 s after the release the peak concentration of the analytic solution is larger than that of the numerical solution. Also, the analytic solution extends upward slightly more than the numerical solution (Figure 7).

At later times the difference between the analytic and numerical solutions becomes more pronounced. Most of this difference is in the cloud topside. Figure 8 illustrates the numerical and analytic solutions 507.8 s after release. We find the analytic solution to be a useful approximation to the numerical solution for the first 10 min for a release near 300-km altitude.

The results of simulation 2 are shown in Figure 9. An  $H_2$  source moves vertically with a velocity of 8 km/s, releasing vapor at a constant rate of  $6 \times 10^{26}$  molecules/s from 230-km to 270-km altitude. Since the release starts at low altitudes and moves upward, the gas cloud bulges at the bottom during the early times of expansion (Figure 9a). For expansion times greater than 20 s the nonuniformity of the background atmosphere causes a bulge in the upper portion of the cloud. Many minutes into the expansion the gas loses all memory of its initial structure (Figure 9c).

The effects of neutral winds are demonstrated in the next two simulations. The neutral wind profiles used in the simulation (illustrated in Figure 10) are taken from measurements at Sondre Stromfjord Station (67.02°N, 50.17°W) on December 17, 1974, as reported by Pereira *et al.* [1978]. The strong shear in this wind has a striking effect on the neutral gas expansion.

Figure 11 illustrates the effect of a nonuniform neutral wind on this diffusion of  $3 \times 10^{27}$  molecules of  $CO_2$  released at a point 160 km in altitude. The neutral wind shear elongates the initially spherical gas expansion.

The last simulation illustrates the effect of the strong neutral wind shear on an elongated source. A  $CO_2$  source moves at 45° to the vertical with a velocity of 1.4 km/s, releasing vapor from 145-km to 175-km altitude at a rate of  $1 \times 10^{26}$  molecules/s. The neutral wind pattern changes the initially west-east gas distribution into a north-south distribution covering tens of kilometers (Figure 12).

## 7. SUMMARY AND CONCLUSIONS

A numerical model of neutral diffusion has been developed for the study of gas flow in a nonuniform, chemically reactive environment. The three-dimensional model permits realistic simulation of neutral gas expansions under a wide range of atmospheric conditions.

Recently, Anderson and Bernhardt [1978] have shown that molecular hydrogen releases into the equatorial ionosphere will produce ionospheric depletions which can trigger a Rayleigh-Taylor type gravitational instability. They also have shown that  $H_2$  releases will produce airglow at 6300 Å and 3060 Å due to excited O and OH. Their study was, however, limited to point releases of  $H_2$  using the analytic formulation for gas expansion by Bernhardt [1976]. Similar limitations were experienced by Bernhardt *et al.* [1975] and Bernhardt and da Rosa [1977] in their studies of mid-latitude ionospheric modification. Research is currently underway using the three-

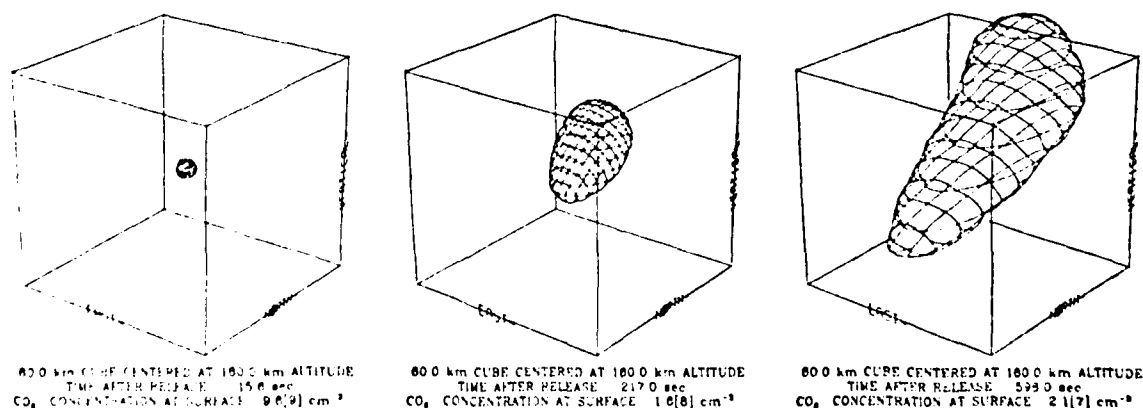


Fig. 11. Distortion of a spherical release by a wind shear.

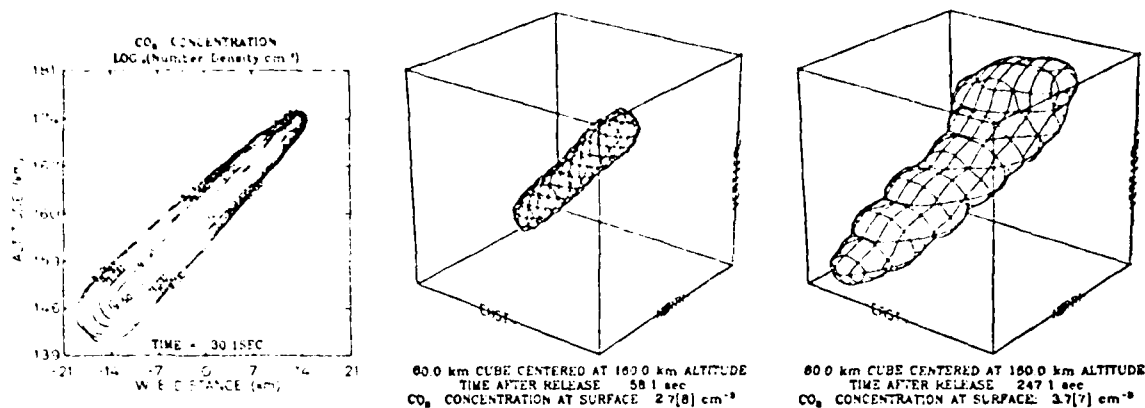


Fig. 12. Effect of a wind shear on an elongated release.

dimensional neutral expansion model described here along with the existing ionospheric models.

Optical observations of neutral chemicals released into the upper atmosphere have provided information about the wind velocities and diffusion coefficients in this region. For example, trimethyl aluminum reacts with atomic oxygen in the atmosphere, leaving a chemiluminescent trail [Rosenberg *et al.*, 1963]. Simulation of chemiluminescent reactions is analogous to the simulation of the molecular hydrogen and atomic oxygen reaction described here. Interpretation of chemical tracer experiments may be aided by use of the three-dimensional diffusive expansion model.

**Acknowledgments.** The author would like to thank A. V. da Rosa, D. N. Anderson, R. G. Roble, and M. C. Kelley for many helpful discussions. This research was supported by the Office of Naval Research contract N00014-77-C-0586. A majority of the computing was done at the National Center for Atmospheric Research, which is sponsored by the National Science Foundation. This study was presented at the Summer Computer Simulation Conference, Newport Beach, California, July 24-26, 1978.

The Editor thanks R. W. Schunk and M. Mendillo for their assistance in evaluating this paper.

#### REFERENCES

- Anderson, D. A., and P. A. Bernhardt, Modeling the effects of an H<sub>2</sub> gas release on the equatorial ionosphere, *J. Geophys. Res.*, **83**, 4777, 1978.
- Banks, P. M., and G. Kockarts, *Aeronomical Vols. A, B*, Academic, New York, 1973.
- Bernhardt, P. A., The response of the ionosphere to the injection of chemically reactive vapors, *Tech. Rep. 17*, Stanford Electron. Lab., Stanford Univ., Stanford, Calif., 1976.
- Bernhardt, P. A., and A. V. da Rosa, A refracting radiotelescope, *Radio Sci.*, **12**, 327, 1977.
- Bernhardt, P. A., C. G. Park, and P. M. Banks, Depletion of the F2 region ionosphere and the protonosphere by the release of molecular hydrogen, *Geophys. Res. Lett.*, **2**, 341, 1975.
- Bienkowski, G., Collisionless expansion of gas clouds in the presence of an ambient gas, *Phys. Fluids*, **7**, 352, 1964.
- Chapman, S., and T. G. Cowling, *The Mathematical Theory of Non-uniform Gases*, Cambridge University Press, New York, 1970.
- Crank, J., and P. Nicolson, A practical method for numerical evaluation of solutions of partial differential equations of the heat-conduction type, *Proc. Cambridge Phil. Soc.*, **43**, 50, 1947.
- Forbes, J. M., and M. Mendillo, Diffusive aspects of ionospheric modification by the release of highly reactive molecules into the F-region, *J. Atmos. Terr. Phys.*, **38**, 1299, 1976.
- Hedin, A. E., J. E. Salah, J. V. Evans, C. A. Reber, G. P. Newton, N. W. Spencer, D. C. Kayser, D. Alcayde, P. Bauer, L. Cogger, and J. P. McClure, A global thermospheric model based on mass spectrometer and incoherent scatter data, MSIS 1, N<sub>2</sub> density and temperature, *J. Geophys. Res.*, **82**, 2139, 1977a.
- Hedin, A. E., C. A. Reber, G. P. Newton, N. W. Spencer, H. C. Brinton, H. G. Mayr, and W. E. Potter, A global thermospheric model based on mass spectrometer and incoherent scatter data, MSIS 2, Composition, *J. Geophys. Res.*, **82**, 2148, 1977b.
- Jost, W., *Diffusion*, Academic, New York, 1960.
- Mason, E. A., and T. R. Marrero, *The Diffusion of Atoms and Molecules, Advances in Atomic and Molecular Physics*, vol. 6, edited by D. R. Bates, p. 155, Academic, New York, 1970.
- McKenzie, A., M. E. R. Mulcahy, and J. R. Steven, Kinetics of decay of hydroxyl radical at low pressure, *J. Chem. Phys.*, **59**, 3244, 1973.
- Mendillo, M., and J. M. Forbes, Artificially created holes in the ionosphere, *J. Geophys. Res.*, **83**, 151, 1978.
- Pereira, E., M. C. Kelley, D. Rees, I. S. Mikkelsen, T. S. Jorgensen, and T. J. Fuller-Roswell, Coupling between magnetospheric processes and the neutral atmosphere in the dayside auroral oval, submitted to *J. Geophys. Res.*, 1978.
- Poirier, R. V., and R. W. Carr, Jr., The use of tubular flow reactors of kinetic studies over extended pressure ranges, *J. Phys. Chem.*, **75**, 1593, 1971.
- Rosenberg, N. W., D. Colomb, and E. F. Allen, Jr., Chemiluminescence of trimethyl aluminum released into the upper atmosphere, *J. Geophys. Res.*, **68**, 5895, 1963.
- Schunk, R. W., On the dispersal of artificially-injected gases in the nighttime atmosphere, *Planet. Space Sci.*, **26**, 605, 1978.
- Vincenti, W. G., and C. H. Kruger, *Introduction to Physical Gas Dynamics*, John Wiley, New York, 1965.
- Yu, K., and M. M. Klein, Diffusion of small particles in a nonuniform atmosphere, *Phys. Fluids*, **1**, 651, 1964.
- Zinn, J., and C. D. Sutherland, Stratospheric chemistry computations, *Rep. LA-6111-MS*, Los Alamos Sci. Lab., Los Alamos, N. Mex., Oct. 1975.

(Received May 8, 1978;  
revised July 31, 1978;  
accepted September 26, 1978.)



### C. GAS DYNAMICS OF VAPOR RELEASES

We have investigated the flow of vapors released into the upper atmosphere. Our previous work (see Section B) presented a three-dimensional model of neutral gas diffusion. This work considered the transition from a collisionless expansion (immediately after release) to a collision-dominated (i.e., diffusive) flow. This study was necessary to determine the stopping distance of vapors released into the tenuous upper atmosphere where the mean free path is approximately  $10^5$  meters at 400 km altitude.

The details of our new model are presented in the following paper which was published in the Journal of Geophysical Research. Briefly, the vapor flow process is described by the Boltzmann equation with a collision term representing relaxation of the injected vapor to the kinetic state of the background atmosphere. Simulations show significant differences between supersonic and subsonic vapor releases. Lower speed releases take a longer time to become collisionally dominated. High speed flows experience large heating due to collisions with the background atmosphere. The new model permits prediction of the expansion of vapors that are released into the upper atmosphere from supersonic vehicles.

# High-Altitude Gas Releases: Transition From Collisionless Flow to Diffusive Flow in a Nonuniform Atmosphere

PAUL A. BERNHARDT

*RadioScience Laboratory, Stanford University, Stanford, California 94305*

Vapors, released at high altitudes from rockets or the Space Shuttle, may travel many hundreds of kilometers before coming to rest. An understanding of the effects produced by these releases requires knowledge of the vapor flow. In the tenuous upper atmosphere, the injected gases expand from a collisionless to a collision-dominated state. In this paper, this process is described by the Boltzmann equation with the Krook collision integral. The theory is applied to supersonic releases into a nonuniform atmosphere. The model predicts elongation and heating of the vapor trails due to collisions. The theory may be applied to a wide range of experiments whose objectives include the formation of ionospheric depletions, the triggering of instabilities, the generation of gravity waves, and the injection of neutrals as luminous tracers.

## 1. INTRODUCTION

The flow of vapors released into the upper atmosphere is governed by three types of expansions. During the early stages, collisions between the expanding vapor molecules dominate the flow. This expansion is called self-continuum flow. As the expanding cloud becomes tenuous, self-collisions become rare and in a vacuum the expansion is free streaming or collisionless. At some time in the expansion, collisions with the background atmosphere become important. When interaction with the background atmosphere controls the flow, a state of diffusive expansion exists.

The nature of the expansion depends on the amount of material released and on the particle concentration of the background atmosphere. In a dense atmosphere, the expansion interacts with the background atmosphere to form Rankine-Hugoniot shock waves. These shock waves separate the background atmosphere from the core of the expansion. When releases are made at high altitudes, i.e., at reduced atmospheric concentrations, the shock waves are broader, and the transition between expansion core and the background becomes less well defined. Further reduction of the background concentration eliminates any shock waves. Experimental verification of these flow regimes is presented by *Muntz et al.* [1970].

All gas expansions initially are governed by continuum flow. Such flow in a vacuum has been described by *Freeman and Grundy* [1968] and *Freeman and Thomas* [1969]. Continuum flow in a rarified atmosphere has been described by *Holway* [1969], *Brode and Enstrom* [1972], and *Hoffman and Best* [1974].

The transition from self-continuum flow to diffusive flow has been examined by *Linson and Baxter* [1977]. In their treatment, they assume that the gas velocity distribution does not deviate significantly from a Maxwellian distribution. The flow is collision dominated, either by self-collisions or by collisions with the background atmosphere, throughout the expansion. This type of solution is valid in atmospheres denser than those considered in this paper.

In a low-density background, the transition from a self-continuum expansion to a diffusive expansion may be divided into two expansion sequences. The first sequence consists of transition from self-continuum to collisionless flow [*Draper and Hill*, 1969]. The second sequence involves the transition of collisionless flow to diffusive flow. This latter transition has

been modeled by *Brook and Hamel* [1972], and *Baum* [1973, 1974] for interaction with a uniform, chemically nonreactive atmosphere. At high altitudes the self-continuum flow is uncoupled from the diffusive flow by the intervening collisionless expansion.

The work presented here extends the efforts of *Baum* [1973, 1974] to include the effects of a nonuniform background atmosphere and a velocity dependent collision frequency. The unsteady expansion of gas releases is analyzed using gas kinetic theory. The Boltzmann equation with the Krook collision integral is solved numerically. At late times (after many collisions with the background atmosphere) the solution is identical with the one given by diffusion in a nonuniform atmosphere [*Bernhardt*, 1979].

This analysis is motivated by a need for a description of high-altitude releases from rockets or from the Space Shuttle. *Bernhardt* [1976], *Mendillo and Forbes* [1978], and *Anderson and Bernhardt* [1978] have shown that the release into the F layer ionosphere of certain neutral gases (such as CO<sub>2</sub>, H<sub>2</sub>O, and H<sub>2</sub>) will produce plasma depletions, plasma temperature enhancements, and airglow emissions and may trigger instabilities. Proper interpretation of the results from such experiments requires modeling of the flow of the released gas. This is especially true for the supersonic releases made from the Space Shuttle.

This research was also motivated by the observations of *Schunk* [1978] that a simple diffusive model may not adequately describe the flow resulting from gas releases. Specifically, *Schunk* states that the effects of nonlinear acceleration, viscous stress, and velocity-dependent collision frequencies may significantly retard the expansion of the gases at high altitudes. The solution to the Boltzmann's equation incorporates all of these effects.

## 2. ANALYTIC DESCRIPTION

In kinetic theory, the state of a gas is completely described by a distribution function  $f(\mathbf{x}, \mathbf{v}, t)$ , where  $\mathbf{x}$  is the position vector,  $\mathbf{v}$  is the velocity vector, and  $t$  is time. The first three velocity moments of this function give the common physical properties of the gas

$$\int f d^3\mathbf{v} = n(\mathbf{x}, t)$$

$$\int \mathbf{v} f d^3\mathbf{v} = n(\mathbf{x}, t) \mathbf{u}(\mathbf{x}, t)$$

and

$$\int |\mathbf{v}|^2 f d\mathbf{v} = \left[ |\mathbf{u}|^2 + 3 \frac{KT}{m} \right] n(\mathbf{x}, t)$$

where  $n$  is concentration,  $\mathbf{u}$  is bulk velocity, and  $T(\mathbf{x}, t)$  is temperature.

The evolution of the gas distribution function is described by the Boltzmann equation

$$\frac{\partial f}{\partial t} + \mathbf{v} \cdot \nabla_{\mathbf{x}} f + \mathbf{F} \cdot \nabla_{\mathbf{v}} f = (\partial f / \partial t)_c \quad (1)$$

where  $\nabla_{\mathbf{x}}$  and  $\nabla_{\mathbf{v}}$  are the gradient operators in  $\mathbf{x}$  and  $\mathbf{v}$  space, respectively;  $\mathbf{F}$  is an external acceleration vector, and  $(\partial f / \partial t)_c$  is the change in the distribution due to collisions. In this note, the Krook collisional term is used,

$$(\partial f / \partial t)_c = \nu(n\phi - f) \quad (2)$$

where  $\nu(\mathbf{x}, \mathbf{v})$  is the collision frequency,  $\phi$  is the Maxwell distribution given by

$$\phi(\mathbf{v}) = \left( \frac{m}{2\pi kT} \right)^{3/2} \exp \left[ \frac{-m}{2kT} (\mathbf{v} - \mathbf{u})^2 \right] \quad (3)$$

$m$  is the molecular mass, and  $k$  is the Boltzmann constant. The Krook collision term represents relaxation of the distribution function to a Maxwellian distribution characterized by a temperature  $T$  and a velocity  $\mathbf{u}$  [Bhatnagar et al., 1954].

Simulation of gas releases involves two distribution functions:  $f_e$  the released gas (or exhaust) function and  $f_a$  the atmospheric distribution function. The coupled Boltzmann equations describing the interaction between these functions are

$$\begin{aligned} \frac{\partial f_e}{\partial t} + \mathbf{v} \cdot \nabla_{\mathbf{x}} f_e + \mathbf{F} \cdot \nabla_{\mathbf{v}} f_e = \nu_e(n_e \phi_e - f_e) + \nu_{ea}(n_e \phi_a - f_e) \\ + Q_s(t) \phi_s(\mathbf{v}) \delta[\mathbf{x} - \mathbf{S}(t)] \end{aligned} \quad (4)$$

$$\frac{\partial f_a}{\partial t} + \mathbf{v} \cdot \nabla_{\mathbf{x}} f_a + \mathbf{F} \cdot \nabla_{\mathbf{v}} f_a = \nu_a(n_a \phi_a - f_a) + \nu_{ae}(n_e \phi_e - f_a) \quad (5)$$

where the subscripts  $e$  and  $a$  refer to the released gas and to the atmosphere, respectively;  $\nu_{ea}$  and  $\nu_{ae}$  represent collisions between the exhaust and the atmosphere;  $Q_s(t)$  is the source flow rate,  $\phi_s(\mathbf{v})$  is the initial source distribution function; and  $\delta[\mathbf{x} - \mathbf{S}(t)]$  represents a moving point source with position vector  $\mathbf{S}(t) = S_x \hat{\mathbf{a}}_x + S_y \hat{\mathbf{a}}_y + S_z \hat{\mathbf{a}}_z$ . The values used for  $\mathbf{u}$  and  $T$  in the function are indicated by the subscripts  $e$ ,  $a$ , and  $s$  on the distribution function  $\phi$ . The molecular masses used in (4) and (5) are  $m_e$  and  $m_a$ , respectively. The coupling between these equations occurs through the collision frequencies ( $\nu_{ea}$  and  $\nu_{ae}$ ), which are concentration, velocity, and temperature dependent. Production and loss terms can be added to (4) and (5) if chemical reactions are important.

All of the gas flows described in the introduction can be modeled by solution of (4) and (5). For example, if all the collision frequencies are set to zero, collisionless flow occurs. If  $\nu_e \gg \nu_{ea}$ , taking the velocity moments of (4) yields the equations governing self-continuum flow. Similarly, neglecting  $\nu_e$  and finding velocity moments can provide the equations describing diffusive flow.

In this paper, the discussion is limited to the transition from collisionless to diffusive flow. The gas is assumed to have

expanded to the degree that the self-collision frequency ( $\nu_e$ ) is essentially zero. The atmosphere provides a large momentum and energy sink for the released molecules [Baum, 1973]. Also, the high-velocity molecules are primarily moving into undisturbed regions of the atmosphere. Consequently, the background atmosphere is assumed to be in an unperturbed state throughout the expansion. Under these assumptions, (4) is written as

$$\begin{aligned} \frac{\partial f}{\partial t} + \mathbf{v} \cdot \nabla_{\mathbf{x}} f + \mathbf{F} \cdot \nabla_{\mathbf{v}} f = \nu_a(\mathbf{x}, \mathbf{v})(n\phi_a - f) \\ + Q_s(t) \phi_s(\mathbf{v}) \delta[\mathbf{x} - \mathbf{S}(t)] \end{aligned} \quad (6)$$

where the subscript  $e$  has been dropped for convenience. Coordinates  $x$ ,  $y$ , and  $z$  denote the east, north, and vertical directions, respectively. The effects of gravity can be represented by  $\mathbf{F} = -g_0 \hat{\mathbf{a}}_z$ , where  $g_0$  is the gravitational acceleration, and  $\hat{\mathbf{a}}_z$  is the unit vector along the vertical.

The collision frequency must be chosen to represent momentum-transfer collisions between an exhaust particle with velocity  $\mathbf{v}$  and the background atmosphere. The number of collisions per unit time is written as

$$\nu_a(\mathbf{x}, \mathbf{v}) = \frac{m_a}{m_e + m_a} n_a(\mathbf{x}) \sigma_{ea} v_{ea}(\mathbf{v})$$

[Banks and Kockarts, 1973] where  $m_e$  and  $m_a$  are the masses of the exhaust and atmospheric particles, respectively,  $n_a(\mathbf{x})$  is the atmospheric concentration,  $\sigma_{ea}$  is the collision cross section, and  $v_{ea}(\mathbf{v})$  is the average, relative speed between the atmospheric molecules and the exhaust molecule with velocity  $\mathbf{v}$ .

The atmospheric concentration is assumed to vary exponentially with altitude:

$$n_a(z) = n_{a0} \exp[(z_0 - z)/H_a]$$

where  $n_{a0}$  is the concentration at altitude  $z_0$ , and  $H_a = kT_a/m_a g$  is the scale height. The values for temperature  $T_a$  and average molecular mass  $m_a$  are found from the MSIS neutral-atmosphere model described by Hedin et al. [1977a, b]. The altitude dependence should be included if the mean-free path is greater than the scale height of the atmosphere.

The collision cross section is  $\sigma_{ea} = \pi(r_e + r_a)^2$ . The exhaust and atmosphere molecules are taken to be rigid spheres with radii  $r_e$  and  $r_a$ , respectively. With this model, the collision cross section is independent of velocity. The molecular radii for air,  $\text{CO}_2$ , and  $\text{H}_2$  are 0.214, 0.20, and 0.145 nm, respectively [Hirschfelder et al., 1954].

The differential speed between the injected gas molecules and the atmosphere is found by averaging the relative speeds over the atmospheric velocity distribution

$$v_{ea}(\mathbf{v}) = \int_{-\infty}^{\infty} g \phi_a(\mathbf{w}) d^3\mathbf{w}$$

where  $g = |\mathbf{v} - \mathbf{w}|$  is the relative speed between an exhaust molecule with velocity  $\mathbf{v}$  and an atmospheric molecule with velocity  $\mathbf{w}$ . Substitution of the Maxwell distribution given by (3) and integration yield

$$\begin{aligned} v_{ea}(\mathbf{v}) = \frac{c_a}{\pi^{1/2}} \exp \left( - \frac{|\mathbf{v} - \mathbf{u}_a|^2}{c_a^2} \right) \\ + \left( \frac{c_a^2}{2|\mathbf{v} - \mathbf{u}_a|} + |\mathbf{v} - \mathbf{u}_a| \right) \text{erf} \left( \frac{|\mathbf{v} - \mathbf{u}_a|}{c_a} \right) \end{aligned} \quad (7)$$

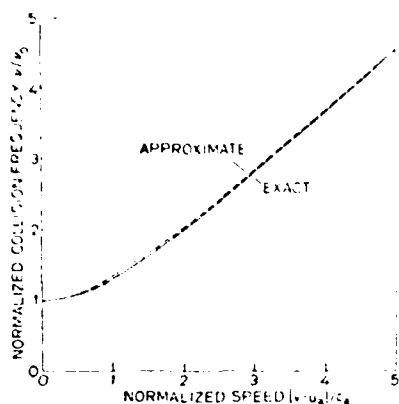


Fig. 1. Increase in the molecular collision frequency with speed. The exact expression involves exponentials and error functions. The approximate formula, which only requires the computation of a square root, is used in the modeling.

where  $c_a = (2kT_a/m_a)^{1/2}$  is the atmospheric speed of sound and  $|v - u_a|$  is the relative speed between the exhaust particle and the atmosphere [Muckenfuss, 1962]. For  $|v - u_a|/c_a \ll 1$ , the relative speed becomes

$$v_{ra} = \frac{2}{\pi^{1/2}} c_a = (8kT_a/\pi m_a)^{1/2}$$

Thus at low speed the average relative speed (and also the collision frequency) is independent of exhaust velocity. If  $|v - u_a|/c_a \gg 1$ , the average relative speed becomes  $v_{ra}(v) = |v - u_a|$ . At high speeds the thermal motion of the atmosphere has little effect on the average relative velocity.

Equation (7) may be approximated by a hyperbola to simplify numerical calculation

$$v_{ra}(v) \approx \left( \frac{4c_a^2}{\pi} + |v - u_a|^2 \right)^{1/2}$$

The maximum error caused by this hyperbolic approximation is less than 3%. The expression for collision frequency becomes

$$\begin{aligned} \nu_a(x, v) &= \frac{m_a}{m_r + m_a} n_{a0} \exp\left(\frac{z_0 - z}{H_a}\right) \\ &\cdot \sigma_{ra} \left( \frac{4c_a^2}{\pi} + |v - u_a|^2 \right)^{1/2} \\ &= \nu_0 \exp\left(\frac{z_0 - z}{H_a}\right) \left( 1 + \frac{|v - u_a|^2 \pi}{4c_a^2} \right) \end{aligned} \quad (8)$$

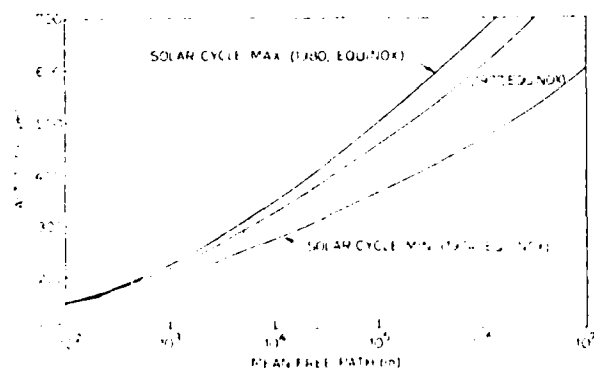


Fig. 2. Altitude and solar cycle dependence of the mean free path for  $\text{CO}_2$  in the atmosphere.

where  $\nu_0 = (2c_a m_a n_{a0} \sigma_{ra}) / [\pi^{1/2} (m_r + m_a)]$ . The exact and approximate computations for the velocity dependence of the collision frequency are compared in Figure 1. The rapid increase in the collision frequency for velocities greater than the speed of sound is illustrated.

Another parameter of interest is the mean free path of each exhaust particle as defined by

$$\lambda(x, v) = |v - u_a| / \nu_a(x, v)$$

For low-speed particles,

$$\lambda(x, v) = \frac{|v - u_a| (m_r + m_a) \pi^{1/2}}{m_a n_a(x) \sigma_{ra} 2c_a}$$

which vanishes at  $|v - u_a| \rightarrow 0$ . For high-speed (supersonic) particles, the mean free path takes the limiting value

$$\lambda(x, v) \rightarrow \frac{m_r + m_a}{m_a n_a(x) \sigma_{ra}}$$

Representative profiles of the high-speed values of mean free path for  $\text{CO}_2$  are shown as a function of solar cycles in Figure 2. These profiles are based on the MSIS model atmosphere. A strong altitude and solar cycle dependence is evident.

The formulation represented by (6) is only valid in low-density regions where the released gas will attain a collisionless state before the flow is dominated by diffusion. The regions, which permit collisionless flow, are found by comparing the equal-mass radius of the released gas to the atmospheric mean free path [e.g., Baxter and Linson, 1977; Linson and Baxter, 1977]. The equal-mass radius is the characteristic length of the cloud when it has expanded to a volume which contains an amount of atmospheric mass equal to the mass of the released gas. This radius is given by

$$a_0 = \left( \frac{3m_r Q_0}{4\pi n_a m_a} \right)^{1/3}$$

where  $Q_0$  is the number of exhaust molecules released and  $n_a$  is the atmospheric concentration.

If this length is less than 3 mean free paths, the released gas will expand in a collisionless state for at least 1.5 mean collision times before significant interaction with the background atmosphere occurs. Consequently, (6) can be applied if  $a_0/\lambda < 3$ . This criterion is illustrated in Figure 3 for a  $\text{CO}_2$  injection into the MSIS model atmosphere during equinox, 1977.

The procedures described in this paper may be applied for conditions of release above and to the left of the curve in Figure 3. Releases corresponding to conditions below the

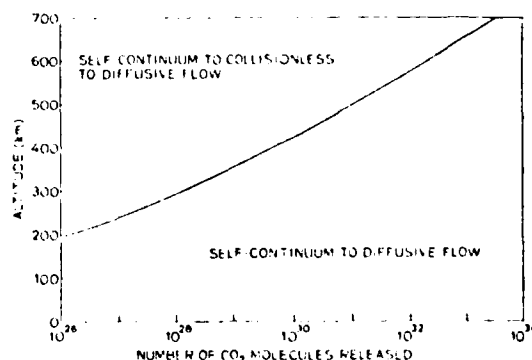


Fig. 3. Conditions where different expansion concepts apply. The theory presented in the text is applicable to releases for conditions to the left of and above the solid curve.

curve should use the continuum flow equations such as described by *Baxter and Linson* [1977]. The validity of the criteria described above is only approximate. Changes in the initial velocity and shape of the injected gas affect these criteria.

### 3. METHOD OF SOLUTION

Equation (6) is a partial differential equation in seven variables:  $x$ ,  $y$ ,  $z$ ,  $v_x$ ,  $v_y$ ,  $v_z$ , and  $t$ . An analytical solution for a stationary source [ $S(t) = 0$ ] in a uniform atmosphere ( $v_a = \text{const}$ ) has been found by *Baum* [1973, 1974]. This analytic solution involves a three-dimensional convolution in space as well as an integration over time. Baum's solution is not readily extendable to the analysis of releases from a moving source in a nonuniform atmosphere with a velocity-dependent collision frequency.

If the flow were nearly Maxwellian, velocity moment equations could be used to describe the solution. Collisionless flow, however, is highly non-Maxwellian, and truncation to a finite set of velocity moment equations would introduce large errors in the results. For this reason, a numerical solution to (6) is formulated.

By transformation of variables and integration over velocity space, (6) is converted into an integral equation suitable for a recursive, numerical solution. Using the transformations

$$\mathbf{x}' = \mathbf{x} - \mathbf{v}t + \frac{\mathbf{F}t^2}{2}$$

and

$$\mathbf{v}' = \mathbf{v} - \mathbf{F}t$$

Equation (6) becomes

$$\frac{\partial f}{\partial t} = v_a(\mathbf{p}, \mathbf{q})[v_a(\mathbf{p}, t)\phi_a(\mathbf{q}) - f] + Q_s(t)\phi_s(\mathbf{p})\delta[\mathbf{p} - \mathbf{S}(t)] \quad (9)$$

where

$$\mathbf{p}(t) = \mathbf{x} + \mathbf{v}'t + \mathbf{F}t^2/2$$

$$\mathbf{q}(t) = \mathbf{v}' + \mathbf{F}t$$

With the substitution

$$f = g \exp \left\{ - \int_0^t v_a[\mathbf{p}(t_1), \mathbf{q}(t_1)] dt_1 \right\}$$

Equation (9) becomes

$$\frac{\partial g}{\partial t} = G_1(\mathbf{x}', \mathbf{v}', t)Q_s(t)\phi_s(\mathbf{q})\delta[\mathbf{p} - \mathbf{S}(t)] + G_1(\mathbf{x}', \mathbf{v}', t)v_a(\mathbf{p}, \mathbf{q})v_a(\mathbf{p}, t)\phi_a(\mathbf{q}) \quad (10)$$

where

$$G_1(\mathbf{x}', \mathbf{v}', t) = \exp \left\{ \int_0^t v_a[\mathbf{p}(t_1), \mathbf{q}(t_1)] dt_1 \right\}$$

Integrating with respect to  $t$  and making substitutions for  $\mathbf{x}'$ ,  $\mathbf{v}'$ , and  $g$  yield

$$\begin{aligned} \psi(\mathbf{x}, \mathbf{v}, t) = & \int_0^t G_2(\mathbf{x}, \mathbf{v}, t_1)Q_s(t-t_1)\delta(\mathbf{v} - \mathbf{F}t_1) \\ & \cdot \delta \left[ \mathbf{x} - \mathbf{v}t_1 + \frac{\mathbf{F}t_1^2}{2} - \mathbf{S}(t-t_1) \right] dt_1 \\ & + \int_0^t G_2(\mathbf{x}, \mathbf{v}, t_1)v_a \left( \mathbf{x} - \mathbf{v}t_1 + \frac{\mathbf{F}t_1^2}{2}, \mathbf{v} - \mathbf{F}t_1 \right) \end{aligned}$$

$$\cdot n \left( \mathbf{x} - \mathbf{v}t_1 + \frac{\mathbf{F}t_1^2}{2}, t-t_1 \right) \phi_a(\mathbf{v} - \mathbf{F}t_1) dt_1 \quad (11)$$

where

$$G_2(\mathbf{x}, \mathbf{v}, t_1) = \exp \left[ - \int_0^{t_1} v_a \left( \mathbf{x} - \mathbf{v}t_2 + \frac{\mathbf{F}t_2^2}{2}, \mathbf{v} - \mathbf{F}t_2 \right) dt_2 \right]$$

$$f(\mathbf{x}, \mathbf{v}, t) = 0 \quad t < 0$$

The distribution function given by (11) is multiplied by 1,  $\mathbf{v}$ , and  $|\mathbf{v}|^2$  and integrated over velocity space to yield concentration, bulk velocity, and temperature, respectively. The result is written compactly as

$$\begin{aligned} n(\mathbf{x}, t) & \left[ \frac{1}{|\mathbf{u}|^2 + 3kT(\mathbf{x}, t)/m_e} \right] \\ & = \int_0^t G_3(\mathbf{x}, \mathbf{S}(t-t_1), t_1) \frac{Q_s(t-t_1)}{t_1^3} \phi_s[\mathbf{U}(t_1)] \left[ \frac{1}{|\mathbf{U}(t_1)|^2} \right] d\mathbf{U} \\ & + \int_0^t \int_{-\infty}^{\infty} G_3(\mathbf{x}, \mathbf{x}', t_1)v_a[\mathbf{x}', \mathbf{V}(t_1)] \\ & \cdot \frac{n(\mathbf{x}', t-t_1)}{t_1^3} \phi_a[\mathbf{V}(t_1)] \left[ \frac{1}{|\mathbf{V}(t_1)|^2} \right] d^3\mathbf{x}' dt_1 \quad (12) \end{aligned}$$

where

$$\mathbf{U}(t_1) = [\mathbf{x} - \mathbf{S}(t-t_1)]/t_1 - \mathbf{F}t_1/2$$

$$\mathbf{V}(t_1) = (\mathbf{x} - \mathbf{x}')/t_1 - \mathbf{F}t_1/2$$

$$\mathbf{x}' = \mathbf{x} - \mathbf{v}t_1 + \mathbf{F}t_1^2/2$$

$$G_3(\mathbf{x}, \mathbf{S}, t_1) = G_2(\mathbf{x}, (\mathbf{x} - \mathbf{S})/t_1 + \mathbf{F}t_1/2, t_1)$$

The first equation in (12) is a Fredholm-Volterra equation of the second kind. There exist a variety of methods for its solution [e.g., *Baker*, 1977]. Quadrature techniques are chosen for simplicity. The first term on the right side of (12) is evaluated using Gaussian quadrature. This is the dominant term for time less than  $1/\nu$ . Early time solutions are introduced into the second term on the right side of (12). The solution then proceeds recursively. After the concentration  $n(\mathbf{x}, t)$  is found, the velocity and temperature are found directly from the second and third equations in (12).

In certain cases, the integral representation of  $G_3$  may be computed analytically. If the external acceleration term (i.e., gravity) is dropped,  $G_3$  becomes

$$G_3(\mathbf{x}, \mathbf{S}, t_1) = \exp \left[ -v_a \left( \mathbf{S}, \frac{\mathbf{x} - \mathbf{S}}{t_1} \right) t_1 F(z, S_z) \right] \quad (13)$$

where

$$F(z, S_z) = \frac{\exp[(z - S_z)/H_0] - 1}{(z - S_z)/H_0}$$

If both external forces and atmospheric gradients are neglected,  $F(z, S_z) = 1$ .

In the following discussions,  $\mathbf{F}$  is set to zero. This is justified because gravity is negligible for the short times considered in the examples. Also, releases at orbital velocity do not see the effects of gravity in a flat earth geometry. A more detailed analysis may have to include the effects of a curved (versus flat) earth as well as gravity.

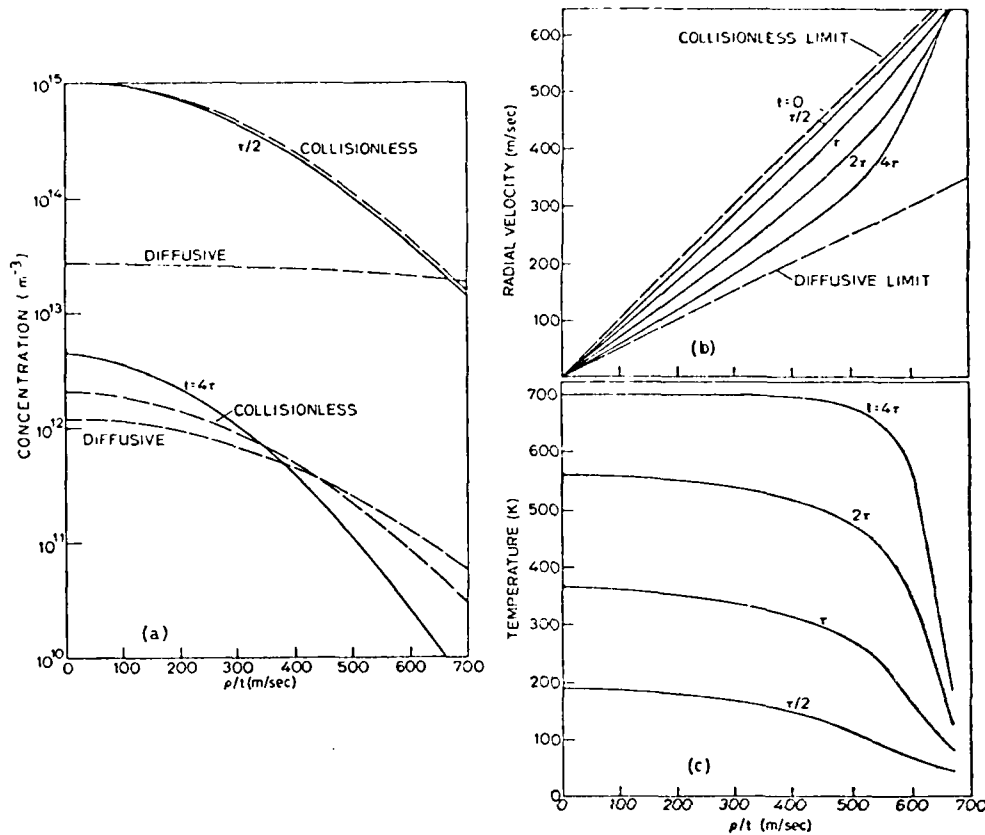


Fig. 4. Simulation of a low-temperature (300 K) spherical expansion of  $\text{CO}_2$ . The concentration and temperature of the background gas are  $1 \times 10^{14} \text{ m}^{-3}$  and 870 K, respectively. The low-speed atmospheric collision frequency ( $\tau$ ) is 70.8 s. At early times ( $t < \tau$ ), the expansion is nearly collisionless. At later times, the concentration, velocity, and temperature relax to their collision-dominated limits.

#### 4. PHYSICAL INTERPRETATION

The released gas concentration given by (12) can be written as

$$n(\mathbf{x}, t) = n_0(\mathbf{x}, t) + n_1(\mathbf{x}, t) \quad (14)$$

The first term,  $n_0(\mathbf{x}, t)$ , denotes the part of the solution which is in a collisionless state. Written out in full, this term is

$$n_0(\mathbf{x}, t) = \int_0^t G_3(\mathbf{x}, \mathbf{S}(t-t_1), t_1) \cdot \frac{Q_0(t-t_1)}{t_1^3} \phi_s \left[ \frac{\mathbf{x} - \mathbf{S}(t-t_1)}{t_1} \right] dt_1 \quad (15)$$

where  $F$  is set to zero.

This is the only remaining term for a vanishing collision frequency. The function  $G_3$  (see (12) and (13)) represents damping of the collisionless expansion by interaction with the background atmosphere. The function  $n_0(\mathbf{x}, t)$  is excited only by the initial-gas source distribution function and is called the natural response.

The second term in (14) is the part of the solution governed by the background environment.

$$n_1(\mathbf{x}, t) = \int_0^t \int G_3(\mathbf{x}, \mathbf{r}, t_1) n_0 \left( \mathbf{r}, \frac{\mathbf{x} - \mathbf{r}}{t_1}, t_1 \right) \frac{n(\mathbf{r}, t-t_1)}{t_1^3} \phi_s \left( \frac{\mathbf{x} - \mathbf{r}}{t_1} \right) d\mathbf{r} dt_1 \quad (16)$$

This function is a convolution of the previous gas concentration with a function of the background atmosphere. It is the only term remaining after many collision times. The function  $n_1(\mathbf{x}, t)$  asymptotically approaches the diffusion solution for long times [Baum, 1973] and is called the forced response to the gas injection. In this example, the forcing function is the particle distribution of the background atmosphere.

#### 5. GAS SOURCE REPRESENTATION

Both point sources and line sources of released gases are of interest. The release of gas vapors from explosively detonated canisters is an example of a point source release. The line source can be represented by exhaust released from a rocket or from the Space Shuttle. Only these sources will be considered here.

The initial velocity of molecules released from any source is the sum of the source velocity vector plus the initial velocity vector of the molecules relative to the source:

$$\mathbf{u}_s = \mathbf{v}_s + \mathbf{w}_s \quad (17)$$

where  $\mathbf{u}_s$  is the bulk velocity relative to a point in space,  $\mathbf{v}_s$  is the source velocity relative to a point in space, and  $\mathbf{w}_s$  is the bulk velocity relative to the source.

A point source is specified by the function  $Q_s(t) = Q_0 \delta(t)$  where  $Q_0$  is the number of molecules released. The position vector  $\mathbf{S}_0$ , velocity vectors  $\mathbf{u}_s$ ,  $\mathbf{v}_s$ , and  $\mathbf{w}_s$ , and temperature  $T_s$

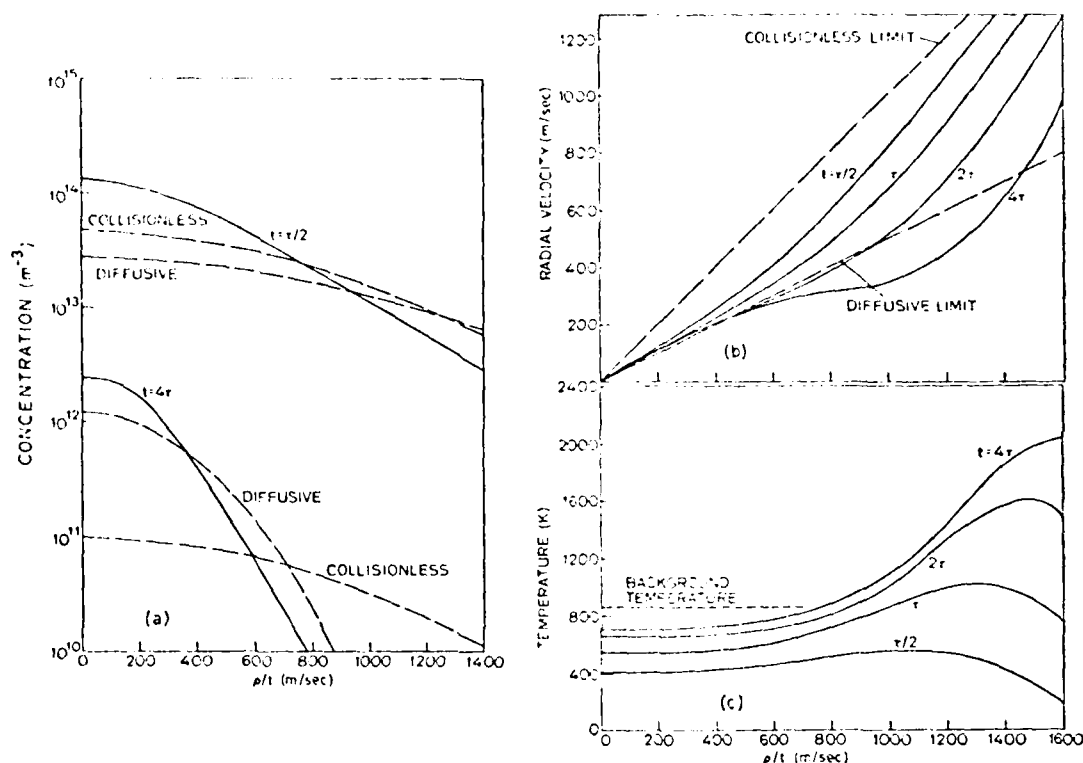


Fig. 5. Simulation of a high-temperature (2400 K) spherical expansion of CO<sub>2</sub>. The background gas is identical to the one for Figure 4 ( $\tau = 70.8$  s). The large initial temperature at the time of release produces a rapid expansion. At the edge of the expansion, the velocity is retarded and the temperature is elevated above the ambient temperature.

complete the description of the source. Substitution of these quantities into (15) yields

$$n_0(\mathbf{x}, t) = G_3(\mathbf{x}, \mathbf{S}_0, t) \frac{Q_0}{P} \phi_s \left[ \frac{\mathbf{x} - \mathbf{S}_0}{t} \right] \quad (18)$$

where  $G_3$  and  $\phi_s$  have been previously defined in (3) and (12), respectively.

The line source is assumed to be moving at a constant velocity and to be releasing molecules at a constant rate. The position of the source is given by

$$\mathbf{S}(t) = \mathbf{v}_s t + \mathbf{S}_0$$

where  $\mathbf{S}_0$  is the location of the start of the release at time  $t = 0$ . The molecules are assumed to be released at a rate of  $Q_0$  molecules per second. The duration of the release is  $t_0$  s. The velocity and temperature of the molecules leaving the source

are  $\mathbf{w}_s$  and  $T_s$ , respectively. Using (15), the natural term in the solution of the Boltzmann equation is

$$n_0(\mathbf{x}, t) \approx \int_{\max(0, t-t_0)}^t G_3(\mathbf{x}, \mathbf{v}_s(t-t_1) + \mathbf{S}_0, t_1) \frac{Q_0}{t_1^3} \phi_s \left[ \frac{\mathbf{x} - \mathbf{S}_0}{t_1} + \mathbf{v}_s(t-t_1/t_1) \right] dt_1 \quad (19)$$

## 6. SPHERICAL EXPANSION

It is instructive to consider the flow resulting from the point release of vapor into a uniform atmosphere. The results for the spherical expansion can be compared with analytic solutions for collisionless and diffusive expansions. The concentration, radial velocity, and temperature for the collisionless expansion from a point release are given by

TABLE 1. Simulated Vapor Flows

Simulation	Species	Release Quantity	Source	Initial Velocity, km/s	Background Atmosphere	Figure
I	CO <sub>2</sub>	$1 \times 10^6$ (730 kg)	point	$\mathbf{v}_s = 0$	solar max	6
II	CO <sub>2</sub>	$1 \times 10^6$ (730 kg)	point	$\mathbf{v}_s = \mathbf{v}_{\text{avg}} = 0$	solar avg	7
III	CO <sub>2</sub>	$1 \times 10^6$ (730 kg)	point	$\mathbf{v}_s = -10$ $\mathbf{v}_{\text{avg}} = 7.7$ $\mathbf{v}_{\text{max}} = 0$ $\mathbf{v}_{\text{min}} = -3.1$	solar max	8
IV	CO <sub>2</sub>	$1 \times 10^6$ (730 kg)	line $t_0 = 10$ s	$\mathbf{v}_s = 7.7$ $\mathbf{v}_{\text{avg}} = 0$ $\mathbf{v}_{\text{max}} = 7.7$ $\mathbf{v}_{\text{min}} = -3.1$	solar max	9
V	H <sub>2</sub>	$1 \times 10^6$ (33 kg)	line $t_0 = 10$ s	$\mathbf{v}_s = 7.7$ $\mathbf{v}_{\text{avg}} = 0$ $\mathbf{v}_{\text{max}} = 7.7$ $\mathbf{v}_{\text{min}} = -3.1$	solar max	10

TABLE 2. Model Atmosphere at 400-km Altitude

	$F_{10.7}$ Solar Flux*	Neutral Concentration	Neutral Molecular Temperature, K	Average Molecular Mass, amu
Solar minimum (1974 equinox)	70	$3.24 \times 10^{13} \text{ m}^{-3}$	746	15.1
Solar average (1977 equinox)	160	$1.85 \times 10^{14} \text{ m}^{-3}$	990	15.9
Solar maximum (1980 equinox)	225	$2.95 \times 10^{14} \text{ m}^{-3}$	1192	17.1

\*Flux unit =  $10^{-22} \text{ W m}^{-2} \text{ Hz}^{-1}$ .

$$n_{cl}(\rho, t) = \frac{Q_0}{\rho^2} \phi_s(\rho/t) \quad u_{cl}(\rho, t) = \rho/t \quad T_{cl} = 0$$

where  $\rho$  is the radial distance from the center of the release and  $t$  is the time after release. The corresponding quantities for diffusive flow are

$$n_{df}(\rho, t) = Q_0 \exp[-\rho^2/(4D_0t)]/(4\pi D_0t)^{3/2}$$

$$u_{df}(\rho, t) = \rho/2t \quad T_{df} = T_a$$

where  $D_0 = kT_a/m_0v_a$  is the diffusion coefficient.

The following examples illustrate radial profiles in concentration, velocity, and temperature for  $1 \times 10^{25}$  molecules re-

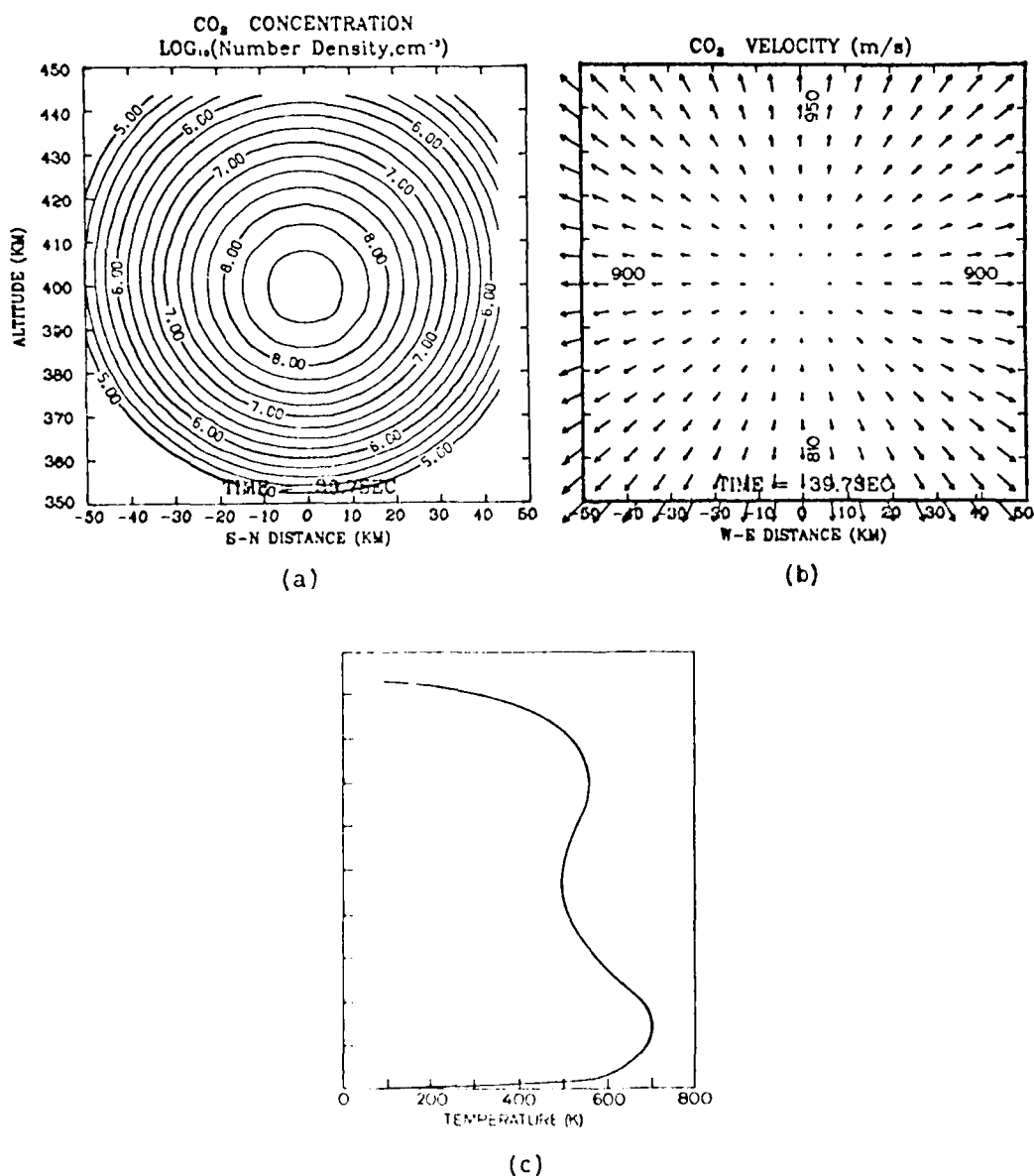


FIG. 4. Simulation of a medium temperature (920 K) expansion of CO<sub>2</sub> in a nonuniform atmosphere. Collisions in the dense, lower-altitude regions retard the flow in comparison with the expansion at higher altitudes. The high temperatures at lower altitudes show the effects of collisional heating.



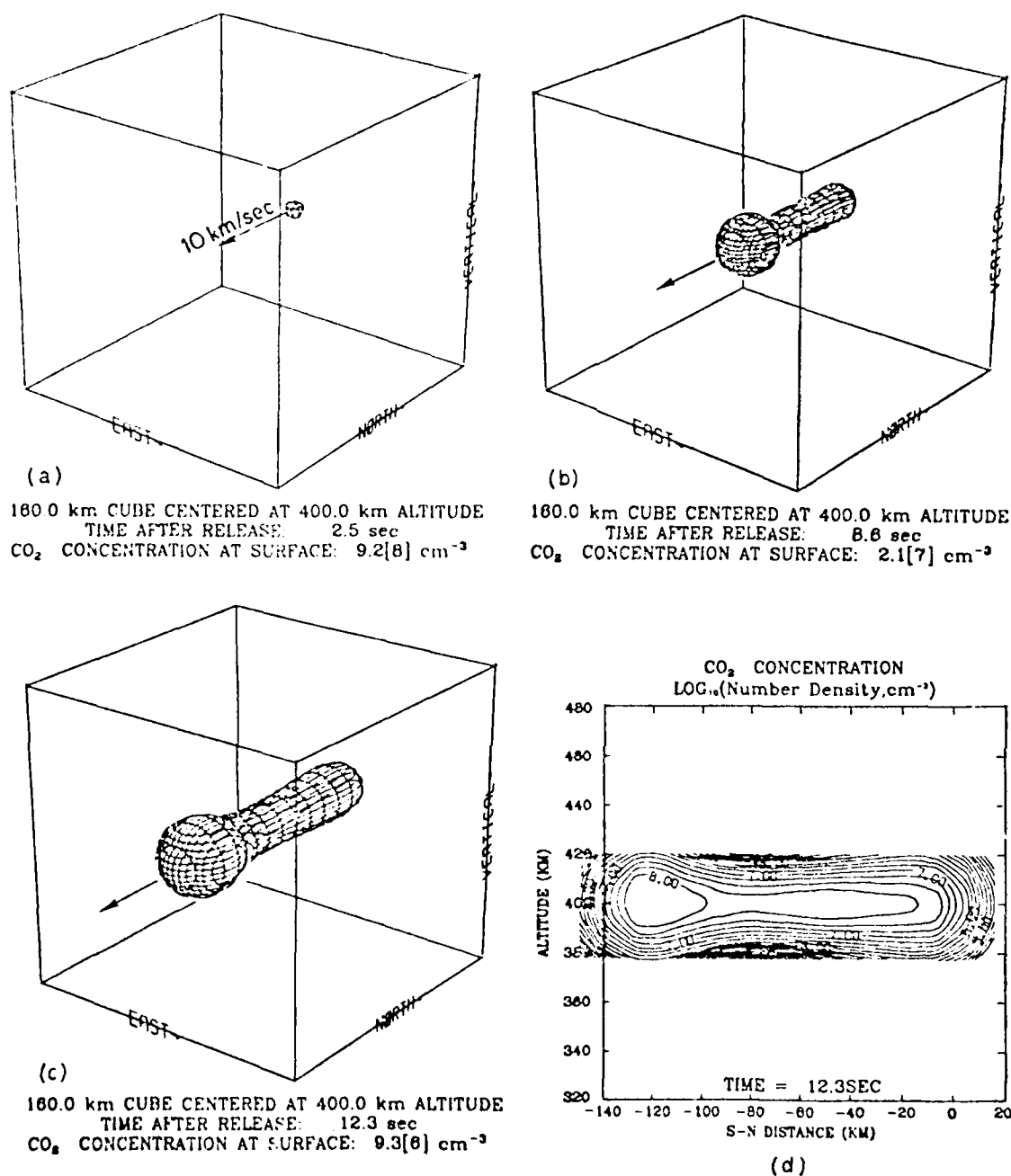


Fig. 7. Formation of a cometlike tail on a high-velocity point release, moving horizontally. Scattering of the injected molecules cause the elongation of the originally spherical vapor cloud.

leased into a uniform atmosphere with a concentration of  $1 \times 10^{10} \text{ m}^{-3}$ , a temperature of 860 K, and an average molecular mass of 15.2 amu. The mean collision time ( $\tau$ ) for this atmosphere is 70.8 s. In all figures, the radial dimension ( $\rho$ ) is divided by the time after release ( $t$ ) for display convenience.

Figure 4 presents the results for a point source of  $\text{CO}_2$  with a low initial temperature of 300 K. At time  $\tau/2$ , the flow is nearly collisionless. The concentration, radial velocity, and temperature are close to their collisionless limits. At time  $4\tau$ , the velocity profile is approaching its diffusive limit of  $\rho/t$ , and the gas temperature has been elevated to 700 K approaching the background temperature of 860 K.

A high-temperature (2400 K) release produces a much more rapid expansion (Figure 5). At  $\tau/2$  the gas is in a transition between collisionless and diffusive flow. At  $4\tau$ , the core of the vapor is in a diffusive state. The outer boundary of the gas ball, however, has a radial velocity below the diffusive limit (Figure 5b) and a temperature higher than the background temperature (Figure 5c). These effects on the surface of the expanding sphere represent dissipation of the initial expansion energy of the gas.

These two examples of gas expansion provide a check on the simulation. Both the low- and high-speed flows are initially collisionless, relaxing to nearly diffusive flow after many colli-

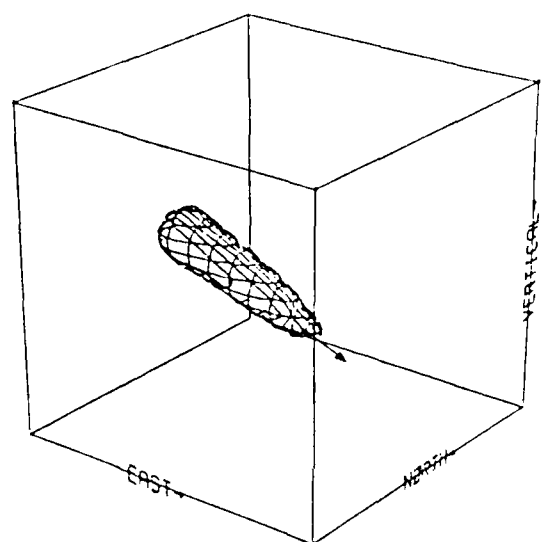
sion times. The calculated flows in both cases are retarded when compared with purely diffusive expansions. This retardation has been explained in terms of nonlinear acceleration, viscous stress, and velocity dependent collision frequency by Schunk [1978], all of which are built into the present model.

### 7. ANISOTROPIC EXPANSIONS

In this section, five vapor releases are presented, illustrating the effects of a nonuniform atmosphere, of a large initial velocity, and of variations in the released species. The condi-

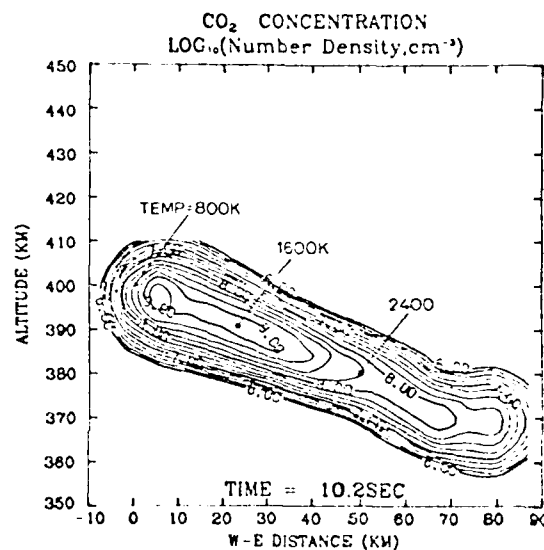
tions for the five releases are listed in Table 1. The source temperature is 920 K in all cases. All of the releases take place at 400-km altitude in the model atmospheres given in Table 2. The atmospheric wind is assumed to be negligible in comparison with the supersonic velocities of the expansions.

The first example is a point release of  $\text{CO}_2$  vapor. The gas center of mass is initially at rest. Because of the nonuniform atmosphere, the expansions are different from the ones presented in the previous section. The density, velocity, and temperature of the vapor 2  $\tau$ s after release are illustrated in Figure

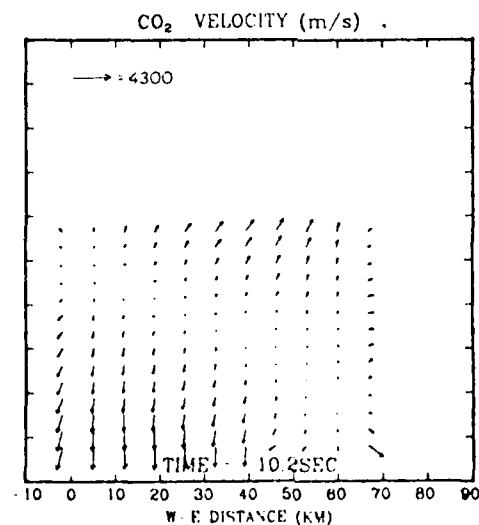


100.0 km CUBE CENTERED AT 400.0 km ALTITUDE  
TIME AFTER RELEASE: 10.2 sec  
 $\text{CO}_2$  CONCENTRATION AT SURFACE:  $1.4[8] \text{ cm}^{-3}$

(a)

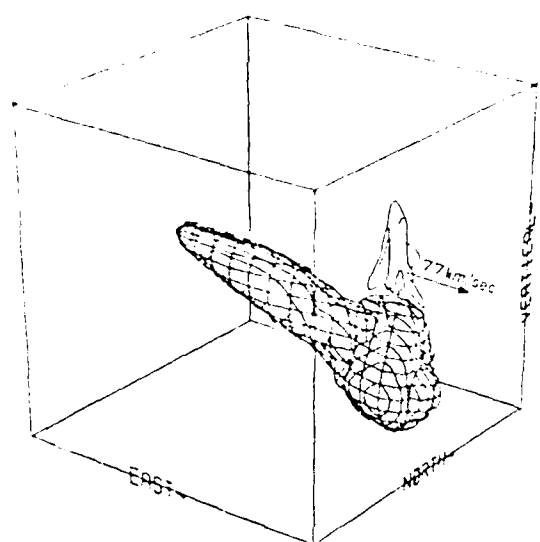


(b)



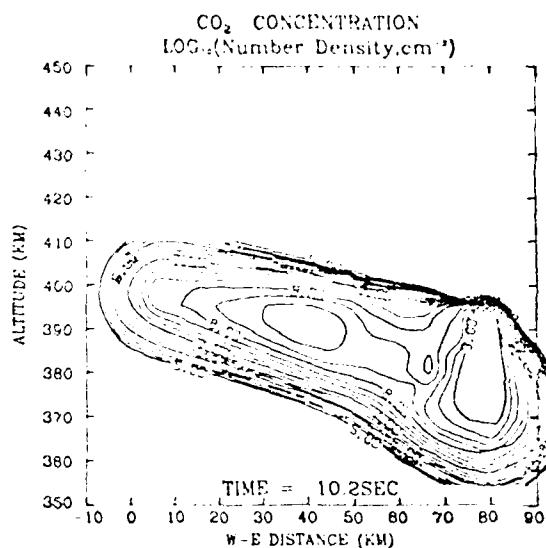
(c)

Fig. 8. Injection of  $\text{CO}_2$  with a velocity of  $8.3 \text{ km/s}$  at an elevation of  $\sim 22^\circ$ . The vapor is rapidly stopped due to collisions in the lower atmosphere.

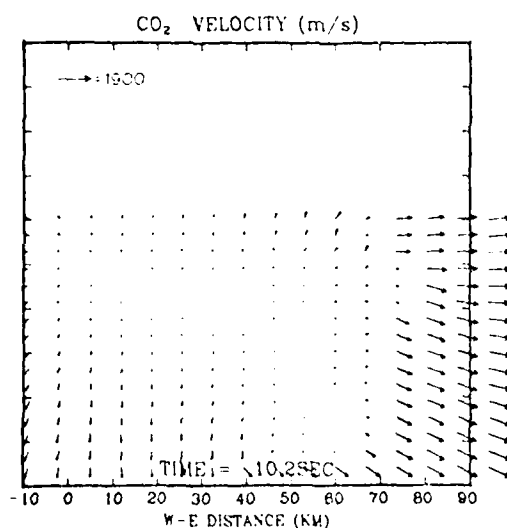


100.0 km CUBE CENTERED AT 400.0 km ALTITUDE  
 TIME AFTER RELEASE: 10.2 sec  
 $\text{CO}_2$  CONCENTRATION AT SURFACE:  $4.9[7] \text{ cm}^{-3}$

(a)



(b)



(c)

Fig. 9.  $\text{CO}_2$  exhaust trail produced by the Space Shuttle moving at  $7.7 \text{ km/s}$ , firing its engines downward with an exhaust velocity of  $3.1 \text{ km/s}$ . The engines burn for  $10 \text{ s}$  releasing  $10^{23}$  molecules per second.

6. (At the point of release, the mean collision time is  $\tau = 19.8 \text{ s}$ .) The expansion is slightly nonspherical, as indicated by the larger distance between contour lines above than below the release point (Figure 6a). At a given distance from the release point, the expansion speed increases with altitude (Figure 6b). The vertical temperature profile through the center of the release (Figure 6c) shows greater collisional heating below the release point because of the denser atmosphere at low altitudes. Except for the small anisotropy introduced by the non-linear atmosphere, the expansion is qualitatively the same as shown in section 6.

The second example illustrates the elongation of a point source when it is released horizontally at Mach 11 into the

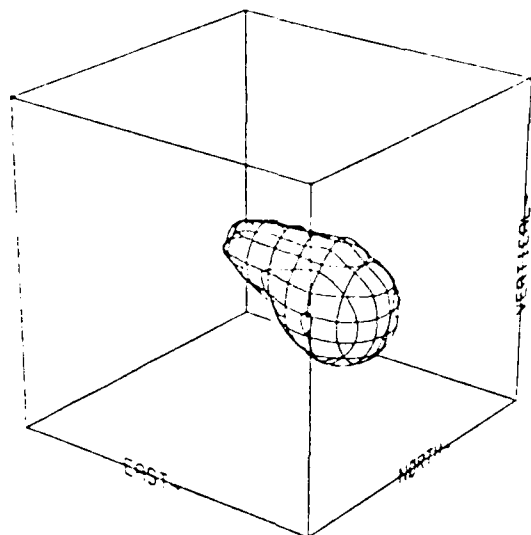
atmosphere during a period of average solar activity. The injection velocity is directed southward. Successive time frames of the gas expansion are shown in Figure 7. Collisions with the background gas molecules cause a comelike tail to form on the cloud. After  $12.3 \text{ s}$  the vapor trail extends over  $100\text{-km}$  distance (Figure 7d), and the bulk of the vapor is still in a collisionless state.

If the vapor is injected with a downward velocity component, it will be expected to be rapidly stopped as it encounters the dense, low-altitude atmosphere. The third example illustrates a release from the Space Shuttle orbiting at  $400\text{-km}$  altitude with an eastward velocity of  $7.7 \text{ km/s}$ . The vapor is ejected from the Shuttle with a downward velocity of  $3.1 \text{ km/s}$

into the atmosphere at solar maximum. Within 10 s, the bulk of the vapor becomes collisionally thermalized within 40 km of the release point (Figures 8a and 8b). The expansion velocity is large only at the edges of the vapor cloud (Figure 8c). The temperature of the gas down stream from the release point increases due to molecular collisions (Figure 8b). The vapor is in a nearly diffusive state. Further expansion can be modeled using a diffusive model [Bernhardt, 1979].

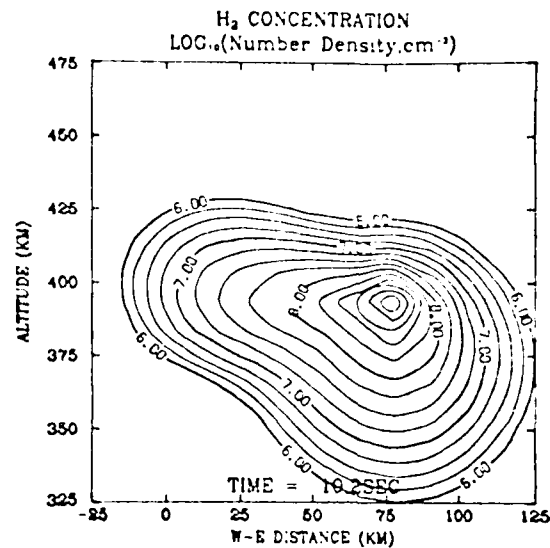
Up to this point, all of the examples have dealt with point releases such as may be produced by explosive canisters. It may be more practical to release vapors in the form of gas jets. The fourth example illustrates the vapor flow of the  $\text{CO}_2$

exhaust released from the engines of the orbiting Shuttle. The vehicle is moving eastward at 7.7 km/s. The Shuttle engines are oriented downward, ejecting  $\text{CO}_2$  with a velocity of 3.1 km/s at a rate of  $10^{23}$  molecules/s. (This is a factor of 5 greater than the actual capabilities of the orbiter engines.) The engines are firing for 10 s, yielding a total release of  $10^{24}$  molecules. This example differs from the previous example only because a line source instead of a point source is used. The continuous source produces the flow pattern shown in Figure 9 at a time 10.2 s after the start of the burn (0.2 s after the Shuttle engines are turned off). Most of the vapor is in the free-streaming plume 78 km to the east of the start of the burn (Figure 9b).

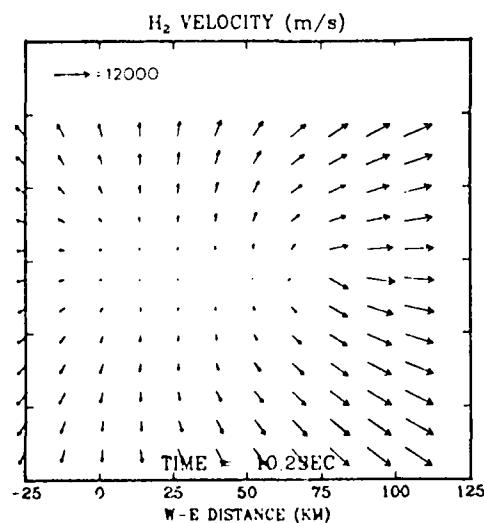


1500 km CUBE CENTERED AT 400.0 km ALTITUDE  
TIME AFTER RELEASE: 10.2 sec  
 $\text{H}_2$  CONCENTRATION AT SURFACE:  $3.2[7] \text{ cm}^{-3}$

(a)



(b)



(c)

Fig. 10.  $\text{H}_2$  exhaust trail produced by the Space Shuttle with the same orientation as in Figure 9. The low mass of the  $\text{H}_2$  molecule makes this flow substantially different from the  $\text{CO}_2$  flow in the previous figure.

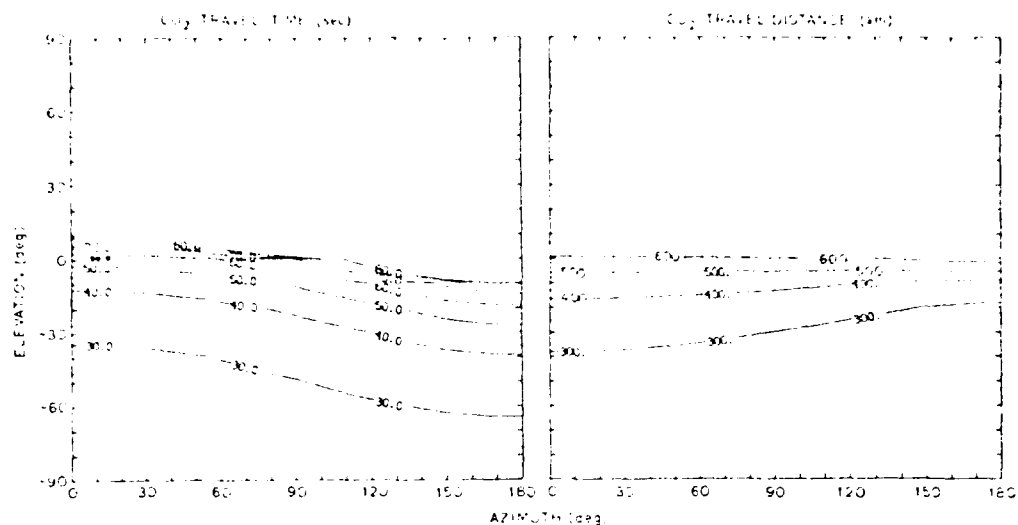


Fig. 11. Travel time and distance for releases of  $\text{CO}_2$  at 400-km altitude during solar minimum. Azimuths of  $0^\circ$  and  $180^\circ$  are along and against the orbit velocity, respectively. Releases with a positive elevation angle are not collisionally stopped in less than a time of (6) s or a distance of (60) km.

The free-streaming vapor is moving at a high velocity (Figure 9c) and will travel for many tens of kilometers before being collisionally stopped. When the vapor enters a diffusive state, its length will be double that shown in the figure.

If the vapors are released from rocket engines, it is unlikely that only one species will be released. The Space Shuttle engines, for instance, release substantial quantities of  $\text{CO}_2$ ,  $\text{N}_2$ ,  $\text{H}_2\text{O}$ , and  $\text{H}_2$ . The fifth example deals with  $\text{H}_2$  vapor expansion. This simulation is identical with the fourth simulation except that the values of molecular mass and collisional cross section for  $\text{H}_2$  instead of  $\text{CO}_2$  are used. The concentration and velocity for this release are illustrated in Figure 10. Note that the scale in Figure 10 is 1.5 times the scale in Figure 9.

All of the examples dealt with the release of  $10^{24}$  molecules. To find the results for the release of different quantities of vapor, scale the concentrations according to the amount released. This procedure is valid as long as the release quantity does not violate the criteria established by Figure 3 in section 2.

#### 8. TRAVEL DISTANCE FOR SUPERSONIC RELEASES

As demonstrated in the previous section, supersonic vapors may come to rest a considerable distance from their point of release. In this section, the travel distance for the bulk of the released vapor is calculated for a variety of injection conditions.

A molecule is said to be collisionally halted when it loses a large fraction (say, 90%) of its original momentum due to molecular collisions. From section 2, the mean free path for supersonic molecules is independent of velocity but does depend on the concentration of the background atmosphere. Thus the condition for the loss of 90% of the momentum of a supersonic molecule is approximated by

$$\exp \left[ - \int \lambda ds \right] \approx 0.1$$

where  $\lambda$  is the spatially dependent collision frequency and  $\int \lambda ds$  is the integral along a molecular path. In a uniform atmo-

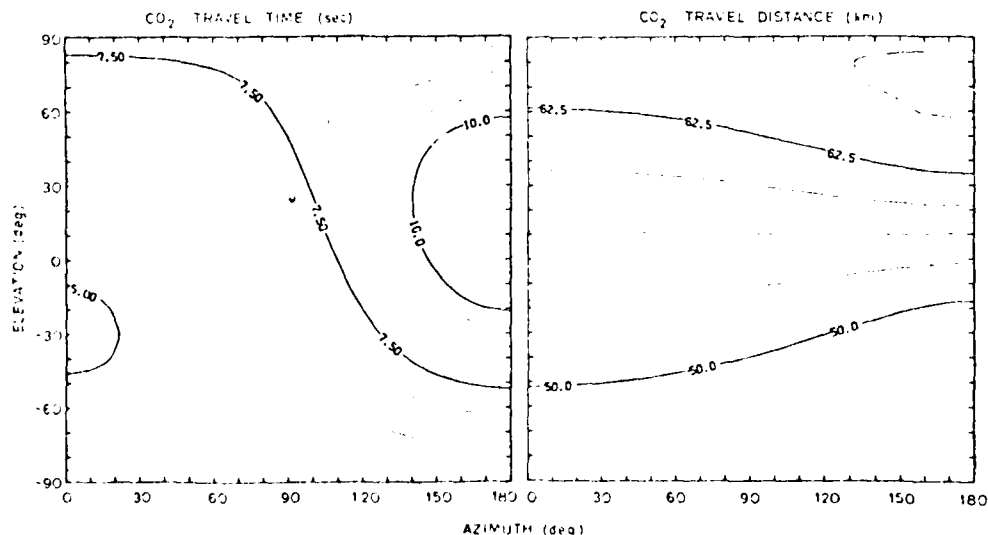


Fig. 12.  $\text{CO}_2$  travel time and distance for releases at 400-km altitude into the solar maximum atmosphere. Except for the atmosphere, the conditions are identical to those of Figure 11.

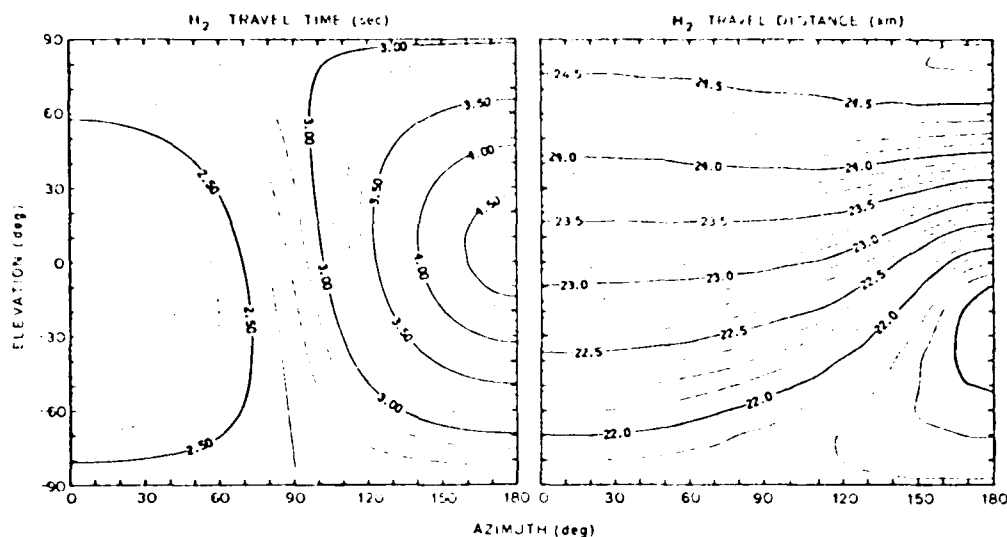


Fig. 13.  $H_2$  travel time and distance for releases under the same conditions as Figure 12. The  $H_2$  molecules are collisionally halted more rapidly than the  $CO_2$  molecules.

sphere, a typical molecule would move  $\lambda \ln(10)$  (2.3 mean free paths).

An alternate way to calculate the vapor travel distance is to consider the partitioning of the molecules between the natural, collisionless response  $[n_c(\mathbf{x}, t)]$ , and the forced, collision-dominated response  $[n_f(\mathbf{x}, t)]$ . When the number of molecules represented by  $n_c(\mathbf{x}, t)$  drops below 10% of the amount released, 90% of the gas will be in a collision-dominated state. The time,  $t_1$ , when this occurs is found from

$$\int_{-\infty}^{\infty} n_c(\mathbf{x}, t_1) d\mathbf{x}^3 = Q_0/10$$

The travel distance to the point where this occurs is the initial source velocity multiplied by  $t_1$ , neglecting the effects of gravity.

Both methods yield similar results for the vapor travel distance. The later formulation involving the spatial integration of the natural response is used here.

The following calculations consider releases of  $1 \times 10^{24}$  molecules being ejected for the Space Shuttle moving with a horizontal velocity of 7.7 km/s. The injection velocity relative to the Shuttle is 3.1 km/s. The travel distance is shown to be a function of the background atmospheric concentration, the injection azimuth and elevation, and the type of species released. In the release coordinate system, the elevation is measured from the horizontal plane, and the azimuth is the angle between the Shuttle velocity vector and the projection in the horizontal plane of the exhaust injection vector.

During solar minimum, the concentration of the neutral atmosphere at 400-km altitude is only  $3.24 \times 10^{13} \text{ m}^{-3}$  (see Table 2). Consequently, high-velocity vapor releases require the maximum time and travel distance to be collisionally stopped during this period. Figure 11 illustrates the travel time and distance for the sample point release. Releases with a downward velocity component require a minimum of 26 s and 200 km to stop. This corresponds to 74.7-km decrease in altitude and 185.5-km movement horizontally for a release at  $-90^\circ$  elevation. The travel distance for releases at zero degree elevation is close to 600 km, nearly independent of azimuth. Positive elevation angles yield travel distances greater than 600

km because the vapor moves into more tenuous regions of the atmosphere at higher altitudes.

For the maximum solar cycle conditions given in Table 2, the  $CO_2$  vapor stop times and distances are greatly reduced (Figure 12). The travel time has a minimum of 4.9 s for releases at  $-30^\circ$  elevation and  $0^\circ$  azimuth. The minimum travel distance (47 km) occurs for  $-50^\circ$  elevation and  $180^\circ$  azimuth. Supersonic releases in the horizontal plane travel a fixed distance (2.3 mean free paths) before they are collisionally stopped. Consequently, at zero degree elevation, the travel time has a strong azimuthal component, but the travel distance is nearly constant.

The calculations for solar maximum atmosphere are repeated with  $H_2$  instead of  $CO_2$  (Figure 13). The light  $H_2$  molecule rapidly loses momentum to the heavier background gas. The  $H_2$  vapor is stopped within 25 km of the release point, a factor of 2 less than the  $CO_2$  travel distance.

## 9. SUMMARY AND CONCLUSIONS

The theory outlined above is applicable to a wide range of gas release experiments. The analysis is specifically designed to model high-velocity (i.e., Space Shuttle) releases used for ionospheric depletion experiments. The theory, however, can be applied to experiments involving the injection of neutral vapors for use as tracers, instability triggers, and gravity wave generators.

The theory may be expanded in several areas. The effects of the high-velocity releases on the background atmosphere could be calculated simultaneously solving the coupled Boltzmann's equations (4) and (5). Collisional ionization and dissociation may be included in the modeling by adding a velocity-dependent loss term to (6). Chemical losses, due to reactions between the injected gas and the atmosphere, may be similarly handled.

The present analysis has predicted several fundamental effects on the vapor as it moves supersonically through a tenuous neutral atmosphere. The release will become elongated due to molecular scattering. During the collisional process heating will occur. The magnitude of the heating depends on the release velocity. The vapor travel distance is a function

of the background atmospheric concentration and of the direction of the vapor injection.

**Acknowledgments.** The author wishes to thank A. V. da Rosa, R. W. Schunk, and M. Mendillo for many useful discussions. This work was supported by the Office of Naval Research under contract N00014-77-C-0586 and by the National Aeronautics and Space Administration under grant NGR-05-020-001 and contract NAS 8-32852. Acknowledgment is made to the National Center for Atmospheric Research (NCAR) for computing time used in this research. NCAR is sponsored by the National Science Foundation.

The Editor thanks J. Zinn and D. C. Baxter for their assistance in evaluating this paper.

#### REFERENCES

- Anderson, D. N., and P. A. Bernhardt, Modeling the effects of an  $H_2$  gas release on the equatorial ionosphere, *J. Geophys. Res.*, **83**, 4777, 1978.
- Baker, C. T. H., *The Numerical Treatment of Integral Equations*, Clarendon Press, Oxford, 1977.
- Banks, P. M., and G. Kockarts, *Aeronomy*, vols. A and B, Academic, New York, 1973.
- Baum, H. R., The interaction of a transient exhaust plume with a rarified atmosphere, *J. Fluid Mech.*, **58**, 795, 1973.
- Baum, H. R., The interaction of an exhaust plume with a rarified atmosphere, paper presented at the Ninth Int. Symp. on Rarified Gas Dynam., Göttingen, West Germany, July 15-20, 1974.
- Baxter, D. C., and L. M. Linson, Dynamics of gas clouds released at satellite orbital velocity, in *Rarified Gas Dynamics*, edited by J. L. Potter, *Progr. Astronaut. Aeronaut.*, **51**, part 1, 177, 1977.
- Bernhardt, P. A., The response of the ionosphere to the injection of chemically reactive vapor, *Tech. Rep. 17, SU-SEL-76-008*, Stanford Univ., Stanford, Calif., 1976.
- Bernhardt, P. A., Three-dimensional, time-dependent modeling of neutral gas diffusion in a nonuniform, chemically reactive atmosphere, *J. Geophys. Res.*, **84**, 793, 1979.
- Bhatnagar, P. L., E. P. Gross, and M. Krook, Model for collisional processes in gases. I. Small amplitude perturbations in charged and neutral one-component systems, *Phys. Rev.*, **94**, 511, 1954.
- Brode, H. L., and J. E. Enstrom, Analysis of gas expansion in a rarified atmosphere, *Phys. Fluids*, **15**, 1913, 1973.
- Brook, J. W., and B. B. Hamel, Spherical source flow with a finite back pressure, *Phys. Fluids*, **15**, 1898, 1972.
- Draper, J. S., and J. A. Hill, Rarefaction of underexpanded flows, *AIAA J.*, **7**, 1400, 1969.
- Freeman, N. C., and R. E. Grundy, Solutions of the Boltzmann equation in an unsteady cylindrically symmetric expansion, *J. Fluid Mech.*, **31**, 723, 1968.
- Freeman, N. C., and D. R. Thomas, On spherical expansions into a vacuum, in *Advances in Applied Mechanics: Rarified Gas Dynamics*, suppl. 5, vol. 1, Academic, New York, 1969.
- Hedin, A. E., J. E. Salah, J. V. Evans, C. A. Reber, G. P. Newton, N. W. Spencer, D. C. Kayser, D. Alcayde, P. Bauer, I. Copper, and J. P. McClure, A global thermospheric model based on mass spectrometer and incoherent scatter data, I,  $N_2$  density and temperature, *J. Geophys. Res.*, **82**, 2139, 1977a.
- Hedin, A. E., C. A. Reber, G. P. Newton, N. W. Spencer, H. C. Brinton, H. G. Mayr, and W. E. Potter, A global thermospheric model based on mass spectrometer and incoherent scatter data MSIS, 2, Composition, *J. Geophys. Res.*, **82**, 2148, 1977b.
- Hirschfelder, J. O., C. F. Curtis, and R. B. Bird, *Molecular Theory of Gases and Liquids*, John Wiley, New York, 1954.
- Hoffman, H. S., and G. T. Best, The initial behavior of high altitude barium releases, II, The expanding vapor cloud, *J. Atmos. Terr. Phys.*, **36**, 1475, 1974.
- Holway, L. H., Similarity model of an explosion in a rarified Atmosphere, *Phys. Fluids*, **12**, 2506, 1969.
- Linson, L. M., and D. C. Baxter, Ion cloud modeling, *Rep. DNA 4455F*, Sci. Appl. Inc., Nov. 1977.
- Mendillo, M., and J. M. Forbes, Artificially created holes in the ionosphere, *J. Geophys. Res.*, **83**, 151, 1978.
- Muckenfuss, C., Mean-free path concepts in gas dynamics, *Phys. Fluids*, **5**, 103, 1962.
- Muntz, E. P., B. B. Hamel, and B. L. Maguire, Some characteristics of plume rarefactions, *AIAA J.*, **8**, 1651, 1970.
- Schunk, R. W., On the dispersal of artificially-injected gases in the night time atmosphere, *Planet. Space Sci.*, **26**, 605, 1978.

(Received January 4, 1979;  
revised February 28, 1979;  
accepted March 1, 1979.)

#### D. RADIOWAVE PROPAGATION

Propagation of radiowaves in the ionosphere can be substantially changed due to the injection of rocket exhaust vapors. Artificially produced plasma holes have strong plasma gradients which affect radio ray trajectories. We have examined propagation in the modified ionosphere for frequency ranges including VLF (3-30 kHz), HF (3-30 MHz), and VHF (30-300 MHz).

At VLF waves propagate through the ionosphere in whistler mode. Plasma holes will defocus these rays causing a reduction in signal strength. As plasma flows from above into ionospheric holes, field aligned reductions in plasma concentration are formed. These depletion tubes may act as guides for VLF waves in the magnetosphere.

At HF the plasma hole focuses transionospheric wave energy. The magnitude of the focusing can be 30 dB or more. Ray refraction in the bottom-side ionosphere is changed in the vicinity of a plasma hole. Depending on the relative locations of transmitter, hole and receiver, the changes in subionospheric propagation can include focusing, defocusing, multipath fading, or leakage of the signal out of the hole.

At VHF and above the ionospheric hole produces slight focusing of signals propagating from satellites to the ground. Changes in phase and polarization of VHF waves penetrating the hole provide experimental diagnostics.

Little is known about scintillations which could be induced by artificially produced holes in the equatorial ionosphere. If, as suggested in the previous section, irregularities form, they could introduce random phase and amplitude changes in VHF and UHF signals propagating through the disturbed region. This could have major impact on satellite communications.

The changes in radiowave propagation are described in greater detail in the following article which was presented at the AIAA 16th Annual Meeting, May 5-11, 1980, in Baltimore, Maryland. This paper has been submitted for publication to the Journal of Spacecraft and Rockets.



# CHANGES IN THE ELECTROMAGNETIC PROPERTIES OF THE UPPER ATMOSPHERE DUE TO ROCKET EFFLUENTS

Paul A. Bernhardt\*  
Stanford Electronics Laboratories  
Stanford University  
Stanford, California

## Abstract

Artificial reduction of the plasma concentrations in the ionosphere and magnetosphere can affect E-M wave propagation. The molecular species found in rocket exhaust vapors promote recombination of electrons and ions (i.e.,  $O^+$ ,  $H^+$ , and  $He^+$ ) in the upper atmosphere. This recombination produces localized regions with strong variations in radio refractive index. Regions of ionospheric plasma reduction produce focusing at HF and VHF frequencies and defocusing at VLF frequencies. Subionospheric propagation in the vicinity of an artificial plasma hole can suffer the effects of multi-path fading and defocusing by reflection at the sides of the hole. Should irregularities form because of the plasma gradients, amplitude scintillations will be introduced in waves passing through the region.

## I. Introduction

The earth's plasma atmosphere can be divided into four regions with approximate boundaries given as follows. The D-region is at altitudes between 70 and 90 km. The E-region extends from 90 to 120 km altitude. The F-region, lying between 120 and 800 km, contains the bulk of the ionospheric plasma. Above the ionosphere is the magnetosphere which extends from 800 km altitude to over 10 earth radii.

The firing of rocket engines in the upper atmosphere releases vapors which can temporarily neutralize some of the plasma in the F-region and to a lesser degree, in the magnetosphere. This process produces regions of localized plasma reduction called plasma "holes". Radio waves propagating through the disturbed regions can be strongly refracted and scattered.

The object of this paper is to survey the variety of effects that artificially-produced plasma depletions can have on electromagnetic waves. For this study, numerical models of the upper atmosphere are used to predict the size and durations of the depletions. Two and three-dimensional raytracing programs are employed to investigate the changes in the radiowave ray trajectories. This study is motivated by the need to evaluate the consequences of temporary alteration of the ionosphere. Such alteration might be produced by the launches required to construct large, orbiting space systems such as the Solar Power Satellite (SPS).

\* Research Associate, Radioscience Laboratory

## II. Molecular Species Present in Rocket Exhaust

Exhaust vapors from chemically powered rockets may react with the plasma in the upper atmosphere. This factor is not normally considered by the designer of rocket propulsion systems. The designer considers a rocket fuel in terms of performance rather than in terms of effect on the environment.

Figure 1 illustrates a comparison of propellants by specific impulse and bulk density. All of the propellants in this figure produce exhaust species which reach chemically in the ionosphere, causing a reduction in plasma concentration. Designing a useful chemical propulsion system which does not eject reactive exhaust vapors may not be feasible.

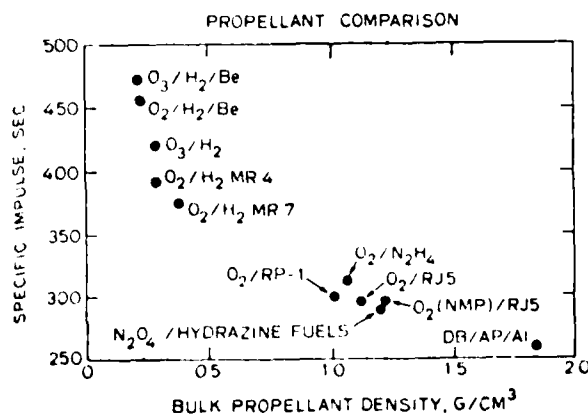


Fig. 1 Performance comparison of eleven propellants.

Table I lists the exhaust species for two solid rocket propellants. The species designated by \* are known to produce modification of the ionosphere. The exhaust from solid rocket motors may also contain chlorine compounds which can effect the stratospheric ozone concentration. Most solid rockets burn only in the lower atmosphere and do not affect the ionosphere.

Exhaust vapors from liquid rocket engines usually contain fewer species than are produced by solid rockets (Table II). This exhaust is mainly composed of oxides and hydrogen and carbon as well as unburned molecular hydrogen. Most of these gases will produce plasma depletions if injected

Table I. Typical Solid Rocket Exhaust Species and Concentrations

Oxidizer	NH <sub>4</sub> ClO <sub>4</sub> --66%		Double-base	
Binder	(CH <sub>2</sub> ) <sub>x</sub>		--	
Fuel	Al--22%		Al--22%	
Combustion temperature (°K)	3644		4017	
Exhaust products, mole fraction	H	0.0283	H	0.1036
	Cl	0.0084	O	0.0004
	*OH	0.0006	*OH	0.0045
	HCl	0.5462	*H <sub>2</sub>	0.7852
	*H <sub>2</sub>	1.3183	*H <sub>2</sub> O	0.1404
	*H <sub>2</sub> O	0.1730	CO	1.0910
	CO	0.8339	*CO <sub>2</sub>	0.0295
	*CO <sub>2</sub>	0.0192	*NO	0.0004
	*N <sub>2</sub>	0.2869	*N <sub>2</sub>	0.7951
	AlCl	0.0011	Al	0.0002
	AlCl <sub>2</sub>	0.0028	AlO	0.0001
	AlCl <sub>3</sub>	0.0001	Al <sub>2</sub> O	0.0004
	Al <sub>2</sub> O <sub>3</sub>	0.4057	Al <sub>2</sub> O <sub>3</sub>	0.4071

\* Promotes ionospheric plasma reduction.

Table II. Typical Liquid Rocket Exhaust Species and Concentrations

Oxidizer	N <sub>2</sub> O <sub>4</sub>		O <sub>2</sub>
Fuel	MMH		H <sub>2</sub>
Mixture ratio (O/F)	1.65		6.0
Theoretical I <sub>s</sub> , sec	313		388
Combustion temperature (°K)	3250		2869
Exhaust products, mole fraction	*H <sub>2</sub>	0.2411	0.2500
	*H <sub>2</sub> O	0.2738	0.7500
	CO	0.0501	0
	*CO <sub>2</sub>	0.1216	0
	*N <sub>2</sub>	0.3134	0

\* Promotes ionospheric plasma reduction.

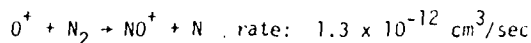
into the F-region ionosphere.

The spatial extent of the ionospheric modification is affected by 1) the total amount of exhaust released and 2) the manner the exhaust vapors are laid down<sup>1,2</sup>. The amount released depends on the engine flow rates and the duration of the engine burn. The flow rate of the Space Shuttle<sup>3</sup> Orbital Maneuvering Subsystem is 8.71 kg S<sup>-1</sup> engine<sup>-1</sup> and of the Space Shuttle Main Engine (SSME) is 468.4 kg S<sup>-1</sup> engine<sup>-1</sup>. The proposed heavy lift launch vehicle (HLLV) for the SPS uses 14 SSME's, producing a flow of 6557.6 kg/sec.

### III. Chemical Mechanisms for Ionospheric Hole Formation

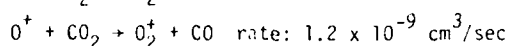
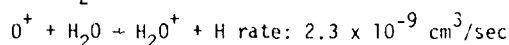
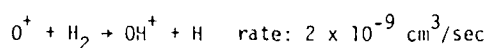
A complete description of ionospheric hole formation involves chemistry, gas dynamics, diffusion and thermal processes. The details of these processes can be found in several reports<sup>3,4</sup>.

Briefly, plasma holes are formed by chemical reaction of vapors in rocket plumes with ions in the F-layer. Normally, the O<sup>+</sup> ion, which makes up the bulk of the ionosphere, is removed by the following reaction.



The rate of this reaction is at least 1000 times lower than the rates for the reactions between O<sup>+</sup> and most rocket exhaust species.

Consider competing reactions with rocket exhaust



The relatively large rates for these reactions cause the rapid removal of the O<sup>+</sup> ion. The molecular ions (NO<sup>+</sup>, OH<sup>+</sup>, H<sub>2</sub>O<sup>+</sup>, and O<sub>2</sub><sup>+</sup>) quickly recombine with electrons at rates around  $2 \times 10^{-7}$  cm<sup>3</sup>/sec. Similar reactions can cause reduction of the H<sup>+</sup> and He<sup>+</sup> ions in the magnetosphere.

After the exhaust vapors are released, they will disperse mainly through diffusive expansion<sup>1</sup>. The lifetime of the ionospheric hole is influenced by transport of ions into the affected region as well as by re-ionization of the neutrals by the sun's extreme ultraviolet radiation. The size of the hole is controlled by the expansion and transport of the injected exhaust vapors. All of the processes are contained in the numerical models we have used in our studies<sup>3,4</sup>.

The models are used to generate estimates of disturbances produced by the release of vapors in the ionosphere. The changes in radio wave propagation are investigated by tracing rays through the perturbed ionospheric regions. The rest of this paper describes typical effects of artificial ionospheric holes on radio waves propagating at VLF (3-30 kHz), at HF (3-30 MHz), at VHF (30-300 MHz) and above.

### IV. Modification of Propagation VLF Waves in the Ionosphere

Long distance propagation of very low frequency (VLF) waves may be either 1) via the earth-ionosphere waveguide or 2) via field aligned ducts in the earth's magnetosphere. The first type of propagation employs the earth's surface and the lower edge of the ionosphere for guiding the waves. Any modification of the ionosphere's lower boundary will change the characteristics of the earth-ionosphere waveguide.

The lower ionosphere is composed of positive polyatomic ions such as NO<sup>+</sup>, O<sub>2</sub><sup>+</sup> (in the D and E

region), negative polyatomic ions such as  $O_2^-$  (D region) and hydrated positive ions such as  $H_3O^+$  (D region). These ions are not nearly as sensitive to the chemical changes as are the  $O^+$  ions of the F-layer. Consequently, the effect of rocket exhaust on propagation via the earth-ionosphere waveguide is expected to be small.

The second type of VLF propagation (called whistler mode) is illustrated in Figure 2. A VLF electromagnetic wave is transmitted from a source into the earth-ionosphere waveguide. Some of the wave energy leaks upward through the bottomside ionosphere, traveling in an unguided mode. If this energy is captured by an enhanced column of plasma (called an enhancement duct), the wave can be guided along the earth's magnetic field lines to the conjugate hemisphere. Amplification may occur as the wave interacts with the radiation belt particles in the magnetosphere<sup>5</sup>. Radio rays leaving the duct will travel in an unducted mode to the bottomside ionosphere. If the ray direction is nearly perpendicular to the ionosphere, signals will couple into the earth-ionosphere waveguide and may be received on the ground. Further details on whistler mode propagation can be found in the text by Helliwell<sup>5</sup>.

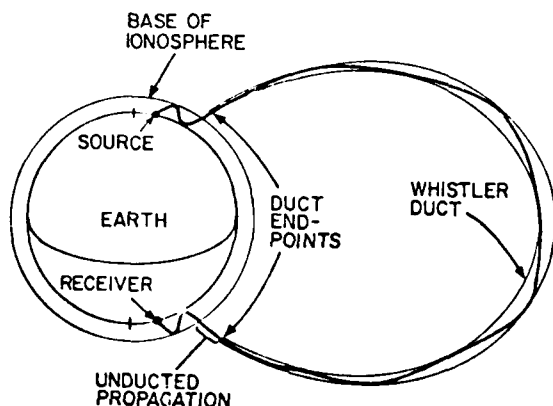


Fig. 2 Schematic of the magnetospheric propagation circuit for VLF waves.

Modification of the F-region ionosphere will change the coupling between the earth-ionosphere waveguide and the ducts in the magnetosphere. This is demonstrated by tracing 5 kHz rays through an ionosphere that was modified by the release of 100 kg of  $H_2$  at 300 km altitude. The electron density contours one minute after the  $H_2$  release, are illustrated in Figure 3.

For rays to be captured by a whistler duct, their wave normal components must be nearly aligned with the earth's magnetic field. At high geomagnetic latitudes, the magnetic field lines are nearly vertical. Upward propagating VLF waves have their wavenormals refracted vertically as they enter the ionosphere at the lower boundary. As these waves propagate in a horizontally stratified ionosphere, the wavenormals tend to remain vertical and the waves tend to couple into any enhancement ducts they encounter.

#### NIGHT-TIME ELECTRON CONCENTRATION LOG<sub>10</sub>(Number Density, cm<sup>-3</sup>)

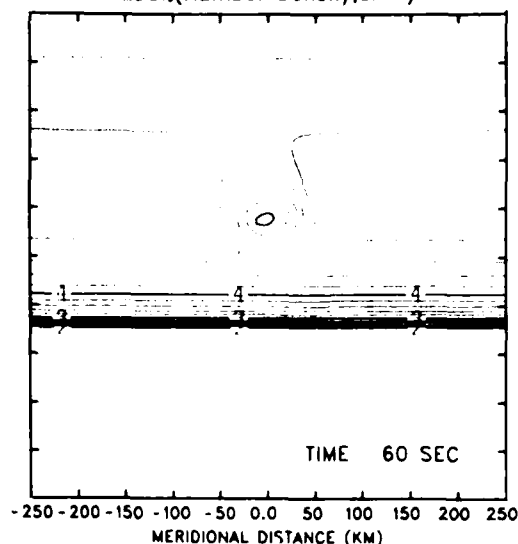


Fig. 3 Ionospheric hole produced by the point release of 100 kg of  $H_2$  at 300 km altitude. One minute after the release, the central plasma concentration is reduced by a factor of 10.

The wavenormals of the rays are sharply bent by the plasma gradients of an ionospheric hole. Figure 4 illustrates the bending of 5 kHz rays by the ionospheric hole of Figure 3. The rays are emitted from a ground station located at 55° geomagnetic latitude. The three rays to the left of the hole are unaffected. In the vicinity of the hole, the rays are defocused and their wavenormals are bent. (The wavenormal directions are indicated by the arrows at the end of the ray trajectories). These rays cannot couple into ducts in the magnetosphere.

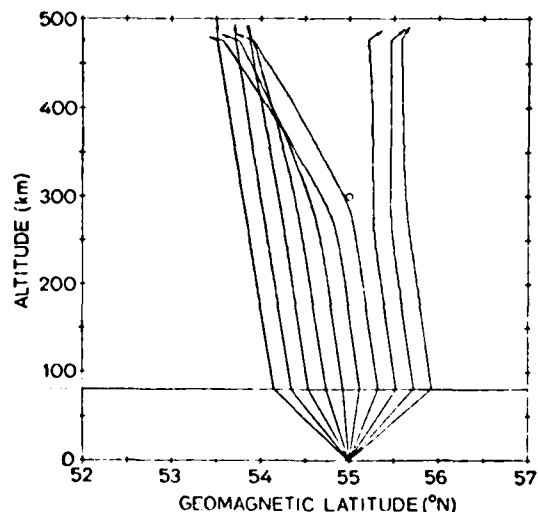


Fig. 4 Defocusing of 5 kHz rays by an ionospheric hole centered on the small circle.

A reciprocal effect occurs for signals exiting a duct over an ionospheric hole. Figure 5 illustrates the defocusing and wavenormal bending for 5 kHz rays, propagating downward. Without the hole, all rays would cross the lower ionosphere and propagate to the earth's surface. Between 53.6° and 56° geomagnetic latitude, the ionospheric hole prohibits transmission to the ground of the 5 kHz wave.

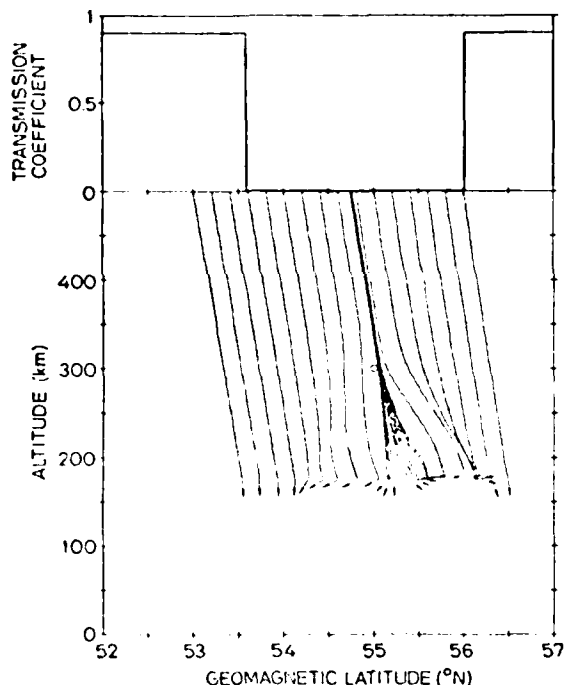


Fig. 5 Refraction of downward propagating rays by an F-region depletion. A transmission coefficient of zero indicates rays which do not penetrate the bottomside ionosphere.

Figure 6 illustrates the required wavenormal angle(s) at 500 km altitude for propagation through the ionospheric hole to the earth's surface. The wavenormal direction is defined with respect to the vertical. The dashed portion of the curve shows where strong defocusing occurs. Rays leaving enhancement ducts have wavenormal angles usually less than 15°. In regions where the penetration wavenormal angle is greater than this value, coupling between whistler ducts and the earth-ionosphere waveguide does not occur.

Fading of the signal amplitude will occur if two or more rays reach the ground receiver, each ray having propagated on a disjoint path. Between 53.6° and 53.9° latitude, rays with three different wavenormal angles can reach the earth's surface. Consider a VLF satellite transmitting a 5 kHz omnidirectional signal from a 500 km orbit. When this satellite enters the fading region (Figure 6), amplitude fluctuations will be perceived on the ground.

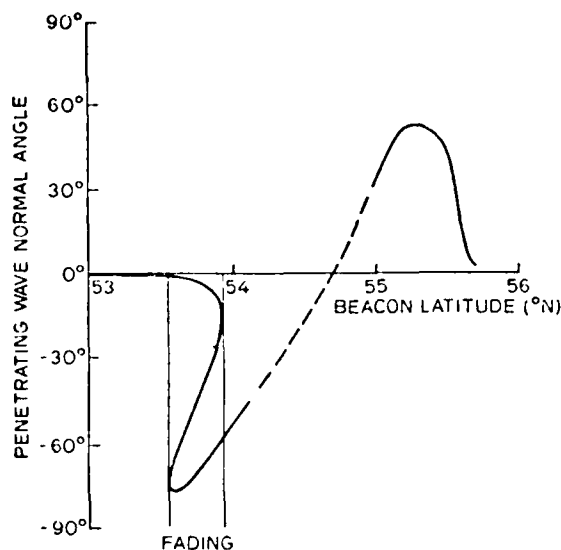


Fig. 6 Required wavenormal angle at 500 km altitude for ground reception of a 5 kHz wave. The angles are defined with respect to the vertical.

One further way that VLF propagation in the magnetosphere may be modified by exhaust vapors is with the creation of artificial ducts. When the F-layer is locally depleted, plasma flows along magnetic field lines from the magnetosphere into the depleted region. This flow will produce a tube of reduced plasma concentration extending up into the magnetosphere. This "depletion duct" takes three or more hours to form.

Bernhardt<sup>3</sup> has made estimates of the amount of reduction in the content of a magnetic flux one would expect from vapor releases. For instance, 1000 kg of H<sub>2</sub> released at 300 km altitude into the daytime ionosphere is calculated to produce 10% reduction in the electron content of a tube centered along a L=4 (earth radii) magnetic fieldline. The radius of this tube will be 650 km at the equator.

This type of duct may be able to guide VLF waves in the magnetosphere. As mentioned previously, enhancement ducts are efficient guides of VLF waves. Depletion ducts can also guide VLF, using one of two modes. The first mode involves large wavenormal angles for rays which do not penetrate the lower ionosphere to the ground. The second mode, involves trapping at the lower edge of the depletion duct<sup>6</sup>. This "one sided" mode can be excited from the ground for guiding a wave to the conjugate hemisphere. A depletion duct of 10% should be sufficient for this type of guiding.

#### V. Artificial Changes in High Frequency (3-20 MHz) Waves.

The peak concentration of the F-layer defines a lower limit for the frequency of penetration of HF waves. This frequency is given by  $f_oF2 =$

$[80.6 N_{\max}]^{1/2}$  Hz where  $N_{\max}$  is the peak concentration in electrons  $m^{-3}$ . An ionospheric hole, located at the F-layer peak, will decrease  $f F_2$ , allowing lower frequency (HF) waves to penetrate. This effect was proposed by Papagiannis and Mendillo<sup>7</sup> for use in low frequency radio astronomy.

Refraction of an HF wave by the plasma gradients of the ionospheric hole will greatly distort the propagating phase front. The magnitude of this distortion is a function of the wave frequency, the plasma gradients in the hole and the direction of wave propagation through the hole.

Figure 7 is an example of downward propagating HF rays through the ionospheric hole shown in Figure 2. The rays are superimposed on contours of constant electron concentration. The ordinary left-hand circularly polarized mode is designated O-mode. The effect of the reduction in plasma concentration is to focus the downgoing waves. This is in contrast with the defocusing of VLF waves discussed in the previous section. In the example shown in Figure 7, the focal point for the 7 MHz O-mode lies on the ground. The ionospheric "lens" produced by a 100 kg release of hydrogen at 300 km altitude is roughly equivalent to a perfect lens with a diameter of 36 km. The use of such a lens for radio astronomical observations has been proposed by Bernhardt and da Rosa<sup>8</sup>.

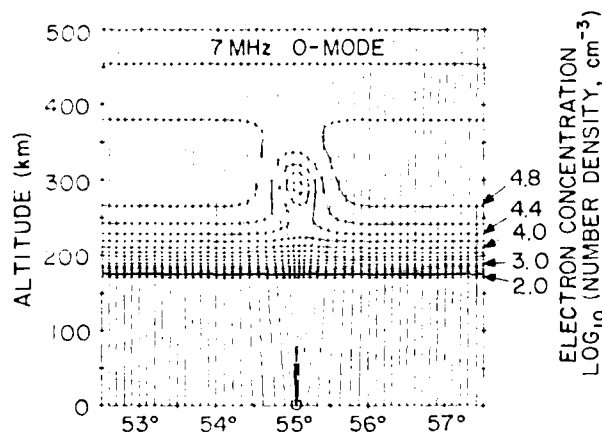


Fig. 7 Propagation of a 7 MHz ordinary wave, through the ionospheric hole illustrated in Figure 3. The downward propagating rays are focused at the encircled point.

Ionospheric plasma holes can also affect the propagation of high frequency waves between two points on the earth's surface (called subionospheric propagation). Depending on the geometry of the transmitter, receiver and ionospheric hole, the HF signals can experience focusing, defocusing and/or fading.

Representative effects of ionospheric holes on HF propagation are taken from the work of Helms and Thompson<sup>9</sup>. They traced rays through an ionospheric perturbation which we estimate could be produced by the release of 3000 kg of  $H_2$  into the nighttime F-layer. In their work, the electron concentration is normalized by square of the frequency, as follows:  $X = 80.6 N_e / f^2$  where  $f$  is the wave frequency in Hz and  $N_e$  is the electron concentration in  $m^{-3}$ .  $X_{\max}$  is the value at the F-layer peak given by  $X_{\max} = 80.6 N_{\max} / f^2$ .

The following is a summary of the discussion presented by Helms and Thompson<sup>9</sup>. With  $X_{\max} = 4$  (for example with  $N_{\max} = 1 \times 10^{12} m^{-3}$  and  $f = 4.5$  MHz), the unperturbed ionosphere produces the O-mode trajectories shown in Figure 8. The ionospheric holes modify the trajectories as shown in Figure 9. The center of the hole is indicated by a dashed, vertical line.

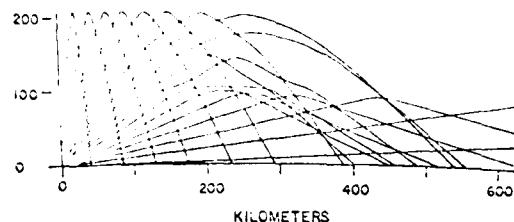


Fig. 8 Ray path trajectories in an undisturbed ionosphere with  $X_{\max} = 4$  (from Helms and Thompson<sup>9</sup>).

Without the hole, the point of maximum ray altitude for rays with  $20^\circ$  to  $40^\circ$  elevation angles is 220 km from the transmitter. With the hole placed 440 km away from the transmitter (Figure 9a) the same rays propagate greater distances reaching maximum altitudes as much as 600 km away from the transmitter. This could have a desirable effect on long distance communications.

Moving the hole closer to the transmitter affects rays with higher initial elevation angles. For hole-transmitter separations less than 220 km, some of the rays are reflected back to the transmitter (Figures 9b and c). Finally, for separations less than 120 km, some rays escape through the ionospheric hole (Figure 9c). When the hole is directly over the transmitter (Figure 9d) the rays are reflected once or twice by the sides of the hole before reaching the ground.

In some cases, an ionospheric hole can produce focusing or defocusing of HF waves. Reflection from the side of the hole tends to spread the ray trajectories (Figure 10a). By lowering the wave frequency from 4.5 MHz ( $X_{\max} = 4$ ) to 2.8 MHz ( $X_{\max} = 10$ ) focusing of the reflected rays can be produced (Figure 10b).

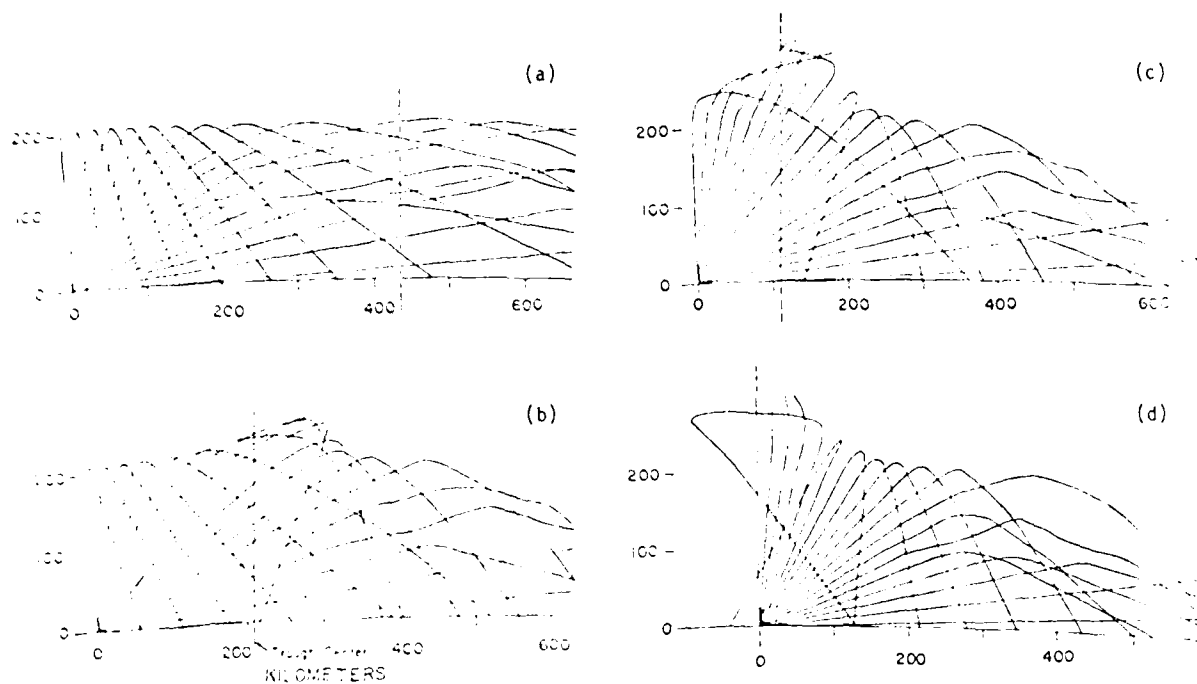


Fig. 9 Ray path trajectories as a function of location for a hole with a depression ratio of 0.1, a halfwidth of 222 km, and  $X_{\max} = 4$  (From Helms and Thompson<sup>9</sup>).

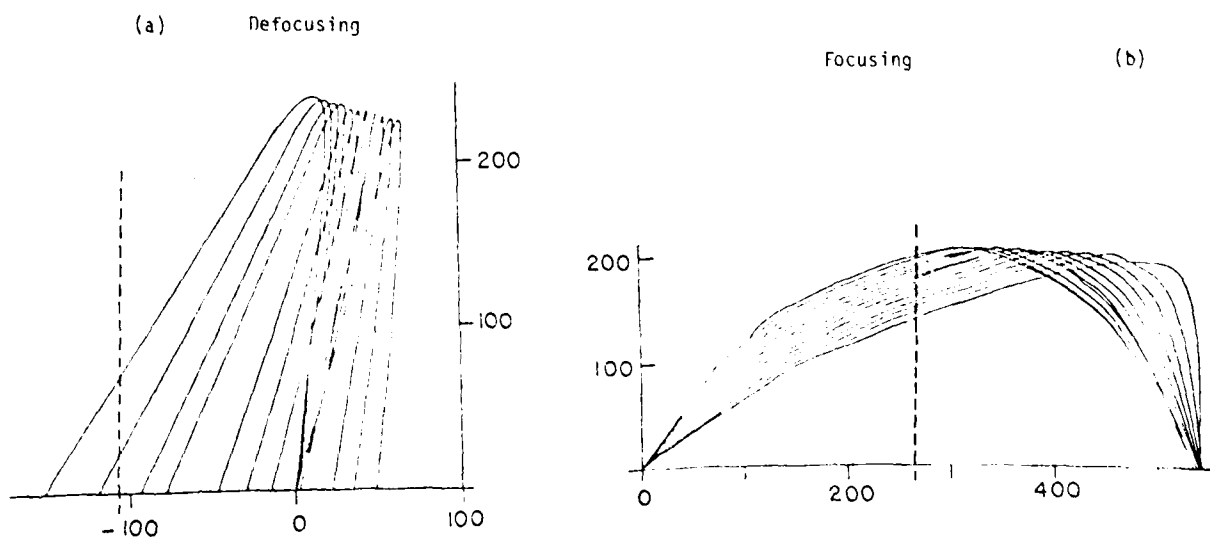


Fig. 10 Focusing and defocusing effects due to propagation through an ionospheric hole (From Helms and Thompson<sup>9</sup>).

An attempt was made to observe perturbations of HF communications by rocket-induced ionospheric holes. On Sept. 20, 1979, a large hole was created by the Centaur stage of a rocket placing the HEAO-C satellite into orbit (see Mendillo<sup>10</sup>). Radio amateurs were solicited to participate in an ex-

periment to observe the effects of the hole on communications<sup>11</sup>. Beacon transmissions 3.6, 7.1, 14.1, 21.1, 28.1 and 50.1 MHz were made from Puerto Rico. Signal strength measurements from over 150 amateurs in the continental United States are reported. The reports indicated that some

small communication effects may have been produced. These effects, however, were of the same magnitude that one would expect with the ionosphere's normal variability. The communication effects of the HEAD-C launch are still under study.

From the theoretical examples, we see that ionospheric holes can produce a variety of changes on subionospheric HF communications. Holes directly over a transmitter will defocus the wave components with large elevation angles. Under certain specialized conditions, holes several hundred kilometers from a transmitter can produce focusing resulting in an enhancement of signal amplitude. Multi-path propagation produced by the hole may cause fading.

#### V. Effects at VHF and Above (Frequencies greater than 30 MHz)

As the wave frequency is increased above 30 MHz, the refraction by the ionospheric gradients becomes less pronounced. Above 100 MHz, the ray bending is so weak that propagation between two points on the ground (via ionospheric reflection) becomes unlikely. Consequently, the only effects of interest occur for trans-ionospheric propagation. An example of this might be signals propagating from a satellite through the ionosphere to the ground.

Focusing will occur for VHF (30 - 300 MHz) signals travelling vertically through an ionospheric hole. The phenomenon is similar to that shown in Figure 7 but to a much lesser degree. For frequencies above 30 MHz, the amplitude increase on the ground is approximately given by

$$G = 1 + \frac{2z}{a^2}$$

where  $\lambda$  is the wavelength,  $z$  is the altitude of the hole,  $a$  is the halfwidth of the hole,  $\phi$  is the phase change through the center of the hole and  $G$  is the amplitude gain resulting from propagation through the hole. The phase perturbation can be found from the integrated vertical electron content with and without the hole

$$\phi = 8.44 \times 10^{-7} \Delta I$$

where  $\Delta I$  is the reduction in electron content (in  $m^{-2}$ ) through the center of the hole and  $f$  is the wave frequency (in Hz).

As an example, consider an ionospheric hole centered at an altitude of 300 km with a content reduction  $\Delta I = 6 \times 10^{16} m^{-2}$  and a size  $a = 20$  km. For a wave frequency  $f = 140$  MHz, one obtains an amplitude gain  $G = 1.1$ . This .8 dB gain is small compared with naturally occurring variations in signal amplitude.

The reduction in electron content associated with ionospheric holes produces changes in the phase and polarization of VHF waves. Measurements of these changes have been made by a number of workers to detect and study artificially produced holes<sup>12, 13, 14, 15</sup>. Recent measurements made after the launch of the HEAD-C satellite are shown in Figure 11. The data for this figure was provided by Stanford University, Boston University, Air Force Geophysical Laboratory, and the Department of the Army, Fort Monmouth. More details can be found in the paper in this session by Mendillo<sup>10</sup>.

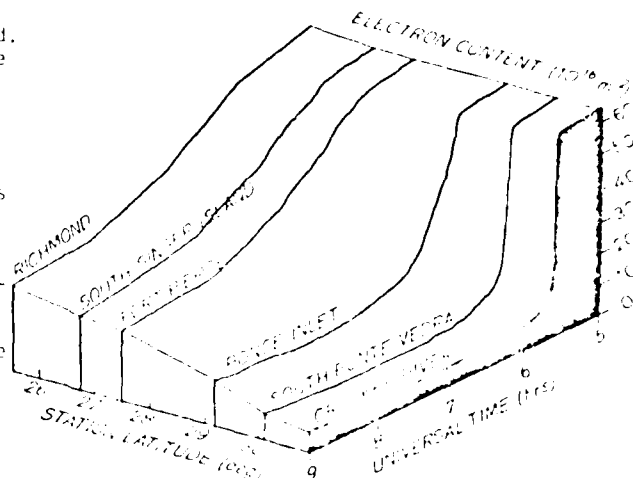


Fig. 11 Electron content changes associated with the launch of HEAD-C. The launch took place at 0628 UT. The rocket exhaust first crossed the Vhf propagation path terminating on the Crooked River station. The measurements were made using a Vhf signal transmitted from the STRIO satellite located in geosynchronous orbit at 14.77° W longitude, 1.07° S latitude.

The previous discussion concentrated on fluctuations in radiowave propagation due to the smooth plasma gradients which form the plasma hole. The scale size of these gradients is the order of tens of kilometers or more. One should consider, however, the possibility of the hole breaking up into irregularities. As suggested by Anderson and Bernhardt<sup>16</sup> and by Ossakow, et al.<sup>17</sup>, holes created in the bottomside F-region at the magnetic equator may become unstable. This phenomena occur naturally, and has been reported by a number of researchers<sup>16, 17, 18</sup>.

The instability growth rate increases as the bottomside plasma gradients become steeper. This growth rate, however, is decreased by enhanced electron-ion recombination in the region. In the case of exhaust releases, the mechanism which steepens the bottomside F-layer also increases the recombination in the region. Consequently, the exhaust vapors may damp-out any instabilities which would otherwise form. If the plasma hole and the exhaust vapors become separated, the instability can grow. Electric fields and/or neutral winds may be adequate for transporting the hole and the exhaust vapors away from each other.

The effects of the irregularities on VHF (and higher frequency) propagation depends on the size and distribution of the irregularities. Naturally occurring irregularities have been known to produce severe amplitude and phase scintillations in trans-ionospheric propagating signals.

#### VII. Concluding Remarks

Current plans for the Solar Power Satellite<sup>20</sup> call for the multiple launches of chemical rockets for transportation of cargo and crews. The Heavy Lift Launch Vehicle (HLLV), the Personnel Launch Vehicle (PLV), and the Personnel Orbit Transfer

Vehicle (POLL) may deposit a substantial amount of exhaust vapors in the upper atmosphere. The magnitude and the duration of the ionospheric plasma reduction produced by the engine burns depends on the particular burn profiles. These plasma reductions can be simulated with a number of existing models (3,4,11). The refraction effects by the chemically-produced plasma-gradients can be readily accomplished by coupling ray tracing to the ionospheric models.

The major uncertainty in this field of research is whether or not exhaust releases will trigger irregularities in the equatorial ionosphere. This is of special interest to the SPS program because the HLLV's are expected to conduct orbit circularization burns at the equator. The amount of material released during one of these burns may be as much as  $8 \times 10^3$  kg over a region 1200 km long. Should the HLLV make an expected 391 flights per year, the exhaust vapors may continually stimulate ionospheric irregularities which could adversely affect trans-ionospheric propagation in the disturbed region. More theoretical and experimental work needs to be done in this area.

(Acknowledgement) This work was supported by the Office of Naval Research Grant N00014-77-C-0056 and Air Force National Laboratory Contract 31-109-38-5071.

#### VI. References

- Bernhardt, P. A., Three-dimensional, Time-Dependent Modeling of Neutral Gas Diffusion in a Nonuniform, Chemically Reactive Atmosphere, *J. Geophys. Res.*, **84**, 793, 1979a.
- Bernhardt, P. A., High Altitude Gas Releases: Transition from Collisionless Flow to Diffusive Flow in a Nonuniform Atmosphere, *J. Geophys. Res.*, **84**, 4341, 1979b.
- Bernhardt, P. A., The Response of the Ionosphere to the Injection of Chemically reactive Vapors, Stanford University Tech. Rept. No. 17, SU-SEL-76-009, 1976.
- Anderson, D. A. and P. A. Bernhardt, Modeling the Effects of an  $H_2$  Gas Release on the Equatorial Ionosphere, *J. Geophys. Res.*, **83**, 4777, 1978.
- Helliwell, R. A., Whistlers and Related Ionospheric Phenomena, Stanford University Press, Stanford, California, 1965.
- Inan, U. S., and T. F. Bell, The Plasmapause as a VLF Waveguide, *J. Geophys. Res.*, **82**, 2819, 1977.
- Papagiannis, M. D., and M. Mendillo, Low Frequency Radio Astronomy Through an Artificially Created Ionospheric Window, *Nature*, **255** (5503), 42-43, 1975.
- Bernhardt, P. A., and A. V. da Rosa, A Refracting Radiotelescope, *Radio Sci.*, **12**, 327, 1977.
- Helms, W. J. and A. D. Thompson, Ray-tracing Simulation of Ionization Through Effects Upon Radio Waves, *Radio Sci.*, **8**, 1125, 1973.
- Mendillo, M., Investigations of Atmospheric Effects Due to HEAO-C Launch, Session No. 75, Paper No. 7, AIAA 16th Annual Meeting, May 5-11, 1980.
- Bernhardt, P. A., J. A. Klobuchar, O. G. Villard, Jr., R. A. Simpson, J. G. Troster, M. Mendillo, and J. H. Reisert, The Great Ionospheric Hole Experiment, *QST*, **58**, No. 9, 22, 1979.
- Mendillo, M., G. S. Hawkins, and J. A. Klobuchar, A Large-scale Hole in the Ionosphere Caused by the Launch of Skylab, *Science*, **187**, 343, 1975a.
- Clynch, J. R., C. Rushing, and J. A. Klobuchar, Faraday and Differential Doppler Observations of the Lagopedo Ionospheric Depletions, *EOS Trans. AGU*, **59**, 344, 1978.
- da Rosa, A. V., and P. A. Bernhardt, Rocket-Borne Beacon Measurements of Chemically-Induced Ionospheric Depletions, *EOS Trans. AGU*, **59**, 334, 1978.
- Bernhardt, P. A. Ionospheric Modification by Rocket Effluents - Interim Progress Report, Technical Report E326-1, Stanford University, Stanford, California, January 1, 1980.
- Woodman, R. F. and C. LaHoz, Radar Observations of F-region Equatorial Irregularities, *J. Geophys. Res.*, **81**, 5447, 1976.
- McClure, J. P., W. B. Hanson and J. H. Hoffmann, Plasma Bubbles and Irregularities in the Equatorial Ionosphere, *J. Geophys. Res.*, **82**, 2650, 1977.
- Yeh, K. C., H. Soichev, C. H. Liu, and F. Bonelli, Ionospheric Bubbles Observed by the Faraday Rotation Method at Natal Brazil, *Geophys. Res. Letters*, **6**, 473, 1979.
- Ossakow, S. L., S. T. Zalesak, and B. E. McDonald, Ionospheric Modification: An Initial Report on Artificially Created Equatorial Spread-F, *Geophys. Res. Letters*, **8**, 691, 1978.
- Piland, R. O. The Solar Power Satellite Concept Evaluation Program, Radiation Energy Conversion in Space, *Progress in Astronautics and Aeronautics*, Vol. **61**, 3, 1978.
- Zinn, J. and C. D. Sutherland, Effects of Rocket Exhaust Products in the Thermosphere and Ionosphere, *Space Solar Power Review* (in press) 1980.



## E. ANALYSIS OF VLF PHASE AND AMPLITUDE DATA

We have made a systematic search of VLF phase and amplitude data for rocket launch effects. The data set is based on signals received at Byrd Station, Antarctica after having propagated through the earth-ionosphere waveguide from one of several Standard Frequency and Time Stations operating at VLF. The data, taken during the time period of September 1964 and April 1970, has not been previously analyzed. Signals propagating along great-circle-paths in the vicinity of Cape Canaveral, Florida, were examined during times of rocket launches. There were no systematic fluctuations in the phase of amplitude that could be associated with rocket launches. From this, we conclude that rocket exhaust releases in the lower ionosphere are not sufficient to produce significant fluctuations in VLF signal propagation on subionospheric paths.

We did, however, isolate periodic fluctuations in the data that were attributed to the lunar tide. Also, the VLF amplitude data was shown to contain a significant increase in signal strength. The effect may be due to power-line-induced precipitation of energetic electrons which ionize the D-region ionosphere. The details of this analysis are given in the following article which is to be submitted to the Journal of Geophysical Research.

## PERIODIC FLUCTUATIONS IN THE EARTH-IONOSPHERE WAVEGUIDE

Paul A. Bernhardt

Kent M. Price

Radioscience Laboratory, Stanford Electronics Laboratories,  
Stanford University, Stanford, California 94305

James H. Crary

Jefferson County Data Processing Department  
Golden, Colorado 90419

### ABSTRACT

VLF phase and amplitude measurements made in 1967 at Byrd Station, Antarctica, using 18.6 kHz transmissions from NLK, Washington, have been analyzed for lunar-induced and hebdomadal variations. The VLF propagation path was 14,250 km in length, and nearly constant in longitude. The lunar-induced variations are found to be  $\pm 18^\circ$  in phase and  $\pm 0.26$  dB in amplitude and are explained by height changes in the D-region of the ionosphere. The hebdomadal variation in VLF amplitude shows a 0.46 dB increase during the Sunday daylight hours, relative to the Monday-Saturday average, and is ascribed to man-made changes in the D-region.

### INTRODUCTION

The phase and amplitude of VLF signals propagating in the earth-ionosphere waveguide are affected by fluctuations in the D-region. These fluctuations can be either irregular transient or periodic. Irregular or transient disturbances have been associated with solar flares, magnetic activity, meteor showers, whistler-induced electron precipitation and geomagnetic storms (Chilton et al., 1964; Potemra and Rosenberg, 1973; Muraoka, 1979; and references cited in these works). Sources of periodic

fluctuations may include the earth's rotation relative to the sun, the solar 27 day rotation, the lunar semi-diurnal tide and the hebdomadal variations in power line radiation. In this paper, only the periodic changes in VLF amplitude and phase are considered.

The lunar-induced semi-diurnal variation in VLF phase has been previously investigated by Brady and Crombie (1963). They found that the lunar tide produces about  $\pm 1^\circ$  of variation in the phase measured along propagation paths 4000 to 5000 km in length. This phase change was shown to be equivalent to a  $\pm 0.1$  km fluctuation in the height of the D-region. The peak height of the D-region was found to occur one hour before upper and lower transit of the moon. It had been previously shown by Appleton and Beynon (1949) and by Mitra (1955) that maximum absorption occurs approximately one or two hours before lunar transit. If the D-region produces the absorption, it seems puzzling that the peak absorption should occur when the layer is elevated to its highest extent by the lunar atmospheric tide. In this paper, both VLF amplitude and phase data are analyzed to provide further information about the lunar tidal effects in the D-region.

Another, more recent puzzle concerns the effects of power line radiation (PLR) on the energetic particle population in the magnetosphere. A number of papers (Helliwell et al., 1975; Bullough et al., 1976; Park 1977; Lurette et al., 1977; Park and Helliwell, 1978; Lurette et al., 1979; Park and Miller, 1979; and Lurette et al., 1980) have suggested that PLR may 1) trigger VLF emissions in the magnetosphere and 2) change the trajectories of energetic electrons causing particle precipitation into the upper atmosphere. If the energetic electrons

ionize the D-region, they might produce a measurable change in VLF signals propagating in the earth-ionosphere waveguide. Fraser-Smith (1979) and Park and Miller (1979) have suggested that effects due to PLR may be identified by looking for hebdomadal periodicities in the data. The lower usage of electric power on weekends (especially on Sunday) could produce variations with a seven day period. A search for such periods is described in the second half of this paper.

#### VLF AMPLITUDE AND PHASE DATA

The paper reports on the analysis of VLF amplitude and phase measurements made in 1967 using the propagation path between the 18.6 kHz NLK transmitter located at Jim Creek, Washington (48.204°N, -121.25°E), and a receiver located at Byrd Station, Antarctica (-79.97°N, -120.0°E). The great circle propagation path is shown in Figure 1. The length of the short path is 14,250 km, and the length of the long path (on the opposite side of the Earth) is 25,770 km. The short path has a nearly constant longitude.

Representative plots of the amplitude data are illustrated in Figure 2. During winter (Figure 2a) and summer (Figure 2c), the dawn-dusk terminator crosses the VLF propagation path at a nonzero angle. This produces a more gradual transition between day and night values than is observed during the periods around Equinox (Figures 2b and 2d).

For the first 50 days of phase measurements, the receiver frequency was  $6 \times 10^{-6}$  Hz offset from the NLK transmitter frequency. This produced a gradual shift in the phase measurements (Figure 3). After the receiver frequency was corrected, the phase contained relatively slow variations

on which the daily changes are superimposed. Before analysis of the data, the slow variations were estimated and subtracted from the phase data. Like the amplitude data, the winter and summer phase data (Figures 4a and 4c) showed more gradual transitions between day and night than did the measurements taken during the periods around Equinox (Figures 4b and 4d).

#### MODEL OF THE EARTH-IONOSPHERE (E-I) WAVEGUIDE

The E-I waveguide consists of a spherical lower boundary (i.e., the earth's surface) and an upper boundary (i.e., the D-region at the bottom of the ionosphere). Since most of the propagation path is over the ocean, the lower surface is taken to have infinite conductivity. The D-region conductivity parameter, as defined by Wait and Spies (1964), is given by

$$\frac{\omega_p^2}{\nu} = (2.5 \times 10^5 \text{ s}^{-1}) \exp[\beta(z - h)] , \quad (1)$$

where  $\omega_p$  is the plasma frequency,  $\nu$  is the effective collision frequency,  $\beta$  is the bottom-side normalized conductivity gradient,  $h$  is the reference height, and  $z$  is the altitude. Typical coefficient values for the day-time D-layer are  $\beta = 0.3 \text{ km}^{-1}$  and  $h = 70 \text{ km}$ . The conductivity,  $\frac{\omega_p^2}{\nu}$ , is directly proportional to electron concentration because of the  $\omega_p^2$  dependence and inversely proportional to neutral concentration because of  $\nu$  dependence.

Wait and Spies (1964) have numerically calculated the relationship between changes in  $\beta$  and  $h$  and changes in the amplitude and phase of

VLF signals propagating in the waveguide. Their results are used in linearized expressions for computing perturbations of the D-region.

Using Taylor series expansion, small changes in amplitude and phase can be written as

$$\Delta s = \Delta h \frac{\partial s}{\partial h} + \Delta \beta \frac{\partial s}{\partial \beta}, \quad (2)$$

$$\Delta p = \Delta h \frac{\partial p}{\partial h} + \Delta \beta \frac{\partial p}{\partial \beta}, \quad (3)$$

where  $s$  is signal strength in dB,  $p$  is signal phase in radians, and  $\Delta$  denotes small changes about mean values  $\bar{s}$ ,  $\bar{p}$ ,  $\bar{h}$ , or  $\bar{\beta}$ . The numerical values for the coefficients in Equations (2) and (3) are given in Table 1.

Table 1  
Waveguide Propagation Parameters

Parameter	Day	Night	Average of day and night
$\bar{\beta}(\text{km}^{-1})$	0.3	0.54	0.42
$\bar{h}(\text{km}^{-1})$	70.0	85.4	77.7
$\bar{s}(\text{dB})$	-36.36	-23.9	-30.13
$\partial s / \partial \beta (\text{dB-km})$	58.1	47.9	53.0
$\partial s / \partial h (\text{dB/km})$	0.27	-0.42	-0.07
$\bar{p}(\text{radians})$	5556.4	5573.0	5564.7
$\partial p / \partial \beta (\text{rad-km})$	16.83	16.91	16.87
$\partial p / \partial h (\text{rad/km})$	0.659	0.660	0.660

The parameters in Table 1 were determined as follows. The daytime values of  $\beta$  and  $h$  were assumed. The nighttime values were computed for the average day-to-night variations in the amplitude and phase data. The values for  $s$ ,  $p$ , and the derivatives were obtained from Wait and Spies (1964) assuming propagation of only the first ( $n = 1$ ) waveguide mode. Waveguide attenuation, phase velocity, and mode excitation were considered in the computations. The amplitude of the second ( $n = 2$ ) waveguide mode is at least 21 dB below the amplitude of the first mode for the 14,250 km propagation path. Crombie (1958) proposes that, for short paths greater than 15,000 km, long-path propagation may become important. In our case, the long (25,770 km) path signal amplitude is calculated to be at least 18 dB below the short path signal amplitude. Consequently, high order waveguide modes and long-path propagation are neglected in this work.

Solving for  $\Delta h$  and  $\Delta \beta$  in Equations (2) and (3) yield matrix equations of the form

$$\begin{bmatrix} \Delta h \\ \Delta \beta \end{bmatrix} = \begin{bmatrix} J_{11} & J_{12} \\ J_{21} & J_{22} \end{bmatrix} \begin{bmatrix} \Delta s \\ \Delta p \end{bmatrix}, \quad (4)$$

The values for the matrix coefficients are given in Table 2.

Table 2  
Coefficients Relating Amplitude and Phase  
Fluctuations to Changes in the D-Region

	Day	Night	Average
$J_{11}$	-0.50	0.423	-0.466
$J_{12}$	1.72	1.198	1.466
$J_{21}$	0.0195	0.0165	0.0182
$J_{22}$	-0.008	0.0105	0.0019

#### LUNAR-INDUCED VARIATIONS

The lunar-induced semi-diurnal ( $L_2$ ) component is identified by spectral analysis of the data. A time series representation of the component is provided by digital filters. The filtering techniques used here are described in detail by Bernhardt (1979).

The  $L_2$  tidal frequency has a theoretical value of 1.932 cycles per day. Fourier transforms of both the phase and amplitude data show a spectral peak at  $1.93 \pm 0.0035$  cycles per day. To test the significance of that frequency line, the phase data were divided into three, nonoverlapping time series of 88 days each. The Fourier transform spectrum of each individual series also showed the  $L_2$  line. Figure 5 illustrates the average of the three 88 day spectrums. The error bar indicates the standard deviation of the  $L_2$  component.

The data are dominated by strong solar harmonics having frequencies that are multiples of 1 cycle per day. These are labeled  $S_1$  and  $S_2$



in Figure 5. These harmonics are suppressed by processing the data with a digital filter. Figure 6 illustrates the spectrum of the VLF amplitude data after the filtering. The lunar ( $L_2$ ) spectral line is weak in comparison with other spectral lines. Further processing is required to isolate the lunar component.

Both the amplitude and phase data are next filtered. Only frequencies between 1.892 and 1.972 remain in the data. The filter used for this processing has a response time of 25 days. The outputs of the filter for day numbers 112 through 118 of 1967 are illustrated in Figure 7. The lunar-induced phase and amplitude are described by the equations:

$$\Delta p_L = \alpha_p \cos \left[ \frac{2\pi(\tau - \delta_p)}{12} \right] \text{ radians ,} \quad (5)$$

$$\Delta s_L = \alpha_s \cos \left[ \frac{2\pi(\tau - \delta_s)}{12} \right] \text{ dB ,} \quad (6)$$

where  $\tau$  is the local lunar hour,  $\tau = 0$  hr is the time of lower lunar transit,  $\tau = 12$  hr is the time of upper lunar transit;  $\Delta p_L$  is the lunar-induced phase variation;  $\Delta s_L$  is the lunar amplitude variation;  $\alpha_p$  and  $\alpha_s$  are the cosinusoidal amplitudes; and  $\delta_p$  and  $\delta_s$  are the time references in lunar hour. The lunar-induced variations have the seasonal variations shown in Figure 8. The maximum values for both  $\Delta p_L$  and  $\Delta s_L$  occur near day 115. The reference times for the phase and amplitude are found to be  $\delta_p = 5.48 \pm 0.65$  lunar hour and  $\delta_s = 8.42 \pm 0.16$  lunar hour.

The amplitude and phase changes are translated into changes in the D-region by using Equation (4). Since the lunar variations are

representative of both the day and night D-region, the day-night average values for  $J_{11}$ ,  $J_{21}$ ,  $J_{12}$ , and  $J_{22}$  are used. This analysis yields the following description of changes in the D-region due to the lunar time near the time of maximum effect:

$$\Delta h_L = 0.39 \cos \left[ \frac{2\pi(\tau - 5.9)}{12} \right] \text{ km} , \quad (7)$$

$$\Delta \beta_L = 0.0048 \cos \left[ \frac{2\pi(\tau - 8.2)}{12} \right] \text{ km}^{-1} . \quad (8)$$

The D-region reference height reaches a maximum value 0.39 km above its average value, at approximately 5.9 and 17.9 lunar hour. The D-region bottom-side scale gradient maximizes near 8.2 and 20.2 lunar hour.

#### HEBDOMADAL VARIATIONS

Spectral analysis of the phase and amplitude data does not produce a clear spectral line with a period of seven days. Thus, hebdomadal effects are not as pronounced as the lunar tidal effects. This may be partially due to the increased level of background noise at the lower frequencies.

The search for a weekly periodicity in the VLF phase and amplitude data proceeded as follows. The data were separated into nighttime (2030-0350 local time) and daytime (0830-1550 local time) blocks. The periods were chosen to exclude the transition periods at dawn and dusk. The data were then superposed and averaged according to the day of the week. Only unbroken strings of data of seven days were used. The

superposition process is equivalent to filtering the data with a harmonic filter which passes frequencies which are multiples of 1// cycle per day (Bernhardt, 1974; Bernhardt and Schlapp, 1976).

The results of the superposition analysis are illustrated in Figure 8 and Figure 9. The phase does not show any significant variation with day of the week. At night, the average phase on Tuesdays and Wednesdays exceeds the average phase for the rest of the days of the week by about 35 degrees. This is not significant when compared to the standard deviation of the measurements which is greater than 70 degrees. Similarly, the 35 degree drop in phase during the Monday and Tuesday daylight hours is not considered to be significant.

Analysis of the amplitude data, however, shows a clear indication of an increase in VLF amplitude on Sundays (Figure 9). At night, the amplitude on Sundays is 0.14 dB greater than the weekly average; during the day, that amplitude is 0.46 dB above the average. These increases are almost two standard deviations above the mean.

The increase in amplitude on Sundays cannot, by itself, be used to determine the changes in the  $h$  and  $\beta$  of the D-region model. Using Equation (2) and Table 1, one obtains the expressions

$$\Delta s_N = 0.42 \Delta h_N + 47.93 \Delta \beta_N = 0.14 \text{ dB} , \text{ Night} \quad (9)$$

$$\Delta s_D = 0.27 \Delta h_D + 58.1 \Delta \beta_D = 0.46 \text{ dB} , \text{ Day} \quad (10)$$

where the subscripts N and D denote hebdomadal variations during the night and the day, respectively.

## DISCUSSION OF RESULTS

The analysis presented in the paper has shown that VLF phase and amplitude measurements show evidence of lunar tidal oscillations. The VLF amplitude data also contain a 7-day periodicity which may be related to hebdomadal variations in electric power consumption. No other variations, such as might be produced by the solar rotation, were identified in this study.

As discussed in the Introduction, the lunar-induced variation in VLF phase has been previously observed by Brady and Crombie (1963). They concluded that the D-region reaches a peak altitude 0.12 km above its average altitude at a lunar hour of 11.33 local lunar time. The study presented here gives a maximum  $\Delta h_E$  of 0.39 km at 5.9 lunar hour. The factor of three discrepancy in  $\Delta h_E$  is probably due to seasonal variations in the lunar effect. Some differences between the two results may also be due to the different paths on which the measurements were made. The paths used by Brady and Crombie covered more than  $26^\circ$  in longitude. The present study used a propagation path which did not vary in longitude by more than  $1.25^\circ$ . Since the magnitude of the lunar tide is strongly dependent on local time, one expects to see the largest effect for a VLF path which stays at a constant longitude.

The time reference for the lunar semi-diurnal component is approximately 5.5 lunar hours different for the two studies. Since the lunar "semi-day" is 12 hours long, the two results are nearly 180 degrees out of phase. The results presented here show that the D-region reaches its

minimum height 0.1 hours before lunar transit. This is consistent with the analysis of Appleton and Beynon (1949) showing peak 2 MHz absorption 1.10 hours before transit, and it is also in agreement with the 0.15 MHz absorption measurements of Mitra (1955) showing peak absorption 2.3 hours before transit.

As expected, the lunar tide produces VLF amplitude changes along with the phase changes. The largest value of amplitude variation is  $\pm 0.26$  dB. The amplitude fluctuation lags the phase fluctuation by about three hours. A  $\pm 0.0048 \text{ km}^{-1}$  variation in the normalized bottom-side gradient ( $\beta$ ) of the D-region is estimated. An increase in  $h$  and  $\beta$  probably results from a decrease in electron concentration and an increase in the neutral concentration at the bottom of the ionosphere. The results of our analysis can be interpreted as a change in the neutral concentration due to the lunar semi-diurnal tide.

The hebdomadal variations in VLF amplitude are consistent with theories that attribute precipitation of energetic electrons from the magnetosphere to power line radiation (PLR). The results of the preceding section show that, on Sundays, the VLF amplitude is, on the average, higher than during the rest of the week. This is most likely due to some anthropogenic activity. One explanation is that less PLR occurs on Sunday because of reduced weekend usage of electric power in the western United States. The lower level of PLR in the magnetosphere scatters less radiation belt electrons into the atmosphere. This would lead to a decrease in the D-region ionization resulting in an increase in the parameters  $h$  and  $\beta$ . According to Equations (9) and (10), this process could account for the Sunday increase in VLF signal strength.

#### ACKNOWLEDGEMENTS

The authors thank F. J. Kelly, C. G. Park, R. A. Helliwell, A. C. Fraser-Smith, and A. V. da Rosa for valuable discussions. Special thanks to A. G. Jean for locating the VLF data. This research was sponsored by the Office of Naval Research Contract N00014-77-C-0586.

## REFERENCES

- Appleton, E. V., and W. J. G. Beynon, "Lunar oscillations in the D layer of the ionosphere," Nature, 164, 308, 1949.
- Bernhardt, P. A., "Separation of lunar and solar periodic effects in data," J. Geophys. Res., 78, 4343, 1974.
- Bernhardt, P. A., "Digital processing of ionospheric electron content data," IEEE ASSP Trans., ASSP-27, 705, 1979.
- Bernhardt, P. A., and C. G. Park, "Protonospheric-ionospheric modeling of VLF ducts," J. Geophys. Res., 82, 5222, 1977.
- Bernhardt, P. A., and D. M. Schlapp, "Suppression of the unwanted variations in data," J. Geophys. Res., 81, 3423, 1976.
- Brady, A. H., and D. D. Crombie, "Studying the lunar tidal variations in the D region of the ionosphere by means of very-low-frequency phase observations," J. Geophys. Res., 68, 5437, 1963.
- Bullough, K., A. R. L. Tatnall, and M. Denby, "Man-made ELF/VLF emissions and the radiation belts," Nature, 260, 401, 1976.
- Chilton, C. J., D. D. Crombie, and A. Glenn Jean, "Phase variations in VLF propagation," Propagation of Radiowaves at Frequencies below 300 KC/S, W. T. Blackburn, ed., pp. 257-290, Pergamon Press, New York, 1964.
- Crombie, D. D., "Differences between EW and NS propagation of VLF signals over long distances," J. Atmosph. Terr. Phys., 12, 110, 1958.
- Fraser-Smith, A. C., "A weekend increase in geomagnetic activity," J. Geophys. Res., 84, 2089, 1979.

- Helliwell, R. A., J. P. Katsufakis, T. F. Bell, and R. Raghuram, "VLF line radiation in the earth's magnetosphere and its association with power system radiation," J. Geophys. Res., 80, 4249, 1975.
- Lurette, J. P., C. G. Park, and R. A. Helliwell, "Longitudinal variations of very-low-frequency chorus activity in the magnetosphere: Evidence of excitation by electrical power transmission lines," Geophys. Res. Lett., 4, 275, 1977.
- Lurette, J. P., C. G. Park, and R. A. Helliwell, "The control of magnetospheric chorus by power line radiation," J. Geophys. Res., 84, 2657, 1979.
- Lurette, J. P., C. G. Park, and R. A. Helliwell, "Comment on 'On possible causes of apparent longitudinal variations inOGO 3 observations of VLF chorus' by C. T. Russell," J. Geophys. Res., 85, 1343, 1980.
- Mitra, A. P., "The lunar semi-diurnal oscillation in the ionospheric absorption of 150-kc/s radio waves," J. Atmosph. Terr. Phys., 7, 99, 1955.
- Muraoka, Y., "Lower ionospheric disturbances observed in long-distance VLF transmission at mid-latitude," J. Atmosph. Terr. Phys., 41, 1031, 1979.
- Park, C. G., "VLF wave activity during a magnetic storm: A case study of power line radiation," J. Geophys. Res., 82, 3251, 1977.
- Park, C. G., and R. A. Helliwell, "Magnetospheric effects of power line radiation," Science, 200, 727, 1978.
- Park, C. G., and T. Miller, "Sunday decreases in magnetospheric VLF wave intensity," J. Geophys. Res., 84, 943, 1979.



Potemra, T. A., and T. J. Rosenberg, "VLF propagation disturbances and electron precipitation at mid-latitudes, J. Geophys. Res., 78, 1572, 1973.

Wait, J. R., and K. P. Spies, "Characteristics of the earth-ionosphere waveguide for VLF radio waves," National Bureau of Standards Tech. Note 300, 1964.

## FIGURE CAPTIONS

Figure 1. VLF propagation path between NLK, at Jim Creek, Washington, and Byrd Station, Antarctica.

Figure 2. Diurnal variations in the relative amplitude of the VLF signals received at Byrd. The day of the year is plotted in universal time. Note how that the day-night transitions are steeper during the period near Equinox.

Figure 3. Phase measurements made at Byrd. Slow trends in the data are due to frequency differences between transmitter and receiver.

Figure 4. Diurnal variations in the relative phase. Note the rapid changes at dawn and dusk during the period near Equinox.

Figure 5. Power spectrum of the phase measurements. The solar diurnal harmonics ( $S_1$  and  $S_2$ ) dominate the spectrum. The magnitude of the lunar ( $L_2$ ) line is  $1/80$  of the  $S_1$  magnitude.

Figure 6. Power spectrum of the VLF amplitude measurements with suppressed solar harmonics.

Figure 7. Output of a digital filter with passband at  $1.932 \pm 0.04$  cycles per day. The lower and upper transit of the moon are designated by L and U, respectively.

Figure 8. Seasonal variations in the amplitude of the lunar-induced fluctuations in VLF phase and signal strength. Both observations have maximum values near day 115 of 1967.

Figure 9. VLF phase superposed and averaged by the day of the week. The variations are a fraction of one standard deviation of the measurements and consequently are not significant.

Figure 10. VLF amplitude superposed and averaged by day of the week.

A significant increase in signal strength occurs on Sunday during both night and day.

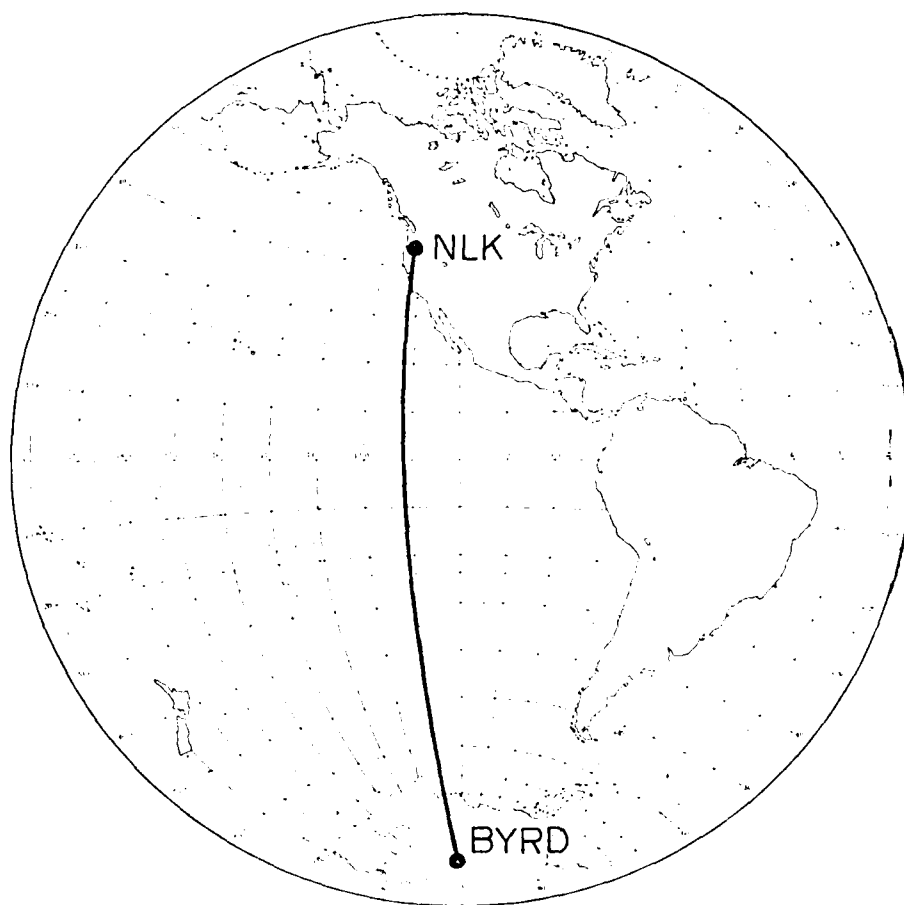
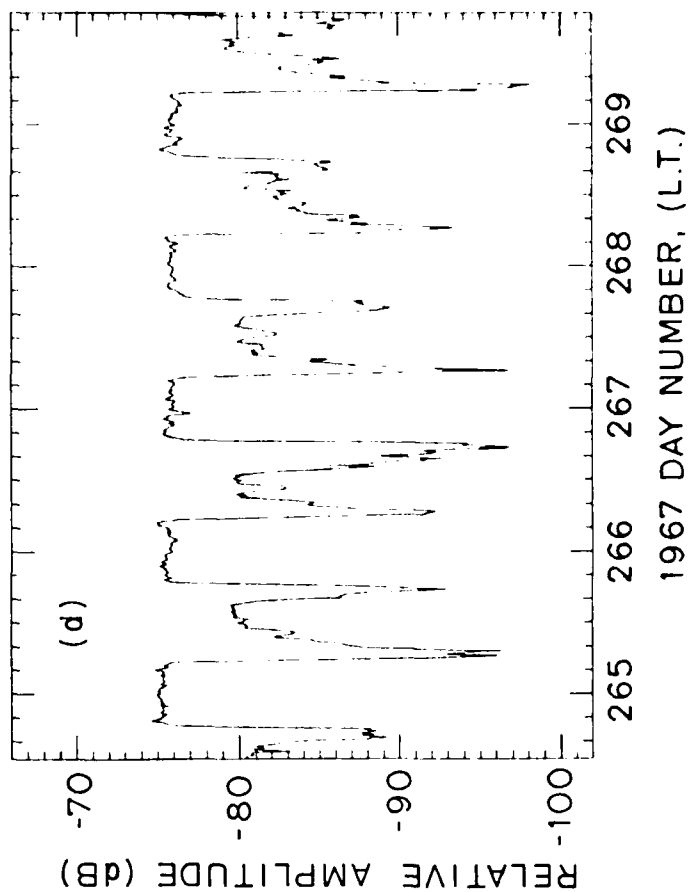
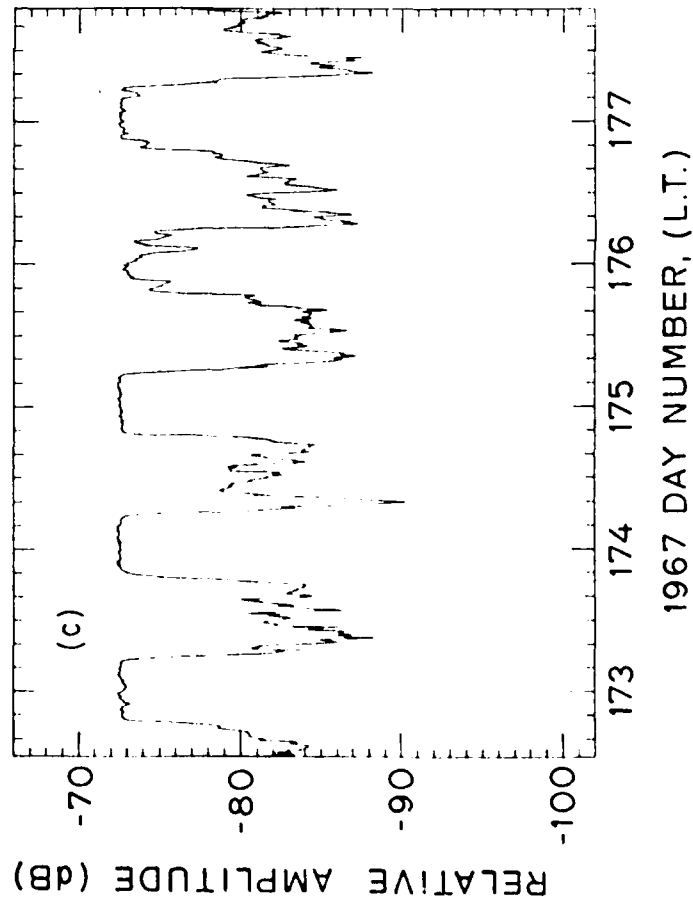
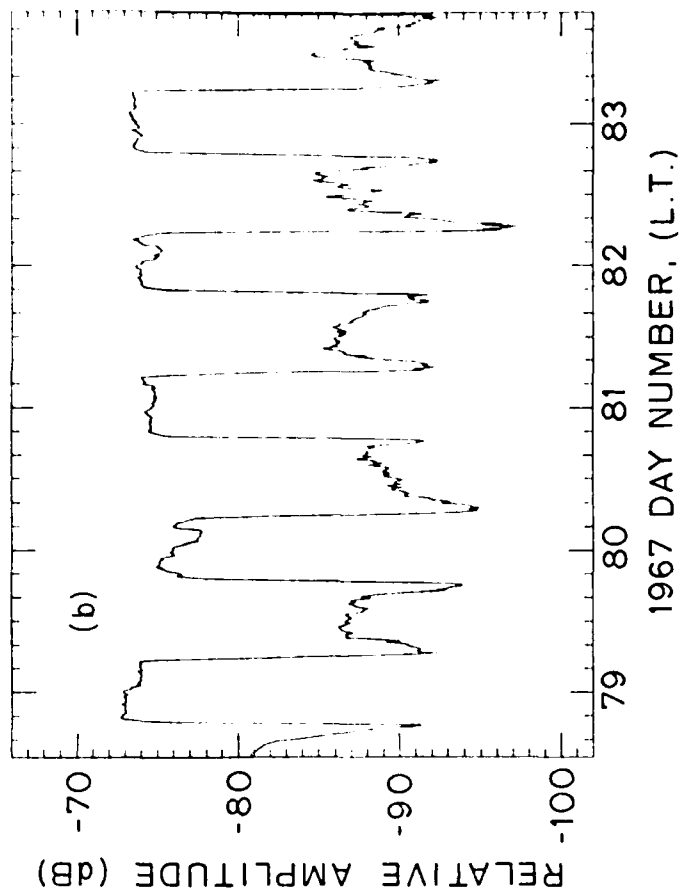
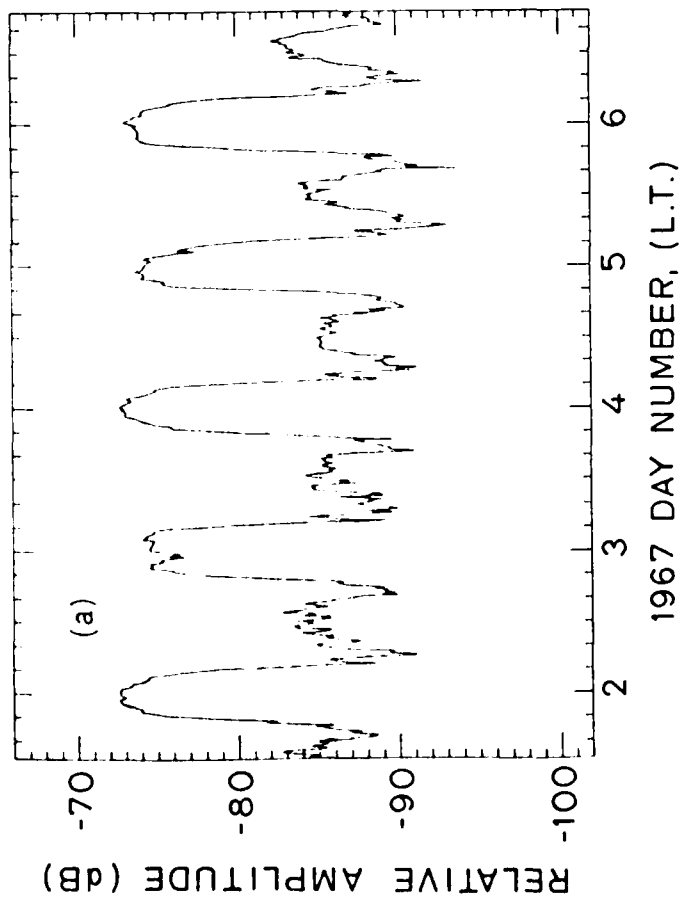


Figure 1. VLF propagation path between NLK, at Jim Creek, Washington, and Byrd Station, Antarctica.



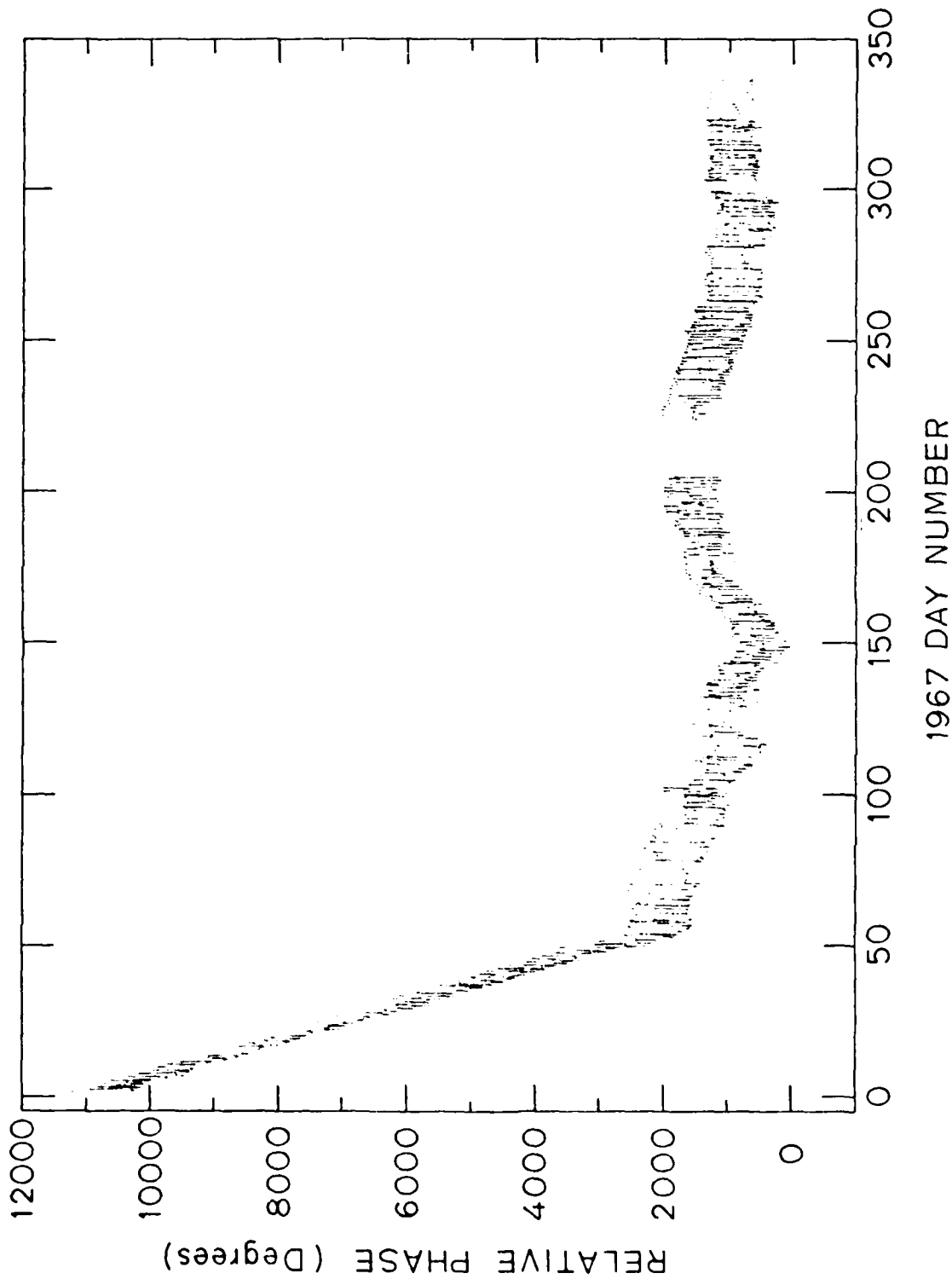


Figure 3. Phase measurements made at Byrd. Slow trends in the data are due to frequency differences between transmitter and receiver.

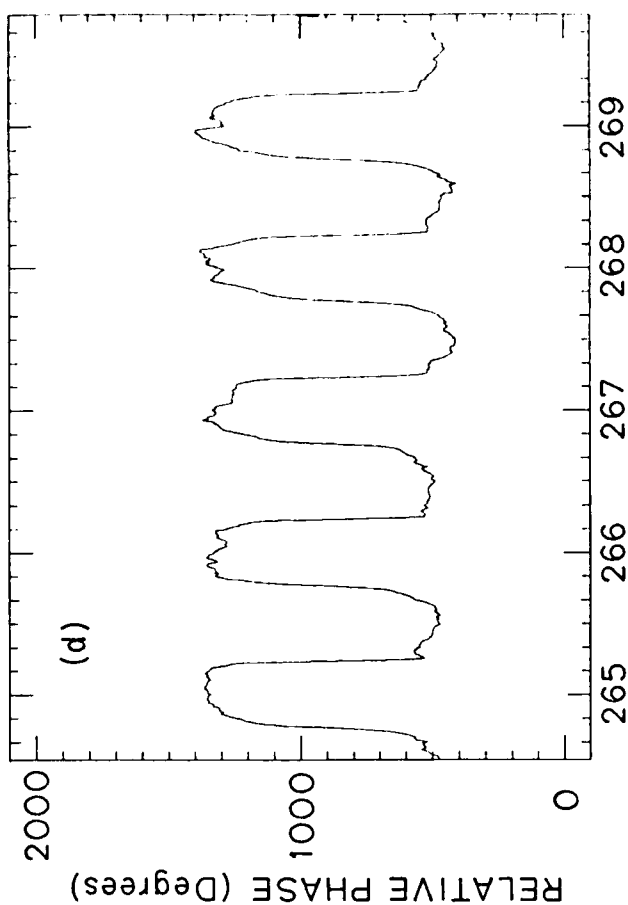
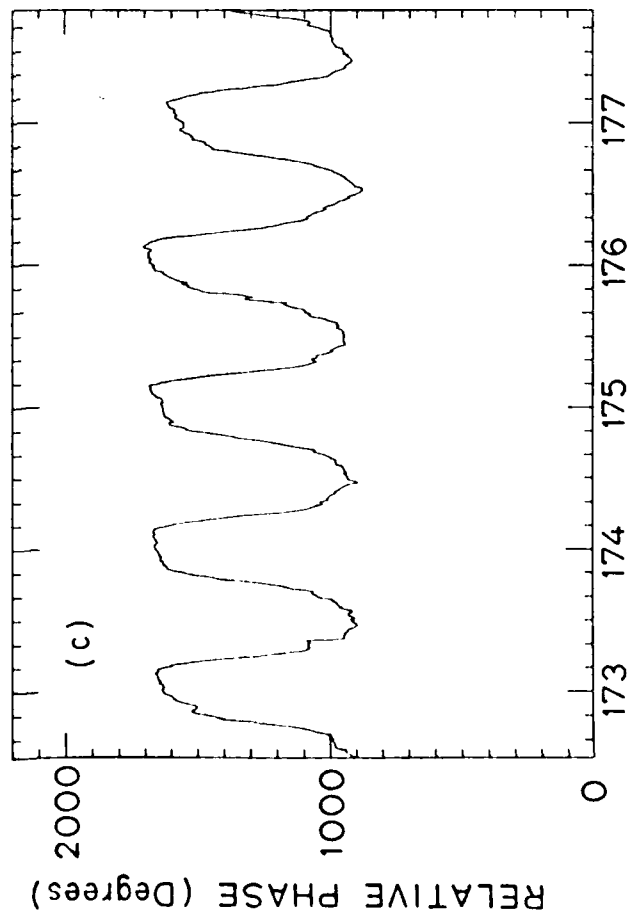
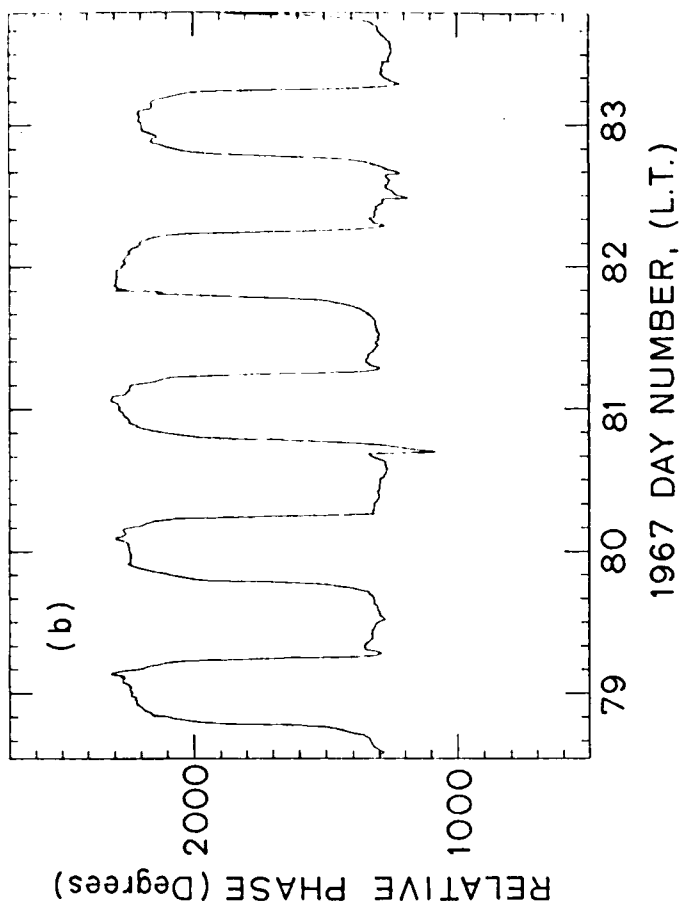
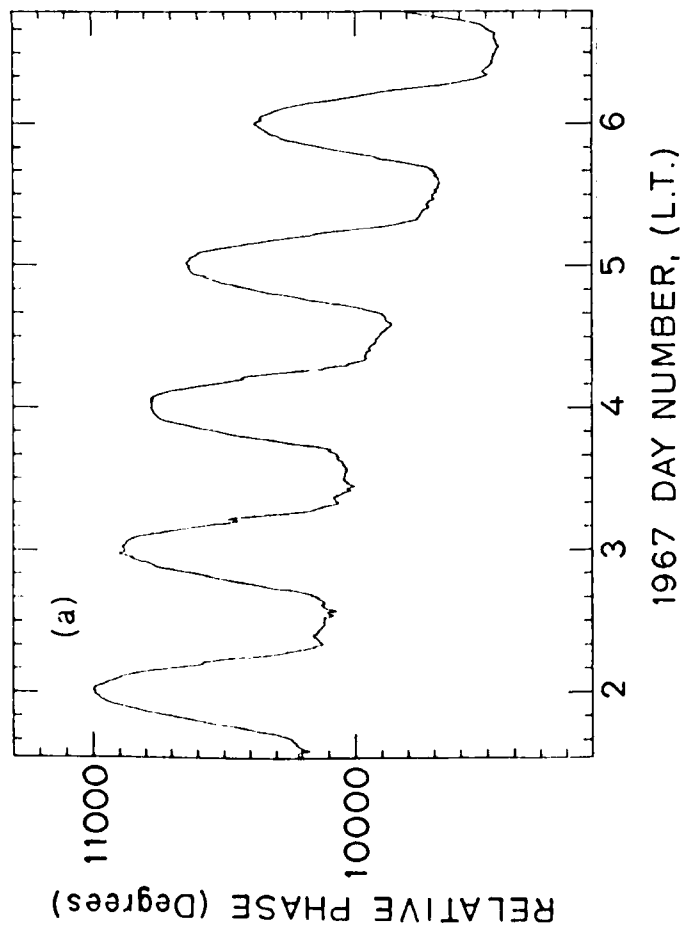


Figure 4. Diurnal variations in the relative phase. Note the rapid changes at dawn and dusk during the period near Equinox.

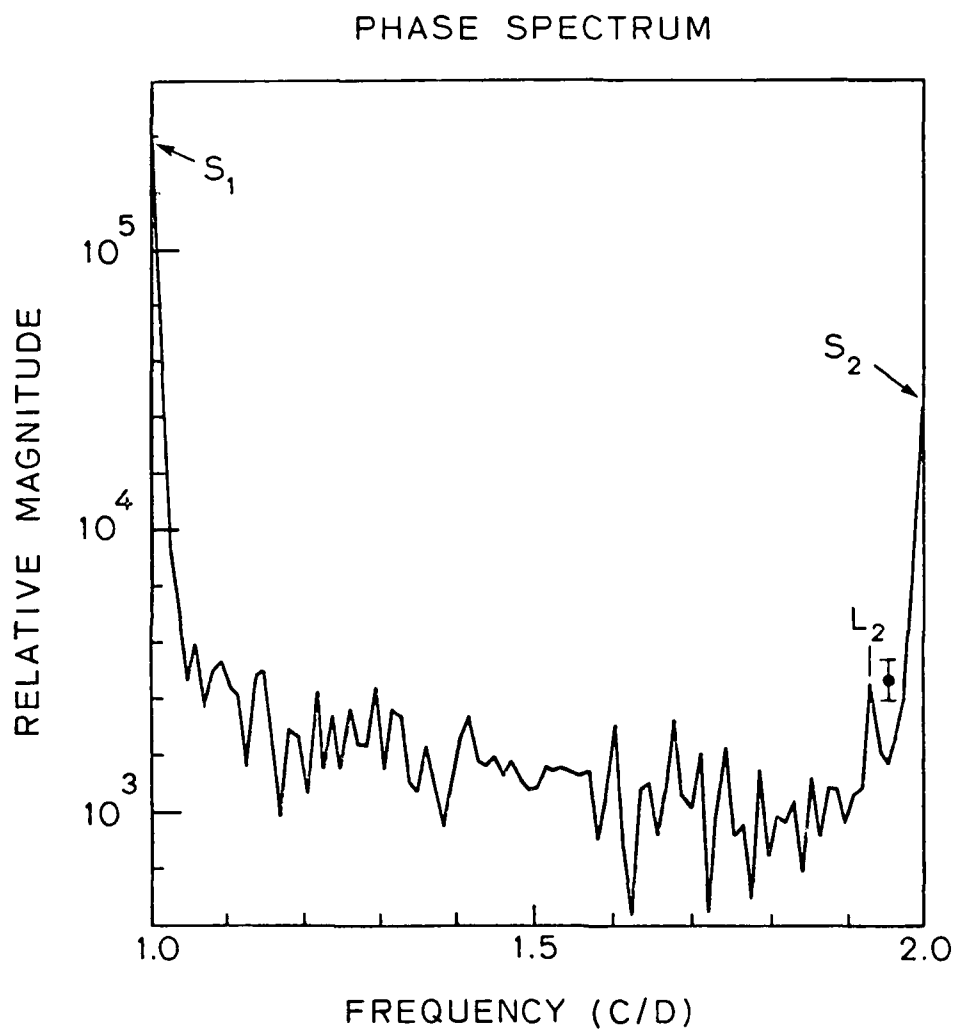


Figure 5. Power spectrum of the phase measurements. The solar diurnal harmonics ( $S_1$  and  $S_2$ ) dominate the spectrum. The magnitude of the lunar ( $L_2$ ) line is 1/80 of the  $S_1$  magnitude.



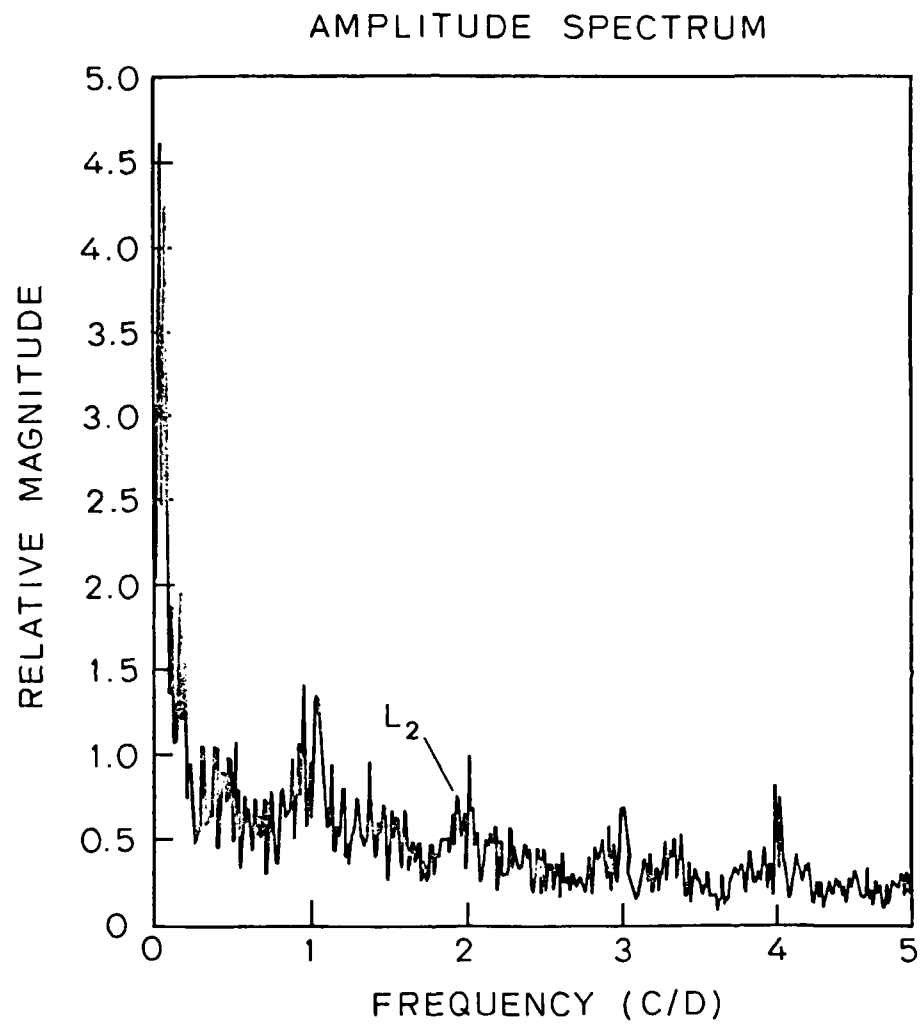


Figure 6. Power spectrum of the VLF amplitude measurements with suppressed solar harmonics.

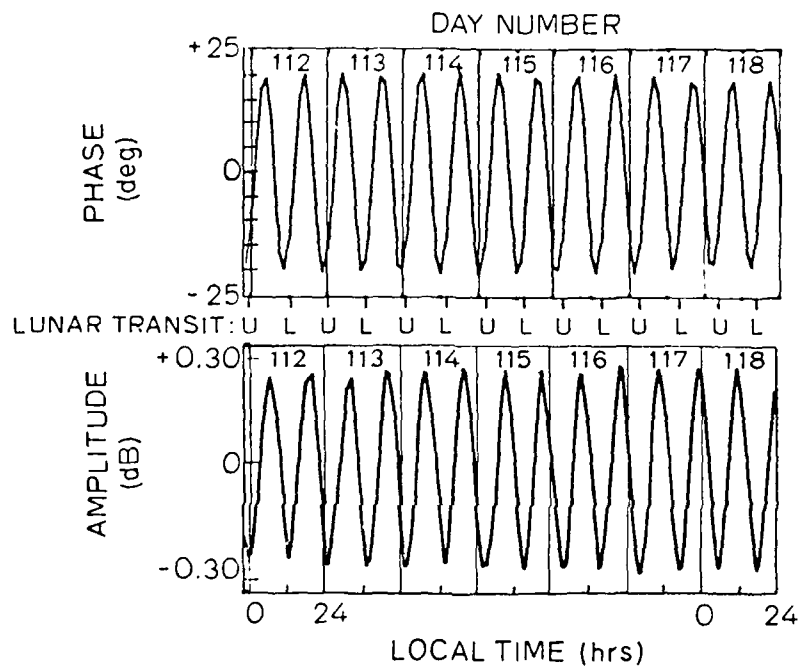


Figure 7. Output of a digital filter with passband at  $1.932 \pm 0.04$  cycles per day. The lower and upper transit of the moon are designated by L and U, respectively.

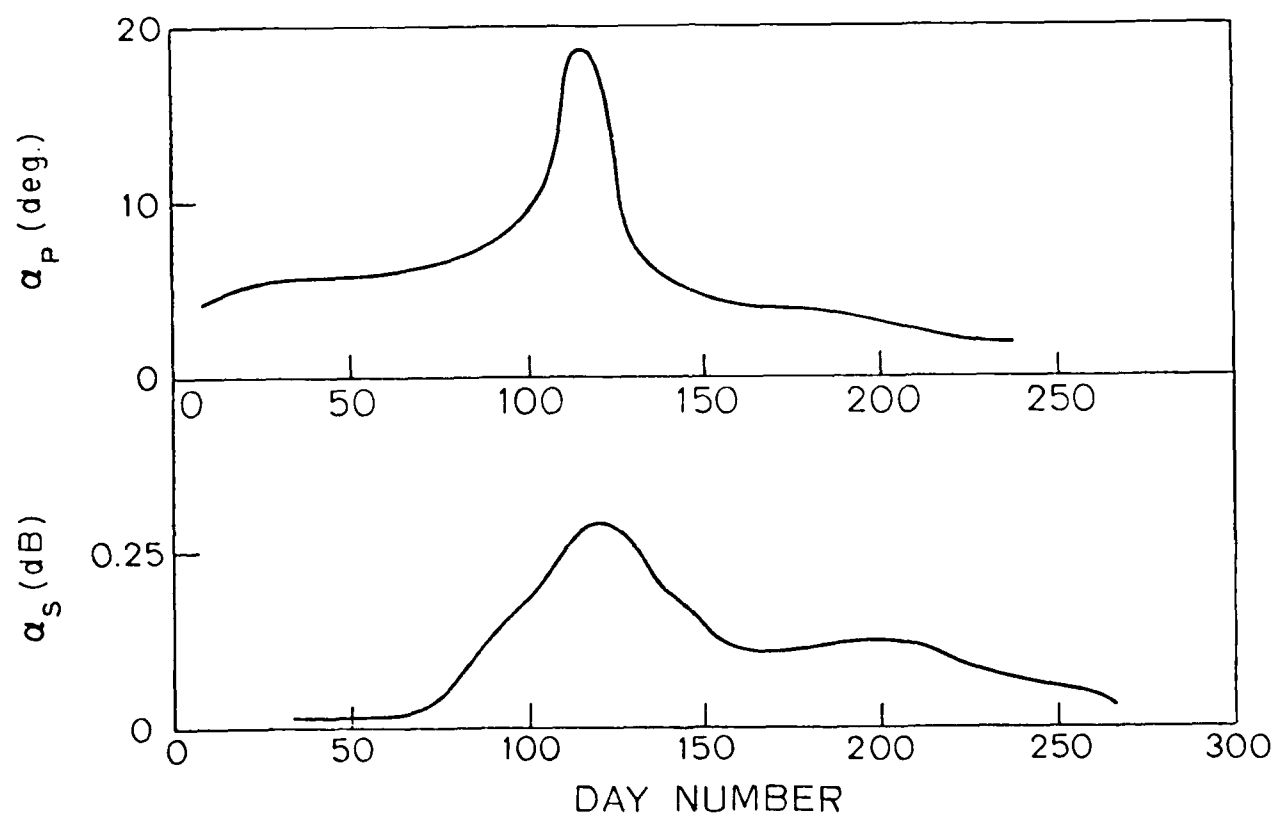


Figure 8. Seasonal variations in the amplitude of the lunar-induced fluctuations in VLF phase and signal strength. Both observations have maximum values near day 115 of 1967.

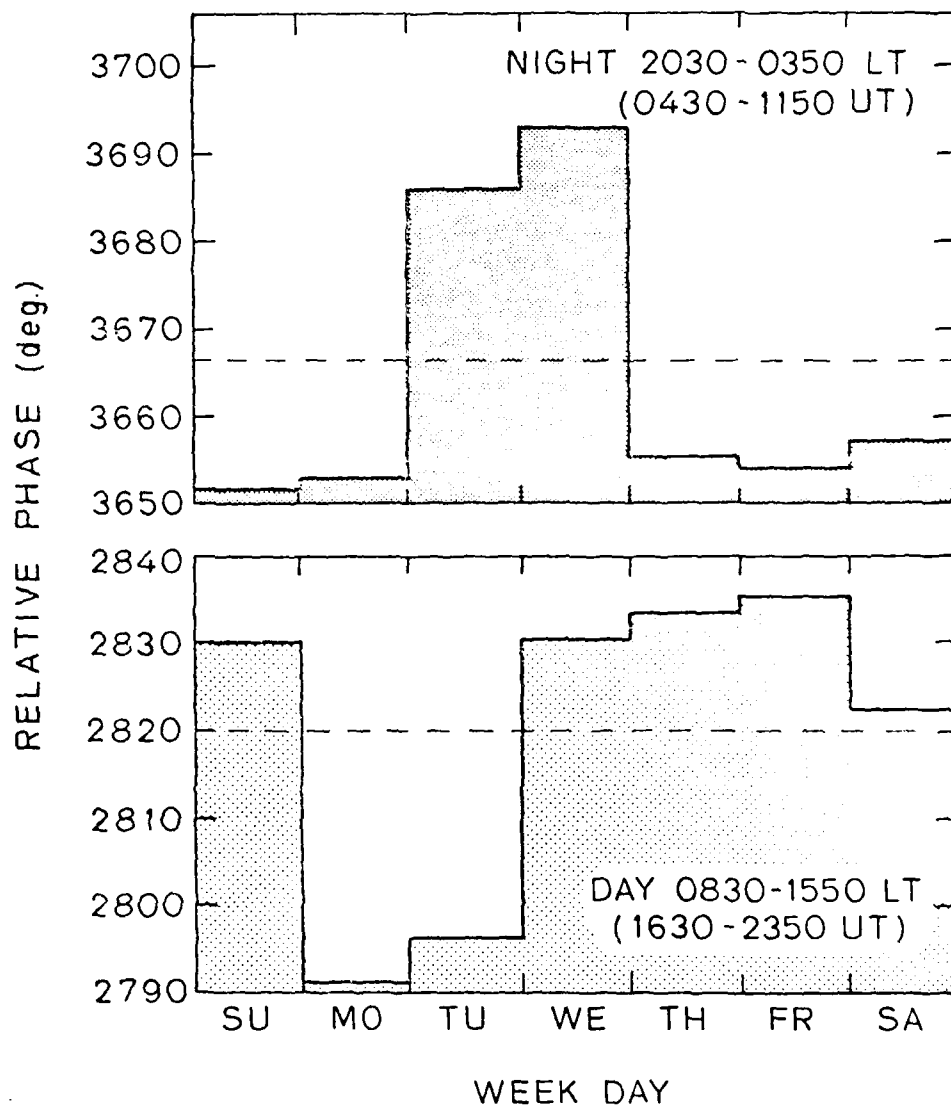


Figure 9. VLF phase superposed and averaged by the day of the week. The variations are a fraction of one standard deviation of the measurements and consequently are not significant.

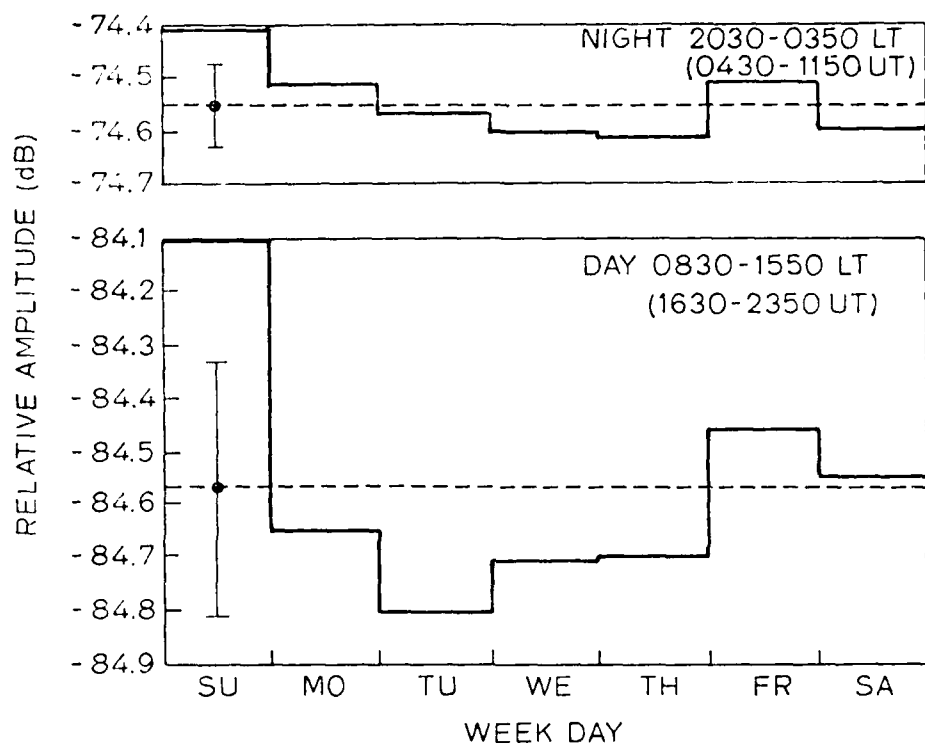


Figure 10. VLF amplitude superposed and averaged by day of the week. A significant increase in signal strength occurs on Sunday during both night and day.

#### PUBLICATION LIST

- Bernhardt, P. A., "Three-dimensional, time-dependent modeling of neutral gas diffusion in a nonuniform, chemically reactive atmosphere," J. Geophys. Res., 84, 793, 1979a.
- Bernhardt, P. A., "High altitude gas releases: Transition from collisionless flow to diffusive flow in a nonuniform atmosphere," J. Geophys. Res., 84, 4341, 1979b.
- Bernhardt, P. A., "Changes in the electromagnetic properties of the upper atmosphere due to rocket effluents," submitted to J. Spacecraft and Rockets, 1980.
- Bernhardt, P. A., K. M. Price and J. H. Cray, "Periodic fluctuations in the earth-ionosphere waveguide," submitted to J. Geophys. Res., 1980.

END

DATE  
FILMED

03-82

DTIC